ULTRA LOW ENERGY GOLD CLUSTER ION BEAMS FOR SIMS APPLICATIONS

JUI-HSIEN CHANG MSc

Thesis for the degree of Doctor of Philosophy

submitted to

The University of Warwick

Department of Physics

August 2008

Table of Contents

List of Figures

List of Tables

Acknowledgements

I would like to thank my supervisor, Prof. Mark G. Dowsett, who kindly provided me the opportunity to participate in this interesting project. I am also grateful for his patience in transferring to me the skills of research and instrumentation. Furthermore, the thesis will not have been achieved to this level without his direction.

I would also like to thank Dr Sergey F. Belykh, who taught me scientific knowledge that is more than is covered in the thesis. His friendly companion and suggestions in aspects other than research gave me many joys.

Dr. Richard J H Morris, with his abundant experience in instrumentation, helped me solve many problems, which I am very grateful. He also introduced me to other groups and the Departmental workshops, so that the co-operation with them could be done in a smooth way. Mr. Roger Gibbons is thanked for providing me many useful suggestions.

I would like to thank Mr. Derrick Richards who manufactured the mechanical components, and Mr. Adrian Lovejoy who built the power supplies that we designed, and advised on the related problems.

I owe very much to my family members who supported and encouraged me continually. I would also like to thank friends on campus, in London and Oxford for their companion and encouragement.

Finally, I would like to acknowledge EPSRC for funding myself and this project.

Declaration

The thesis is submitted to the University of Warwick in support of my application for the degree of Doctor of Philosophy. It contains an account of my work in the Department of Physics at the University of Warwick during the period November 2004 to August 2008, under the supervision of Prof. Mark G. Dowsett.

No part of this thesis has been used previously in a degree thesis submitted to this or any other university. The work described is the result of my own research expect where specifically acknowledged in the text.

Jui-Hsien Chang

August 2008

List of Publications

Journal Papers

New Cs sputter ion source with polyatomic ion beams for secondary ion mass spectrometry applications. S. F. Belykh, V. V. Palitsin, I. V. Veryovkin, A. P. Kovarsky, R. J. H. Chang, A. Adriaen, M. G. Dowsett, F. Adams, *The Review of Scientific Instruments* **78** (2007) 085101.

Caesium sputter ion source compatible with commercial SIMS instruments. S. F. Belykh, V. V. Palitsin, I. V. Veryovkin, A. P. Kovarsky, R. J. H. Chang, A. Adriaen, M. Dowsett, F. Adams, *Applied Surface Science* **252** (2006) 7321.

Conference Presentations

Testing of Ultra-Low Energy Gold Cluster Ion Beams for SIMS Applications, R. J. H. Chang, S.F. Belykh, M.G. Dowsett, *44th IUVSTA Workshop: Sputtering and Ion Emission by Cluster Ion Beams*, Scotland UK, 2007.

A cluster ion source for SIMS applications in nanometre-scale surface and interface analysis, Robert J. H. Chang and Sergey F. Belykh, *UK-Taiwan nanoscience workshop*, Royal Society London UK, 2006.

Caesium sputter ion source compatible with commercial SIMS instruments. S. F. Belykh, V. V. Palitsin, I. V. Veryovkin, A. P. Kovarsky, R. J. H. Chang, A. Adriaen, M. Dowsett, F. Adams, *The 15th International Conference on Secondary Ion Mass Spectrometry*, Manchester UK, 2005.

ABSTRACT

The purpose of work was to obtain gold and possible other negative ion cluster beams where each constituent atom in the cluster carried an energy ≤ 1 keV, using the floating low energy ion gun (FLIG^{TM}), and to test these in secondary ion mass spectrometry. The heavy negative metal cluster is worth researching because (i) there is the possibility of generating high secondary ion/sputter yields, and (ii) negative ions would be useful for insulators.

The sputter cluster ion source (SCIS) developed in the University of Antwerp (Belgium) was selected because it can emit cluster ions of pure materials as well as compounds. Gold was chosen due to its high mass and thus high sputter rate. The source was retrofitted to a FLIG column by designing matched ion optics based on simulation, a new mass separator, vacuum devices and power supplies. The ion gun of SCIS-FLIG was then tested and characterised, and defects were improved. As the result, ultra low energy gold cluster ions were obtained for the first time. The ratio of $I_{Au_1^-} : I_{Au_2^-} : I_{Au_3^-}$ is about 13:1.2:1, and a maximum 1 keV Au_1^- current density of 38 μA cm^{-2} was obtained at the sample, which is superior to any reported negative gold cluster ions source. Ions with higher energy (up to 3.7 keV) and positive ions were also obtained. A preliminary study of the usefulness of the gold cluster ions in SIMS depth profiling with a silicon sample was conducted afterwards. Nonlinear sputtering with $E_0 \leq 1$ keV was observed for the first time. The sputter rates of the ions are higher than that of O_2^+ and Cs^+. Gold deposition due to Au_3^- bombardment ($E_0 = 0.33$ keV) was observed at a dose $\leq 0.54\times10^{17}$ cm^{-2}, otherwise sputtering can be achieved with dose $\geq 1\times10^{17}$ cm^{-2}. A peculiar observation is the time dependent evolution of the bombarded silicon surface during subsequent atmospheric exposure. Further work in obtaining a more reliable and long-lived source and a higher current density at the sample is recommended.

Chapter 1 Introduction

1.1 Rationale

Thanks to its high sensitivity and high depth resolution, secondary ion mass spectrometry (SIMS) depth profiling has been widely used in the microelectronics industry for last thirty years for characterisation of ion implants and diffusion processes. From ~1998 onwards, routine SIMS depth profiling has evolved to the use of ultra low energy (≤ 1 keV) ion beams to obtain better depth resolution and the capability for near-surface feature analysis. This technology is commonly termed ultra low energy SIMS, or uleSIMS.

The depth resolution achievable by uleSIMS, however, is not good enough for future roadmap specification, such as in the applications of ultra shallow (< 10 nm) profiles contained in complex structures (Vandervorst W, 2008), and solutions are needed to satisfy this demand. Further reduction of the ion beam energy would increase the influence of space charge effects and chromatic aberration on the beam performance, and increase the magnification on ion columns which use a retarding objective lens, such as the FLIG. Energy-reduced beams are also much more subject to the perturbation by the secondary ion extraction field. As a result, the current density at the sample would be heavily reduced. Furthermore, the sputter rate and ion yield decrease with ion energy. Overall, the analysis would be very time consuming and sensitivity reduced. In addition, with the most commonly used primary ion species, O_2^+ and Cs^+, at the ultra low energy regime, some combinations of ion energy and incidence angle for a specific task can cause surface roughening and other profile-distorting effects.

The combination of cluster ions with the FLIG would allow the column to work at higher energies (> 1 keV) with lower magnification, and each cluster constituent atom would still carry ultra low energy (≤ 500 eV). Moreover, cluster ions have been very well known to enhance sputter and ion yields (up till now, for beam energies 3 keV). The sputter cluster ion source (SCIS) described

here also provides the advantages that any solid element can be used, and the generated negative ions are useful for minimising charging effects.

1.2 Thesis overview

The aim of the major part of the project was to ion-optically, electrically and mechanically match the sputter gold cluster ion source to the floating low energy ion gun, FLIG (Dowsett M G *et al.* 1997), so as to obtain a fine probe with reasonable current density at the sample. Another objective was to investigate the sputtering and surface alteration due to the gold cluster impact, in order to gain an understanding of the usefulness of gold cluster ions in terms of depth profiling.

Chapter 1 of the thesis describes the rationale of the project and the thesis overview. Chapter 2 discusses the fundamentals and instrumentation of secondary ion mass spectrometry, as well as the effects due to cluster ion bombardment and the cluster ion sources that have been recently developed.

The secondary ion mass spectrometer employed in this work – EVA 2000 and the floating low energy ion gun are briefly described in Chapter 3. The set-up and operation principles of the gold cluster ion source are also discussed in this chapter together with the history of its development and previous studies.

Chapter 4 reports the process of matching and retrofitting the source on to the floating ion column. This includes the simulation of the ion trajectories taking into consideration the mutual repulsion between ions (space charge effects). The designed optics, ion species separator (mass separator) and electrical scheme are demonstrated.

The initial test of the source on EVA 2000 is presented in Chapter 5, including the defects that were discovered and the corresponding improvements, such as the development of a new lens after the investigation of the effective emission area of the SCIS gold target (a hollow cone). The characterisation of the source on the floating column, including the current, spot size, beam profile, etc. obtained, are also described in this chapter.

Chapter 6 illustrates the bombardment effects on a silicon sample by monomer, dimer and trimer gold ions. The enhanced sputtering by clusters at ultra-low energy ($\leq$ 1 keV), gold deposition, bombarded surface change in time and surface roughness are discussed.

The project is summarised in Chapter 7, and suggestions for further instrumental development are made in order to obtain higher current density and smaller probe at the sample.

Chapter 2 Secondary Ion Mass Spectrometry and Cluster Ion Effects

2.1 Secondary ion mass spectrometry

2.1.1 Overview

Since the first secondary ion mass spectrometer (SIMS) was constructed in 1949 (Herzog R F K and Vieböck F, 1949), this technique has become one of the major tools for surface characterisation and sample composition studies. Basically, an energetic primary ion beam (0.1-50 keV) impinges on the sample surface, resulting in the sputtering of material from the top few monolayers (predominantly the first). Those secondary particles which are ionised upon leaving the surface, are collected and mass analysed. Information on the sample composition and the concentration of each detected element can thus be obtained.

SIMS may be divided into two modes. Static SIMS (Benninghoven A, 1970) requires that the adjacent damage induced by each primary ion does not overlap, and thus constrains the acceptable primary ion dose to $<< 10^{13}$ ions cm^{-2}. Since most of the emitted (secondary) ions are ejected from the sample surface, static SIMS is used for surface chemistry studies. The other mode, dynamic SIMS (Wittmaack K, 1980), is applied to depth profiling, imaging, image depth profiling and micro-volume analysis, with depth profiling as the largest application. The sample to be analysed by dynamic SIMS is required to be eroded from layer to layer, and consequently the primary ion dose density is usually more than 10^{17} ions cm^{-2} to achieve the steady-state conditions for the erosion rate and the surface chemistry throughout the analysis.

This chapter is devoted to describing the fundamental processes that happen during SIMS analysis and are critical for acquiring correct information, as well as SIMS instrumentation, with a focus on dynamic SIMS.

2.1.2 Primary ion-solid interaction

2.1.2.1 Sputtering

Sputtering was first discovered some 150 years ago in the studies on glow discharge plasmas by Grove (1853) and Faraday (1854) (Grove W R, 1853; Gassiot J P, 1858). After almost half a century, Goldstein performed the first ion-beam induced sputtering experiment (Goldstein E, 1902). Later whilst attempting to experimentally reveal the structure of atom, J J Thompson discovered both neutral particles and positive ions were emitted from a metal surface under the impingement of a positive ion ray (Thompson J J, 1910). It was found that these particles were ejected in all directions and that the fraction of charged particles amongst the total flux was small.

Many attempts had been made to explain the sputtering effects, but failed to describe many of the observed features quantitatively. The most successful explanation to date is the collision cascade model developed by Sigmund (Sigmund P, 1969; 1977; 1981). This model describes how, when an energetic ion strikes a solid sample surface, it undergoes a series of classical elastic binary collisions (nuclear collision). Some struck sample atoms recoil and hit other sample atoms, and thus trigger a knock-on series of collisions. This phenomenon has been termed (*linear*) *collision cascade*. If the energy transferred to a sample atom exceeds a certain value, the atom may be displaced from its lattice site permanently and leave a vacancy behind. Sputtering happens when a recoiling atom, in the intersection of the cascade and the sample surface, has energy higher than the surface binding energy and with an outward directed momentum (Fig. 2.1.1). As most of the sputtered particles originate from the uppermost surface layer, this type of emission which is employed by SIMS makes SIMS a very surface sensitive technique (parts per million to parts per billion). The impacted surface after bombardment is usually amorphous, consisting of displaced sample atoms and incorporated primary ions.

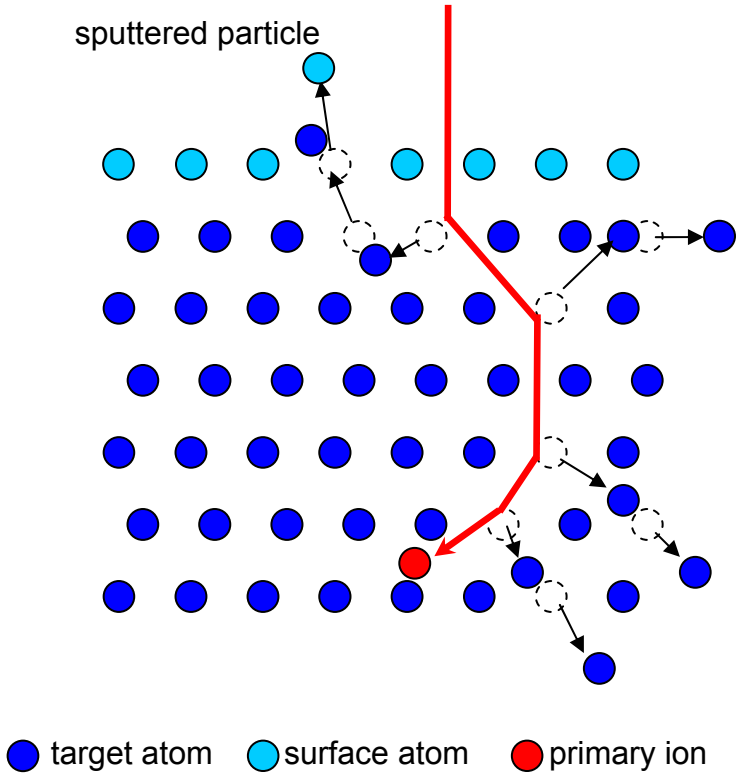

Fig. 2.1.1 Collision cascade and the occurrence of sputtering. The bombardment of primary ions cause sample lattice atom displacements, sputtering and primary ion deposition.

Indeed, with most projectile-target combinations, the developed cascades are *linear*, which means strictly they do not overlap and energy does not share between cascades. In each *linear collision cascade*, only a small fraction of atoms is in motion, and it is assumed that collisions only happen between a moving atom and another initially at rest. Under this situation, *sputter yield*, defined as the mean number of emitted particles per incident primary particle, is constant with the dose of primary particle. The intensity of the sputtered particles against the angle with respect to the surface normal, the *angular distribution*, is normally a cosine distribution (Fig. 2.1.2). Other characteristics of sputtering, such as the energy distribution of the sputtered particles and the dependence of sputter rate on atomic number and incident ion energy, can also be explained by Sigmund's theory.

Nevertheless, when heavy atomic ions with large kinetic energies (Thompson D A, 1981) and cluster ions (Andersen H H *et al.*, 1974-1975) are

used as the primary projectile, deviations from the linear cascade model have been observed. Noticeably, the sputter yield is nonlinear, i.e. the total number of sputtered particles due to a cluster ion impact is more than the sum of that due to the individual cluster constituents (referred to Eqn. 2.2.1). Moreover, in some cases the energy spectra of the emitted secondary particles are peaked at ~ 0.1 eV, in contrast to several eV in the linear cascade case. Efforts, such as the thermal evaporation model (Sigmund P *et al.*, 1981; Sigmund P, 1974) and gas-flow model (Samartsev A V *et al.*, 2005; Urbassek H M *et al.*, 1987), have been made to understand the underlying physics, but still cannot fully explain the nonlinear effects. It has been, however, commonly accepted that the observed phenomena are due to the addition of a nonlinear collision cascade, or a *spike*, which is formed at later stage of a cascade evolution. In a spike, cascades overlap with each other and energy density is increased. Essentially all atoms in the cascade volume are in motion, and collisions happen between two moving atoms. The bombarded surface is more disrupted and surface binding energy reduced. As a consequence, the sputter yield is more than that predicted from a linear cascade.

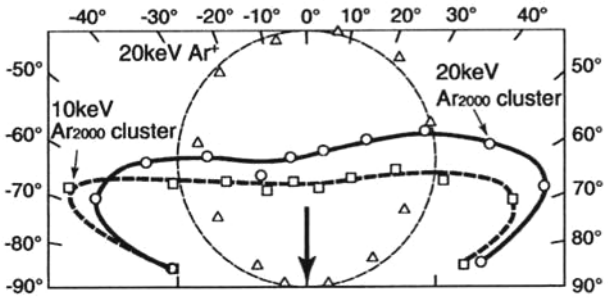

Fig. 2.1.2 The cosine angular distribution of Cu atoms sputtered by 20 keV monomer Ar^+ ions at normal incidence corresponds to Sigmund's theory, in contrast to that by 10 keV and 20 keV Ar_{2000} cluster ions. (reproduced from Yamada I *et al.*, 2001)

2.1.2.2 Secondary ion emission

Amongst the sputtered particles, a few are ionised themselves upon leaving the sample surface. It is these ionised particles that are collected and

analysed in SIMS to acquire information on the sample. The useful ion yield, Y_i, is defined as the number of detected secondary ions per primary particle, which is typically in the range 10^{-1} to 10^{-4} (Dowsett *et al.*, 1992). They are strongly dependent on the surface chemistry, and vary by a factor of 10^4 or more with the sample matrix and the primary ion species.

It was discovered that the adsorption of certain gases on the sample surface can increase positive ion yields (Rybalko V F *et al.*, 1959), and that the bombardment of Cs^+ ions enhances negative ones (Krohn V, 1962). Therefore, these reactive species have been used for SIMS primaries for obtaining higher sensitivity; caesium or other electropositive species are used to enhance negative ion yields, and oxygen or other electronegative species for positive ion yields (Williams P, 1979). Another technique, *flooding of oxygen*, has also been used to increase ion yields by introducing oxygen to the sputtered region of the sample surface (Wittmaack K, 1980). Advantages of this technique, such as rapid equilibration, and disadvantages, such as deteriorated depth resolution, have been studied in detail (Zalm P C *et al.*, 1992). In general, with the use of a normal incidence ion beam, flooding is not used. This technique is also popularly used in applications of high resolution imaging, where a gallium ion beam is normally employed as the SIMS primary (Bishop H E *et al.*, 1989).

The energy spectra of secondary atomic ions usually have a peak between 5 eV to 20 eV with a higher energy tail extending to over 100 eV. The spectra of molecular ions are narrower with a faster decay at high energies. Generally the more atoms that are comprised in the secondary ion, the narrower is the energy spectrum. This effect is useful when the sample surface potential changes due to the primary ion bombardment. The energy bandwidth of the mass spectrometer can be tuned to higher energy to prevent mass interference from molecular ions (Wittmaack K, 1976). The angular distribution of secondary ions is similar to that of sputtered neutrals, represented by a cosine distribution.

In general, sputter yield and ion yield change with primary ion incidence angle with respect to the sample surface normal. Sputter yield usually increases with the incidence angle, but ion yield goes in an opposite trend (Fig. 2.1.3).

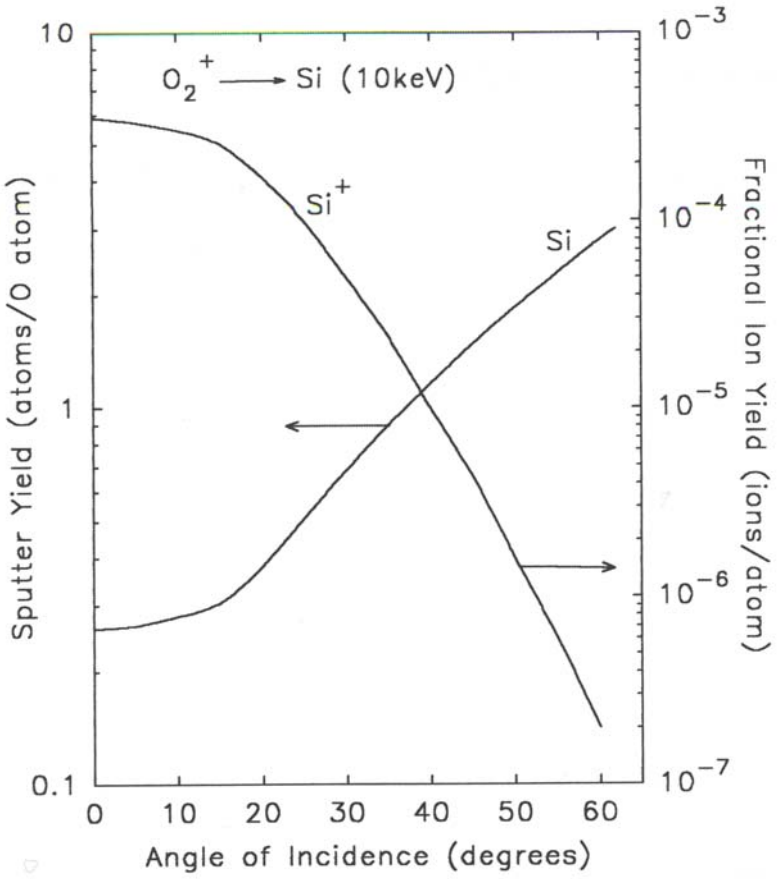

Fig. 2.1.3 Sputter yield and useful ion yield as a function of the primary beam incidence angle (reproduced from Smith N S, 1996).

2.1.2.3 The altered layer and depth profiling

As described previously, the impact of primary ions causes displacement and sputtering of target particles, and projectile atoms stay near the surface mixed in by the cascade. This surface mixing, together with other effects such as preferential sputtering, radiation-enhanced diffusions and segregations (Wittmaack K, 1992), forms a layer in which composition and structure are changed. This region is commonly understood as the *altered layer* (Littmark U *et al.*, 1980; Reuter W *et al.*, 1980). If there happens to be a narrow feature within this layer, the feature atoms may transport with momentum to any direction, and the feature will dilute through out the volume of the layer. The deeper part of the feature will be more diluted, as the surface is ever receding and more matrix atoms are mixed in. The feature when shown on the measured

profile is thus broadened and shifted with respect to the true profile, as can be seen from Fig. 2.1.4. However observed broadened feature is not necessarily due to SIMS primary ion bombardment. In a later study from Dowsett's group, it was found that the broadening effect at the near surface side of a boron delta profile is due to boron segregation occurring in the growth process, rather than being induced by primary ion bombardment (Chu D P *et al.*, 1997).

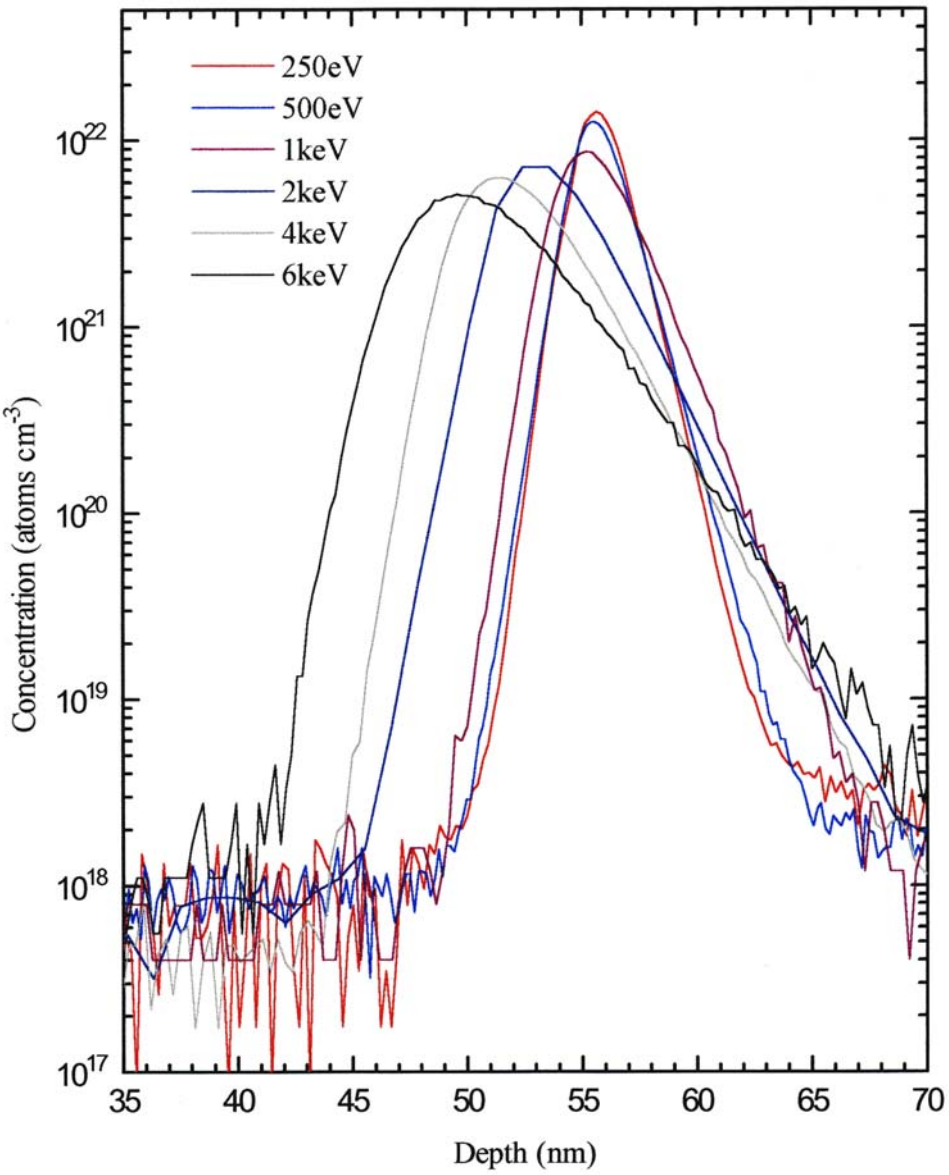

Fig. 2.1.4 Depth profile of a 1 nm think ^{30}Si layer in ^{28}Si. True position of the layer is at 55.8 nm (reproduced from Smith N S, 1996).

In general, better resolution is obtained with a thinner altered layer (Barlow R D *et al.*, 1992), and the layer thickness increases with the primary ion impact energy (Littmark U *et al.*, 1980; Littlewood S D *et al.*, 1988; Vancauwenberghe O *et al.*, 1992). In the case of silicon samples bombarded by O_2^+ ions, the altered layer thickness has been estimated to 4-4.5 nm/keV (Dowsett M G *et al.*, 1992). The detailed studies of using low energy for achieving higher depth resolution had been conducted by Clegg J B (1987), Wittmaack K *et al.* (1981) and in our group (Dowsett M G *et al.*, 1997). The thickness of the layer is also related to the primary ion beam incident angle. With a shallower angle, the layer is generally thinner, because less momentum is directed inwards. This advantage, however, may be compromised by loss in ion yield resulting in less sensitivity, as described previously. In practice, in SIMS depth profiling, the choice of primary incidence angle and energy for best depth resolution has to be considered together with the primary ion species and the sample composition, as well as the instrument type. Radiation-induced surface roughness (Stevie F A *et al.*, 1987; van der Heide P A W *et al.*, 2003), primary ion deposition (Wittmaack K, 1994) and surface contamination (Wittmaack K *et al.*, 1990) should also be taken in to account for obtaining a good depth profile.

Before the altered layer is stabilised, the sputter yield and ion yield will keep changing, and the signal acquired in this region cannot be correctly quantified in most cases. If there is a feature deliberately grown close to the surface, such as the ultra-shallow junction, other measures would be necessary to obtain a correct depth profile (Ronsheim P A, 2006).

2.1.3 SIMS instrumentation

2.1.3.1 Overview

All SIMS instruments can be viewed as consisting of three parts: (i) the SIMS sources comprising the primary ion guns with one or more ion sources,

and the sample, (ii) the mass analyser and the associated secondary ion optics, and (iii) the vacuum system.

There are generally three types of ion sources fitted with a SIMS primary ion column for dynamic SIMS: (i) gas phase sources, such as electron impact and plasma types operated with reactive or inert species, (ii) surface ionisation sources operated with caesium, and (iii) liquid metal (field emission) ion sources (LMIS), using species such as gallium. O_2^+ and Cs^+ ions are the most commonly used ion species for dynamic SIMS due to their merit of enhancing ion yield, and are produced by type (i) and (ii), respectively. LIMS sources are useful for high resolution imaging applications due to their high current density and small probe size (tens to hundreds of nanometres).

In most standard instruments, the sample is loaded in a sample introduction lock connected to the analysing chamber through a vacuum valve, which allows changing the sample without heavily influencing the vacuum in the analysing chamber (normally $\sim 10^{-9}$-10^{-10} mbar). Samples are generally a few mm on each side and fixed on a sample holder designed for good electrical conduction and ion extraction. The sample holder is shifted to the analysing chamber when vacuum allows, and sits on a manipulator stage, which is usually computer-controlled for desired position and angle with respect to the primary ion gun and/or the secondary ion optics. In some instruments, the sample stage can be rotated about the sample azimuth to reduce bombarded surface roughness (Skyes D E *et al.*, 1994). Some are also equipped with heating or cooling systems (Maier M, 1986).

Mass spectrometers that are used on SIMS instruments include the quadrupole mass spectrometer (QMS), the double focussing magnetic sector (DFMS) and the time-of-flight (TOF) spectrometer. Each of them according to its operating principle, has different merits and drawbacks, and thus may be better suited to particular applications. The choice of mass spectrometer dictates the design of extraction system and the sample environment. The secondary ion optics which usually sits in front of the mass spectrometer usually comprises ion extraction optics and an energy analyser. As many secondary ions as possible are extracted from the sputtered area. The energy analyser serves to select ions with suitable energy (QMS) or compensate the chromatic dispersion of the mass spectrometer (DFMS and TOF). (The effect that ions emerging from the same

point with the same angle but with different energy are imaged at different places along the optic axis with different magnifications is termed *chromatic aberration* (Fig. 3.2.2; Klemperer O, 1971)). Mass separated ion signals are converted into interpretable and manageable information by a detector and a data acquisition system. To achieve high dynamic range in a SIMS depth profile, ions are gated optically (DFMS and TOF) before being transferred into the energy filter or electronically (QMS) by the detector electronics, in order to reject ions emitted from the walls of the bombarded crater.

The QMS and TOF SIMS instruments have to conform to the ultra high vacuum (UHV) conditions, particularly in the sample analysing chamber. This is because the residual gas in the chamber can cover the sample surface, and consequently the background ion and sputter yields are altered. In the CAMECA IMS series of instruments (of the DFMS type), the distance between the sample and the extraction electrode is just 5 mm, and it is not possible to achieve UHV conditions over the sample because the pumping speed is very restricted. The pressure in the chamber can also influence the quality of the primary ion beam at the end of the ion gun where the final probe is formed (Dowsett M G, 2007). The pressure in the ion gun determines the beam current and the gun reliability.

2.1.3.2 Ion guns

Various types of ion gun have been developed to meet demands of SIMS applications. In general, a mono-energetic ion beam of a single species, single charge, carrying adequate current density within a well defined probe impacting the sample, is desirable. This is obtained first through optimising the selected ion source, in terms of ion species, lifetime, energy, beam current, optical and operational characteristics. Then a suitable transportation ion optics (ion column) must be designed to provide the desired beam spot, current and mass separation.

Electron impact sources, in which ionisation is produced by primary electron impact in a gas phase, can be found in many instruments for general and static SIMS applications. The most important designs of this type include the cross-beam ioniser (Nier A, 1947) and the oscillatory ion source (Nielsen K O, 1957). Cluster ion sources of this type have been developed recently to generate

ions such as Ar_{2000}^{+} (Yamada I *et al.*, 2001) and C_{60}^{+} (Wong S C C *et al.*, 2003). Note here Ar_{2000}^{+} means a singly-charged argon (Ar) cluster ion composed of 2000 Ar atoms, and similarly C_{60}^{+} a cluster carbon ion.

In plasma ion sources, the dense plasma created in the proximity of the anode aperture provides a very bright source of charged particles compared to electron impact sources. The *brightness* of an ion source is defined as the amount of ion current in a unit solid angle in a unit area, and is often expressed in A m^{-2} sr^{-1} (Klemperer O, 1971). The parameter is critical in obtaining adequate current density at the sample. Sources of this type are consequently very popular in dynamic SIMS applications. Amongst them, duoplasmatron ion sources, either using a hot filament or a cold cathode for plasma excitation, are most frequently used on modern standard SIMS instruments. Other sources include the Finkelstein types (Finkelstein A F, 1940), the radio frequency source (Newton G *et al.*, 1976) and the capillaritron (Mohoney J F *et al.*, 1981). Cluster ions such as SF_n^{+} (n = 1–5), have been produced from a duoplasmatron (Gillen G *et al.*, 1999). A duoplasmatron coupled with a surface ionisation source to produce a mixed beam of caesium and xenon is under investigation in Dowsett's group (Chang R J H *et al.*, 2005).

Surface ionisation ion sources are widely used to produce alkali metal ions, such as caesium (Alton G D, 1988). Caesium ions generated by this source type are usually of high current and low initial ion energy spread (0.2 eV). The latter attribute reduces chromatic aberration in the ion column. However, this type of source has low brightness.

The LIMS extracts ions from a high field region about the tip of a fine needle, wetted by the metal to be ionised. Thanks to its tiny probe size (tens to hundreds nanometres) with high current density, liquid metal ion sources are very useful for high resolution imaging applications. The first caesium LMIS was developed in 1984 (Prewett P D *et al.*, 1984). Positive gold cluster ions have been generated from this source (Davies N *et al.*, 2003).

Electron impact sources are usually coupled with an ion column that is designed to transport as many of the extracted ions as possible to the sample. The column usually consists of one or two Einzel lenses, and the probe size is between 0.1 and 3 mm. For plasma and surface ionisation sources, an ion column with a demagnifying optics system is usually used. This is performed

using one or more condenser lenses and an objective lens (Gerlach R, 1982). The probe size at the sample is typically < 100 μm. LMIS sources which have high brightness and very small optical object size usually require a unity or magnifying focussing system, and the formed probe size is less than 100 nm.

In most ion columns, mass separators, such as the Wien filter (Wien W, 1902) or a magnetic sector (Slodzian G, 1980), are employed to select the required charge to mass ratio (*e/m*) and to filter out undesirable ions. Mass resolution between 10 and 50 ($M/\Delta M$, ΔM being the width of the corresponding peak M in Dalton (Da) at its half-height) is often adequate. Neutral particles generated from ion sources need to be excluded from the ion beam. In general the ion column is bent at some point; in DFMS instruments, they are removed by the mass separator downstream to the ion sources. The ion beam may be raster-scanned at the end of the ion gun before reaching the sample (Hofer W O *et al.*, 1976) to provide uniform primary ion dose across the sputtered area.

2.1.3.3 Double focussing magnet sector

Double focussing magnetic sector (DFMS) is the oldest means of ion mass separation used in SIMS (Cataing R and Slodzian G, 1981). It is based on the principle that, in a uniform magnetic field, ions carrying the same charge and energy but heavier mass will travel along an arc trajectory of larger radius than lighter ones. But, because the majority of secondary ions to be collected normally have an energy spread of 10-20 eV, the incurred chromatic aberration would result in loss of ions and deteriorated mass resolution, if the aberration is not corrected. The general practice is to add an electrostatic sector in front of or behind the magnetic sector to compensate for the energy dispersion of the magnetic sector (Fig. 2.1.5). Thus, ions with the same mass, m, but a higher energy ($E+\Delta E$) and subsequently a higher velocity ($v+\Delta v$), enter the magnetic sector with an offset, and its trajectory is consequently corrected. Meanwhile, both sectors perform focussing action (directional focussing). As displayed in Fig. 2.1.5, the ion rays emitted from the object at the slit before the electrostatic sector, S_1, form an image at S_2, which is then projected by the magnetic sector to S_3. The mass spectrometer is a *double focus magnetic sector* in the sense that

ions with different energies at the same mass are focussed into one line through the combined action of the pair of sectors. The double focussing condition is that the energy dispersion of the magnetic sector be compensated by that of the electrostatic sector.

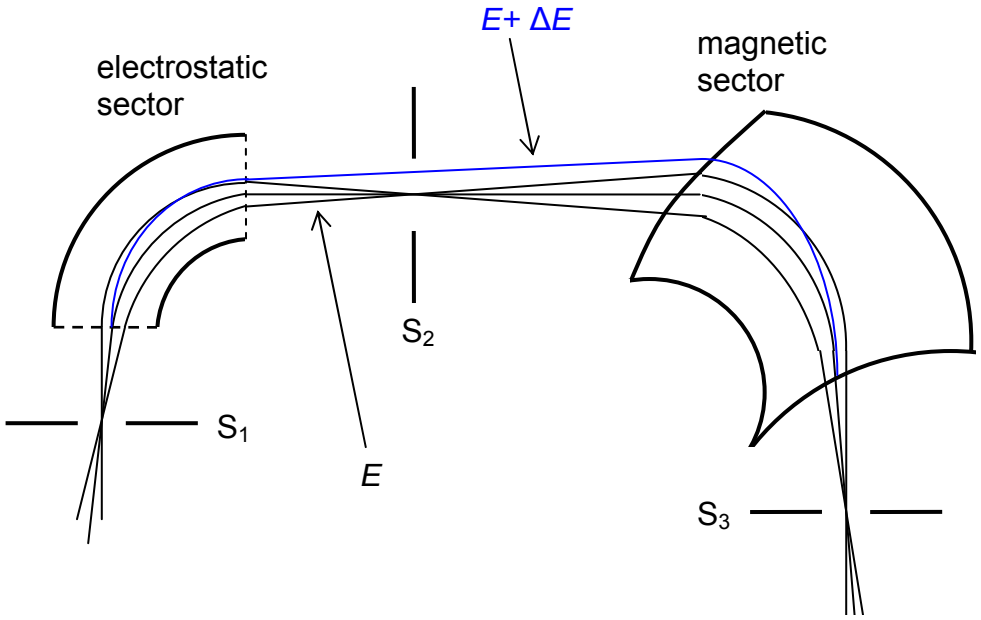

Fig. 2.1.5 Schematic diagram of a double focus magnetic sector. Ions with a mass, *m*, and an energy, *E*, emitted from the object at S_1 are imaged at S_2 by the electrostatic sector, and then S_3 by the magnetic sector. Ions with the same *m* but a different energy, *E*+*ΔE*, are corrected and focussed into the same line.

Due to the high pass energy of DFMS (several keVs), a strong extraction field (~keV mm^{-1}) can be applied above the sample surface and the resulting high collection efficiency is a common merit of DFMS. Other advantages include high mass resolution and broad mass range (up to several thousand Da). The broad bandwidth, ~150 eV, makes it easier to combat mass interference when the sample surface potential changes due to primary ion impact. However, when simultaneous electron bombardment is required for charge compensation on insulating layers and negative secondary ions are to be collected, DFMS instruments may be problematic. This is because the compensating low energy secondary electrons are collected by the secondary ion optics too, leaving the surface potential soaring up. The high extraction field also perturbs the primary ion beam, and the interdependence of primary ion energy and incidence angle makes DFMS instruments less flexible than QMS ones. Most DFMS instruments

have lower sampling rates (data points at small depth increments), which might result in loss of true depth resolution.

Conventionally, the high extraction field prevents the use of primary ion beams with impact energy (E_p) lower than 1.5 keV. Low energy beams are easily defocused and deflected that the current density is not uniform across the bombarded crater, and the obtained profile is distorted. In 1992, a non-linear extraction field (NLEF) was devised for the Kratos S1030 instrument (Dowsett M G *et al.*, 1992), which allows E_p down to 500 eV at full extraction potential (5 keV). Another design of a split extraction field plus a deflector in the primary column by Bayly A R and Dowsett M G on a VG IX70S instrument, permits E_p = 700 eV with variable incidence angles (50 ^{o} -75 ^{o}) for the O_2^+ ion beam (Jiang Z.-X. *et al.*, 1997). Nevertheless, in the case that primary and secondary ions are of opposite polarity (e.g. Cs^+ used to sputter secondary As^-) sub-keV E_p was still lacking, until the CAMECA company in 2000 revealed a new instrument – CAMECA IMS Wf (Chambost E de *et al.*, 2000). This instrument is equipped with a floating type primary column, based on the same principle as the FLIG^{TM} (Dowsett M G *et al.*, 1996) used on QMS instruments, coupled with a new secondary ion extraction system. The extraction is screened and a field free region above the sample surface is thus provided. $E_p \leq 250$ eV has been achieved for both polarity extraction on this instrument.

2.1.3.4 Time-of-flight mass spectrometer

Time-of-light (TOF) instruments (Chait B T *et al.*, 1981; Benninghoven A, 1983) measure the time spent by an ion travelling from the sample surface to the detector. For ions carrying the same energy (E), the light ions reach the detector sooner than the heavy ones through a fixed path (L),

$$t = \frac{L\sqrt{m}}{\sqrt{2E}}. \qquad \text{(Eqn. 2.1.1)}$$

The primary ion source is pulsed to allow for the time required for secondary ions to fly to the detector. There are three aberrations that contribute to the limit of mass resolution, including the pulse time of the primary source (Δt_{is}), the time analyser aberrations (Δt_{an}) and the minimum time resolution of the detector (Δt_{det}),

$$\frac{m}{\Delta m} = \left[\left(\frac{2\Delta t_{is}}{t} \right)^2 + \left(\frac{2\Delta t_{an}}{t} \right)^2 + \left(\frac{2\Delta t_{\det}}{t} \right)^2 \right]^{-\frac{1}{2}}. \qquad \text{(Eqn. 2.1.2)}$$

The initial kinetic energy distribution of secondary ions are corrected by means of energy compensation such as reflectron as shown in Fig. 2.1.6, where ions having higher initial energy penetrate more deeply into the reflectron and thus spend more time. TOF instruments also apply high extraction fields (~ kV mm^{-1}) like DFMS to obtain good time resolution.

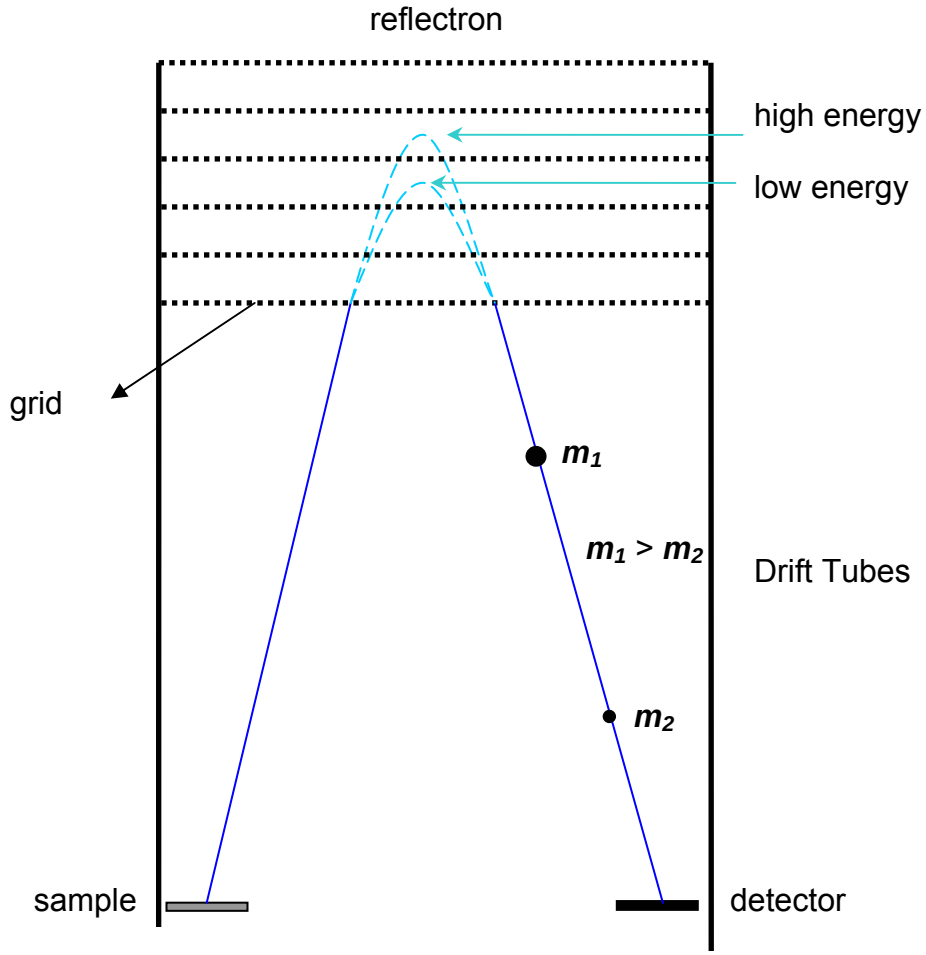

Fig. 2.1.6 Schematic diagram of a TOF SIMS with a reflection analyser. Secondary ions are reflected in the reflectron for energy compensation and time discerned by a detector.

Since virtually there is no limit on mass range, it is particularly advantageous for applications with polymer or organic materials. The instrument allows all ions to be detected (parallel detection), without the necessity of mass scanning as on QMS and DFMS, which provide more information for analysis. TOF also has high transmission (10%-50%) and high mass resolution ($m/\Delta m > 10^4$). However, owing to the required duty cycle (10^{-4}-10^{-5}), TOF instruments conventionally were limited to the use of static SIMS. To erode the sample for tasks of depth profiling, the time would be > 1000 times longer than with a continuous beam. Ten years ago, a dual-beam method was developed in Benninghoven's group, which improves the depth profiling capability of TOF instruments (Iltgen K *et al.*, 1997). This is done by directing a second beam for erosion during the secondary ion flight time. The second beam is usually low energy (for high depth resolution), high current density (for quick erosion), and of reactive species such as Cs^+ or O_2^+ to enhance ion yields. The primary analysis beam is usually a keV gallium ion beam, which produces a well defined analysis area. Although applications of depth profiling on TOF instruments, down to sub-keV, have been realised by this method ever since, one would still have to consider the loss of data points in a given depth interval which may result in errors of dosimetry measurements (Dowsett M G, 2003).

2.1.3.5 Quadrupole mass spectrometer

The quadrupole mass spectrometer (QMS) was first devised in 1953 (Paul W and Steinwedel H, 1953). The inhomogeneous oscillatory electrical field that is formed inside the spectrometer permits a transmission path for ions with a specific *e/m* ratio. Theoretically, this field is to be produced by four electrically conducting rods with hyperbolic surfaces and infinite length, placed in parallel. However, in practice rods are limited to a certain length, because long rods are rather heavy and occupy more space (never mind that ions would not be able to come out from an infinite quadrupole set). Besides, circular cylindrical rods are normally used, instead of hyperbolic ones, because they are cheaper. For best approximation of the field near the optic axis, the radius of the

rods, r, should be 1.145 times that of the circle inscribed by these four rods, r_o; namely, $r \approx 1.145 r_o$ (Fig. 2.1.7, Dowson P H, 1976). Each pair of electrodes is applied a combination of a stationary voltage, V_{dc}, and a radio frequency alternative voltage, V_{ac}, but with opposite polarity,

$$V = \pm[V_{dc} + V_{ac} \cos(2\pi f t)] . \qquad \text{(Eqn. 2.1.3)}$$

The hyperbolic field makes ions with the desired *e/m* ratio undergo an oscillatory trajectory along the optic axis and be transmitted through the spectrometer, whilst ions with other ratios move away from the axis and hit any surface inside the QMS.

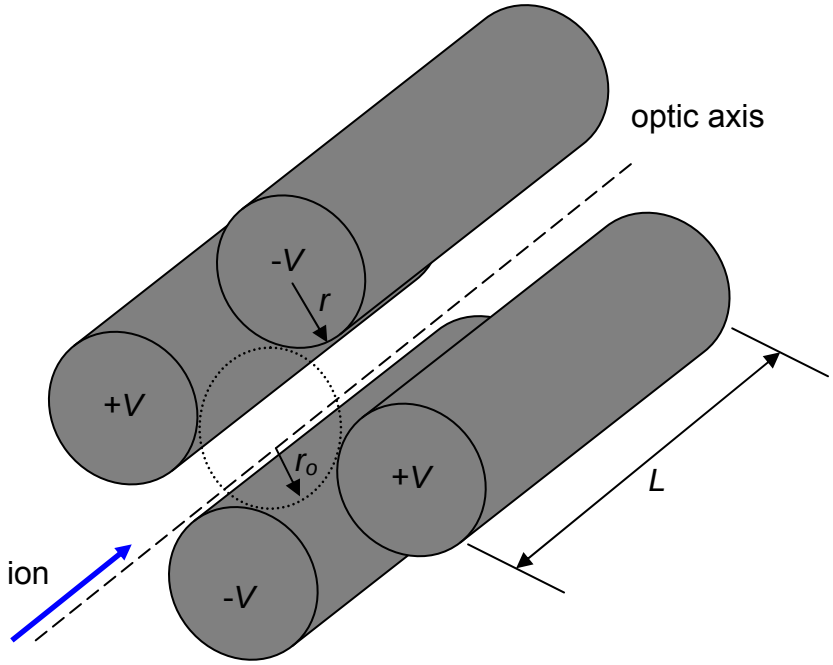

Fig. 2.1.7 Schematic diagram of quadrupole mass spectrometer. Two pairs of cylindrical electrodes are applied a potential V but with opposite polarity.

For ions with the desired *e/m* ratio which enter the spectrometer parallel to the optic axis, the entrance aperture size a of the QMS is limited to

$$a \le \frac{2}{3} r_o \left(\frac{\Delta m}{m} \right)^{\frac{1}{2}}, \qquad \text{(Eqn. 2.1.4)}$$

in order to prevent the ions striking electrodes inside the QMS. Likewise, ions with the desired *e/m* ratio that enter the QMS on the optic axis have a limited traverse momentum, $\vec{P}_t$, for transmission (Paul W *et al.*, 1958),

$$\vec{P}_t \le mf\vec{r}_o \frac{\Delta m}{m}. \qquad \text{(Eqn. 2.1.5)}$$

In practice, the QMS is operated in between two modes: the fixed *Δm* mode or the fixed *Δm*/*m* mode (Jede R *et al.*, 1992), with the mass resolution determined by

$$\frac{\Delta m}{m} = \frac{(0.16784 - C_1) + C_2 / V_{ac}}{0.126}, \qquad \text{(Eqn. 2.1.6)}$$

and

$$V_{dc} = C_1 V_{ac} - C_2. \qquad \text{(Eqn. 2.1.7)}$$

If the fixed *Δm* mode were chosen, there would be less transmission for ions with heavy mass (Eqn. 2.1.4). Conversely, the fixed *Δm*/*m* mode hinders the light-mass ion transmission (Eqn. 2.1.5).

Ions must stay in the field long enough to ensure mass separation, which leads to the determination of the QMS pass energy that is about 10 eV. The pass energy, E_{pass}, is determined by the rod length, frequency and mass resolution (Paul W and Steinwedel H, 1953):

$$E_{pass} < 0.04 f^2 L^2 \left(\frac{\Delta m}{m}\right) m. \qquad \text{(Eqn. 2.1.8)}$$

An optics system is thus put in front of the mass spectrometer to filter out ions with excessive energy, and neutrals. The other purpose of this optics is to provide linear magnification and angular demagnification to improve the collection efficiency.

QMS has a small energy bandwidth, ~15-20 eV, which makes QMS SIMS instruments very sensitive to sample surface potential change and a correction procedure is required (Dowsett M G *et al.*, 1986). However, due to its low extraction field (a few V mm^{-1} above the sample is sufficient for secondary ion collection), the primary ion beam is barely perturbed by the extraction field, and a very flat crater can be obtained down to sub-keV energies. The resultant independence between the primary impact energy and incident angle makes

QMS greater than the other two for fundamental studies and the establishment of best analytical conditions for a specific job. On the other hand, strict symmetry between the sample and the secondary ion optics is not necessary unless optical gating is required. Other advantages of QMS include its smaller size, lighter weight and ease of operation. Although QMS usually has smaller transmission, lower mass resolution and smaller mass range in comparison with DFMS and TOF, it is as sensitive as TOF for dynamic SIMS. This is because the use of the dual-beam method cannot avoid loss of data points (section 2.1.3.4).

In 1996 sub-keV depth profiling was first accomplished on a QMS instrument by the invention of the floating low energy ion gun, FLIG, in Dowsett's group (Dowsett M G *et al.*, 1997).

2.2 Cluster SIMS and cluster ion sources

2.2.1. Review of cluster ion bombardment

A cluster ion is an ion consisting of more than one atom. For example, the commonly used O_2^+ is a cluster (dimer) ion, and its counterpart Cs^+ ion is an atomic ion. Cluster ions are also referred to as molecular or polyatomic ions in the literature.

A significant observation for surfaces under cluster ion bombardment is the nonlinearity of sputter yield, which now is generally referred as the nonlinear (or non-additive) enhancement factor (Belykh *et al.*, 1997),

$$K_n = \frac{Y_n}{nY_1}, \qquad \text{(Eqn. 2.2.1)}$$

where n is the number of constituent atoms in a (primary) cluster ion and Y_n the secondary sputter (or ion) yield due to primary ion impact. The energy carried by each constituent atom is generally referred to as E_0. E_0 is the same for identical atoms, e.g. in the case of an O_2^+ ion, and different for different atoms, e.g. a sulphur fluoride SF_6^- ion. If a 3 keV trimer gold cluster ion (Au_3^-) sputters 9 silicon (Si) atoms out of a surface, and a 1 keV monomer gold ion (Au_1^-) sputters 1 silicon atom (both ions have the same E_0 = 1 keV), then

$$K_3 = \frac{9}{3 \times 1} = 3, \qquad \text{(Eqn. 2.2.2)}$$

provided other conditions are the same. In the other words, each gold atom in an Au_3^- cluster ion is 3 times as effective as an atomic Au_1^- ion in sputtering. This effect was firstly reported by Andersen H H and Bay H L (Andersen H H *et al.*, 1974-1975). In their work, cluster ions of chlorine ($^{35}Cl_n^+$), selenium ($^{79}Se_n^+$) and tellurium ($^{128}Te_n^+$) with n = 1-2, E_0 = 30-260 keV were used to bombard targets made of silicon, silver and gold. It was also found the nonlinearity is more pronounced for heavy projectiles and targets.

Later, a similar result was reported at a lower ion energy range, E_0 = 15-45 keV, by Thompson and his co-workers (Thompson D A *et al.*, 1979). The ions used include phosphorus (P_n^+), arsenic (As_n^+), antimony (Sb_n^+) and bismuth (Bi_n^+) with n = 1-3, and targets of silver, gold and platinum were

bombarded. The nonlinearity was explained by the overlapping of cascades at the surface that causes sample surface disruption and lower surface binding energy.

The nonlinearity of secondary ion yield was first studied in 1979 by Wittmaack (Wittmaack K, 1979), who bombarded a Si sample with dimer noble gases (argon, xenon, krypton and neon) in the energy range E_0 = 5-7 keV.

Bombardment of cluster ions on organic materials was first performed by Appelhans and Delmore (Appelhans A D and Delmore J E, 1989), using 8 keV Cs^+ and $SF_6^{0,-}$ particles to bombard four common pharmaceutical compounds. Beside the enhanced molecular secondary ion yields, they found the increase of chemical damage due to cluster bombardment was outweighed by the enhanced yield, which means a net gain of sensitivity for retrieval of molecular information.

Blain *et al.* conducted a study of the dependence of enhanced secondary ion yields on primary ion nuclearity – the number of constituent atoms in a cluster projectile (Blain M G *et al.*, 1989). 5-28 keV caesium iodide ions ($(CsI)_nCs^+$, n = 0-2) were used to bombard various samples, such as phenylalanine ($HO_2CCH(NH_2)CH_2C_6H_5$), gold and caesium iodide. The results show that the secondary ion yields increased proportionally to the square of the projectile velocity and nonlinearly with increasing projectile nuclearity. Moreover, the yield enhancement is more pronounced for (secondary) molecular ions than for atomic ones.

The dependence of secondary ion yield nonlinearity on the charge state of both primary and secondary ions was investigated by Szymczak and Wittmaack in 1994 on silicon samples (Szymczak W and Wittmaack K, 1994). The ions used were 27–33 keV Xe^+, $SF_5^{\pm}$ and SF_6^-. They discovered that the yield enhancement depends very weakly on the charge state of the projectile, and is larger for negative than for positive secondary ions.

Belykh *et al.* conducted a series of studies on samples made of metals and semiconductors (Belykh *et al.*, 1992, 1997, 1998, 2000a, 2000b, 2001, 2003a, 2003b). Cluster ions including Au_n^- (n = 1-5), Si_n^- (n = 1-6), copper (Cu_n^-, n = 1-3) and aluminium (Al_n^-, n = 1-2), carrying E_0 = 4-18 keV, were used to bombard samples of silicon, niobium, tantalum, indium gallium phosphide and gallium arsenide doped with an aluminium delta layer. Nonlinearity of

secondary ion yields was found in all cases (as big as *n* to several orders). It was also found the yield enhancement is more pronounced for (secondary) molecular ions than atomic ones (Fig. 2.2.1). In addition, studies of secondary ion energy distributions were performed, and the results suggest a different desorption mechanism of secondary particles under cluster bombardment. Heinrich later performed similar experiments, and demonstrated that the enhanced secondary ion yields are due to enhanced desorption mechanism rather than enhanced ionisation probability (Heinrich R *et al.*, 2000, 2002-2003).

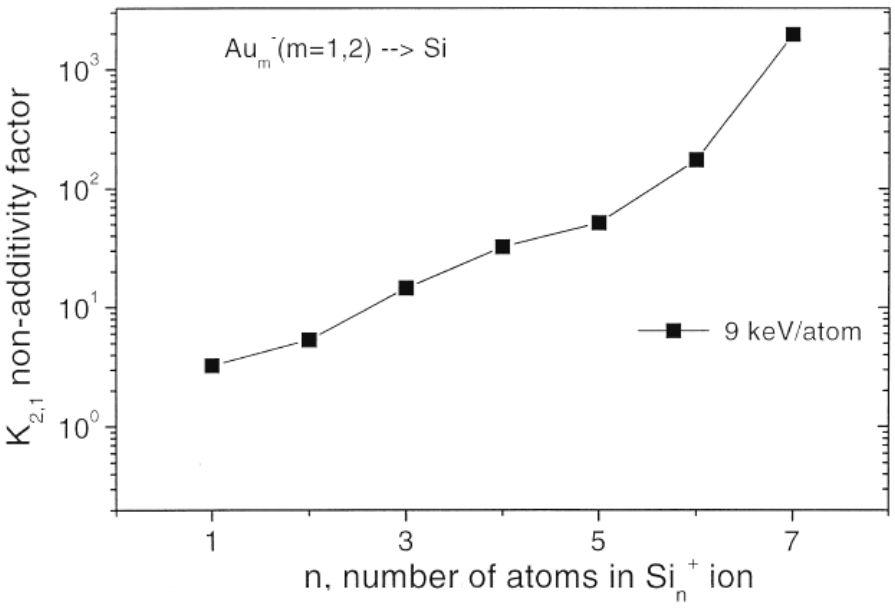

Fig. 2.2.1 Yield enhancement due to cluster ion bombardment increases with secondary ion nuclearity (reproduced from Belykh S F *et al.*, 2001). Secondary Si_n^+ ions were sputtered by Au_m^- projectiles with $E_0 = 9$ keV. The $K_{2,1}$ shown in the figure is the K_2 as defined in Eqn. 2.2.1.

The success of molecule SIMS depth profiling was first demonstrated by Gillen and his co-workers in 2001 (Gillen G *et al.*, 2001). Molecular ion signals from organic films were stable with the increase of dose of primary carbon cluster ions (C_n^-, n = 6-10), which had never been attained by atomic projectiles. Similar effects were observed with SF_5^+ (Mahoney C M *et al.*, 2004; Wagner M S, 2005) and C_{60}^+ projectiles (Cheng J *et al.*, 2005).

In summary, bombarding the surface of metals, semiconductors and organic materials by cluster ions has been found to enhance sputter and ion

yields compared to atomic ions. The nonlinear enhancement factor K_n, as defined in Eqn. 2.2.1, has been found to vary from n to 20000 and depends on the ion-sample combination. The enhancement is usually more pronounced for large secondary ions, and thus cluster ions have been widely applied to organic material analysis. The net gain of sensitivity for retrieval of molecular information makes cluster ions suitable for high-resolution molecular imaging analysis (Kollmer F, 2004). Molecular depth profiling has also become possible through the use of cluster ions.

2.2.2 Cluster ion sources developed for SIMS analysis of semiconductors and metals

To gain a general understanding of the applicability of cluster ions to SIMS analysis of semiconductors and metals, particularly in the branch of depth profiling, several cluster ions sources that have been applied to these materials are reviewed here. This includes sources that generate SF_n^+, C_n^-, CsC_n^-, Au_n^-, C_{60}^+ and large cluster ions such as Ar_{2000}^+. The Au_n^- source described here is a separate work from our work – SCIS. The history and previous study of the SCIS will be detailed in Chapter 3.

2.2.2.1 SF_n^+ (n = 1-5) and F^- ion source

A hot filament duoplasmatron ion source (Vályi L, 1977) was adapted to produce sulphur fluoride (SF_n^+, n = 1–5) and fluorine (F^-) ion beams, at National Institute of Standards and Technology, USA (Gillen G *et al.*, 1999). It was so designed such that SF_6 gas can be introduced into two regions of the duoplasmatron, namely the *pinch region* (between the intermediate electrode and anode), and an *expansion cup* mounted at the extraction side of the anode (Fig. 2.2.2). However, it was reported that only in the latter case were stability of the source and the beam obtained. The additional cup was so designed that it can be electrically floating or biased, with a higher current acquired in the latter case.

The SF_5^+ ion beam was reported to have maximum current of 200-300 nA and current density of 0.5 mA cm^{-2}, with a lifetime of 70 hours. The beam spot size was not specified in the paper and was estimated here to be Ø 226 μm-Ø 339 μm. The F^- ion beam has a maximum current of 3 μA and a lifetime of 1-2 days. The stability of the SF_5^+ ion beam was established by monitoring the secondary ion SiF^+ signal, which had a standard deviation of 0.8 % in a period of > 50 minutes. The stability of the F^- beam was not stated, although from a depth profile it seems to be stable for more than 1 hour (Fig. 2.2.3).

The SIMS applications of the ion beams were performed on a CAMECA IMS 3f/4f instrument. Secondary ion yields from organic materials were enhanced by the 5.5 keV SF_5^+ beam when compared to a 5.5 keV Ar^+ beam. The depth resolution of a sample consisting of nine alternating layers of chromium (53 nm) and nickel (66 nm) was improved by the 3 keV SF_5^+ beam when compared to a 3 keV O_2^+ beam (incidence angle θ not specified). This was explained by the improved surface roughness (a factor of 6) and the lower projectile penetration depth attributed to the SF_5^+ beam. Besides, it was stated that, with oxygen flooding during analysis, an improved decay length of low energy boron implant profiles by almost a factor of 2 as compared to O_2^+ bombardment was obtained (the energy used is not specified). Nevertheless, this application has the drawback that the useful ion yield was reduced by a factor of 3. The SF_5^+ beam when reduced to a total current of 10 pA with a micrometer-sized spot also proved adequate for the application of SIMS imaging. The advantage of the negative F^- beam was stressed in the SIMS insulating material analysis.

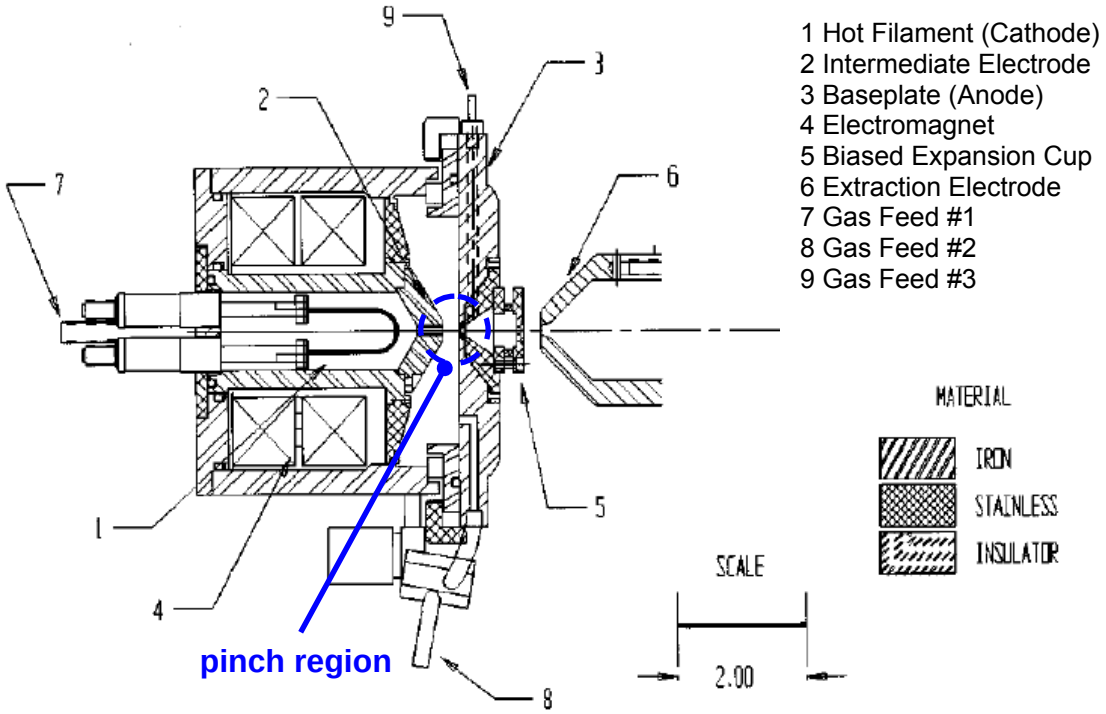

Fig. 2.2.2 Mechanical drawing of the hot filament duoplasmatron ion source modified for operation as a triplasmatron (reproduced from Gillen G *et al.* 1999). The SF_6 gas was fed through the *Gas Feed #2* as indicated into the *pinch region*, and the *Gas Feed #3* into the *expansion cup*. The scale was not specified in the paper, but should be in inch as is commonly used in the U.S.

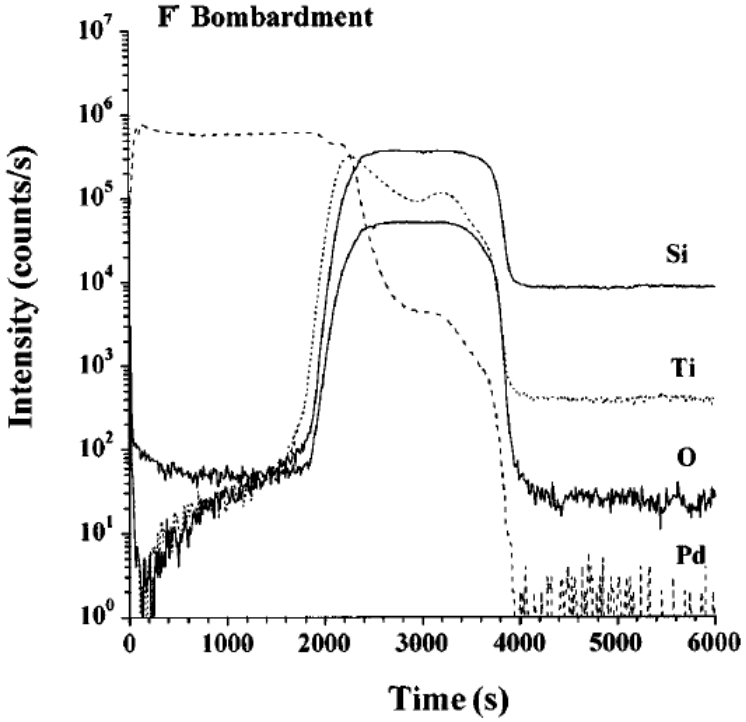

Fig. 2.2.3 Depth profiles of a Pd/Ti/SiO2/Si film by F^- ions (reproduced from Gillen G *et al.* 1999).

2.2.2.2 C_n^- (n = 4-10) and CsC_n^- (n = 2-8) ion source

A commercial sputter ion source (Peabody Scientific PSX–120) was used to generate C_n^- and CsC_n^- ions by sputtering a graphite sample by caesium ions, at National Institute of Standards and Technology (Gillen G *et al.*, 2001). The current of the C_2^- ion beam was > 1 μA, and that of C_n^- (n = 4-10) and CsC_n^- (n = 2-8) was several tens of nA, through a CAMECA 4f primary column. The stability of the source is a few percent over 20 minutes with a general trend of decreasing primary current and degrading beam focus. Under optimal conditions the beam current density was measured 0.4-0.5 mA cm^{-2}.

Enhancements of molecular secondary ion yields and the improved possibility of SIMS depth profiling on organic samples by the cluster ions were reported in the same paper. The depth resolution of a 1 keV arsenic implanted Si depth profile was improved by a factor of 4 under the 3 keV CsC_6^- ion bombardment as compared to the routinely used 3.6 keV Cs^+ ions. However, formation of surface topography was observed with the CsC_6^- ion bombardment, which did not happen with Cs^+ ions.

2.2.2.3 Large gas cluster ion source

A large gas cluster (< 6000 atoms/ion) ion source was designed and built in Kyoto University, Japan (Yamada I *et al.*, 2001). Basically the cluster formation process involves a gas expanding from a high pressure source into vacuum through a small orifice. Adiabatic expansion reduces the relative velocity of the gas atoms and thus clusters are formed. The cluster beam is then ionised by electron impact and collimated. Ar_{2000}^+ and $(SF_6)_{2000}^+$ ions can be produced by this source.

20 keV Ar_{2000}^+ ions were used to irradiate samples of silicon, titanium, copper, zirconium, silver (Ag), tungsten and gold. As a result, the sputter yield was enhanced by one order of magnitude as compared to 20 keV Ar^+ ion bombardment. Amongst the samples, Cu, Ag and Au had higher yield enhancement, which was explained by the lower binding energies. The angular distribution of Ar_{2000}^+-sputtered Cu atoms (Fig. 2.1.2) differs from the cosine law

distribution as predicted by the linear cascade collision theory, and this phenomenon was attributed to a dense collision cascade (a *spike*).

Compared with the Ar_{2000}^{+} ion irradiation, the enhanced sputter yields by $(SF_6)_{2000}^{+}$ ions were attributed to the reactive sputtering effect – more volatile fluoride compounds are produced under the $(SF_6)_{2000}^{+}$ bombardment which can then be physically sputtered or thermally evaporated from the surface. The angular distribution of $(SF_6)_{2000}^{+}$–sputtered Au atoms had a similar secondary atom angular distribution to that of $Ar_{2000}^{+} \rightarrow$ Cu. Nevertheless, in the case of $(SF_6)_{2000}^{+} \rightarrow$ W, a cosine law is obtained, which was attributed to the chemical reaction between W and F. Both species are reported to lead to very good surface smoothing effects on various industrial materials, such as Cu films on Si substrates. The authors also reported this source can be easily adapted for large $(O_2)_n^{+}$ ion emission to take advantage of the well known matrix effects of oxygen.

2.2.2.4 C_{60}^{+} ion source

A commercial C_{60}^{+} source (IonOptika, Model IOG-C60-10) was tested for the SIMS application on semiconductor depth profiling, performed on a CAMECA IMS 4f (Gillen G *et al.*, 2006). The C_{60}^{+} ions are produced by electron impact on C_{60} vapour. It was reported that the deposition of an amorphous carbon layer was formed on the sputtered Si surface with an impact energy of 3-12.3 keV, with various incident angles, and the initiation of carbon deposition depended on the impact energy/incident angle and the current density. This is partially explained by the strong covalent bonds between silicon and carbon. The 14.5 keV C_{60}^{+} beam (240 eV/atom), which provided a sputtering effect (rather than deposition), was then used to depth profile arsenic (As) and boron (B) delta-doped silicon samples, and the results were found to be worse than the conventional use of 500 eV Cs^{+} (As delta) and O_2^{+} (B delta) ion beams.

2.2.2.5 Au_n^- (n = 1-3, 5) ion source

A caesium sputter Au_n^- cluster ion source was designed in the University of Duisburg-Essen, Germany (Samartsev A V and Wucher A, 2006). The source can generate Au_1^-, Au_2^-, Au_3^- and Au_5^- ions at currents of 100, 10, 10, 1 nA, respectively, into a spot size of about Ø 1 mm through a TOF-SIMS primary column. The ions were employed to bombard a polycrystalline indium sample. The TOF-SIMS system allows detections of both secondary neutrals and ions. It was concluded the cluster-induced secondary ion enhancement from metals is due to a more effective sputtering mechanism rather than a more effective ionisation process, in contrast with semiconductors (Wittmaack K, 1979). The ionisation probability was reported to increase with the size of secondary ions.

To date, the results published in the literature indicate that improved depth resolution can be attained, in the (total) energy range ≥ 3 keV, by the use of certain cluster ions. However, this merit may be counteracted by the accompanying disadvantages such as surface topography, reduced useful ion yield and primary ion species deposition. In general, the use of cluster ions for SIMS depth profiling is still believed to be inferior to the traditional ultra low energy (≤ 1 keV) SIMS employing O_2^+ and Cs^+ ions (Gillen G, 2007).

2.2.3 Silicon bombarded by gold ions

Silicon will be used in this work for studies of ion-solid interactions, such as sputtering and bombarded surface topography. Previous studies of silicon bombarded by gold cluster ions are reviewed here. Attributes such as sputtering, deposition, ion yield, ion-induced damage are addressed. Research on bombardment induced topography was not found in the literature.

In 1993 Nagamachi and his co-workers (Kyoto, Japan) developed a liquid metal ion source (LMIS) to emit a Au^+ focused ion beam (FIB) for the application of fabricating submicron metal patterns on Si substrates (Nagamachi *et al.*, 1993). Gold deposition was attained in the energy range of 34-194 eV ($\theta = 0^o$). The deposition was found to be inversely proportional to the ion energy,

and a "*sticking probability*" was defined as the probability of an Au^+ ion depositing on the Si substrate as a function of Au^+ ion energy. Extrapolation of the reported data indicates that for $E_0 \geq 0.2$ keV the sticking probability is about zero and sputtering should occur. However, in the ion gun they used there is no neutral dump (Fig. 2.2.4). Therefore neutral particles could also contribute to the deposition.

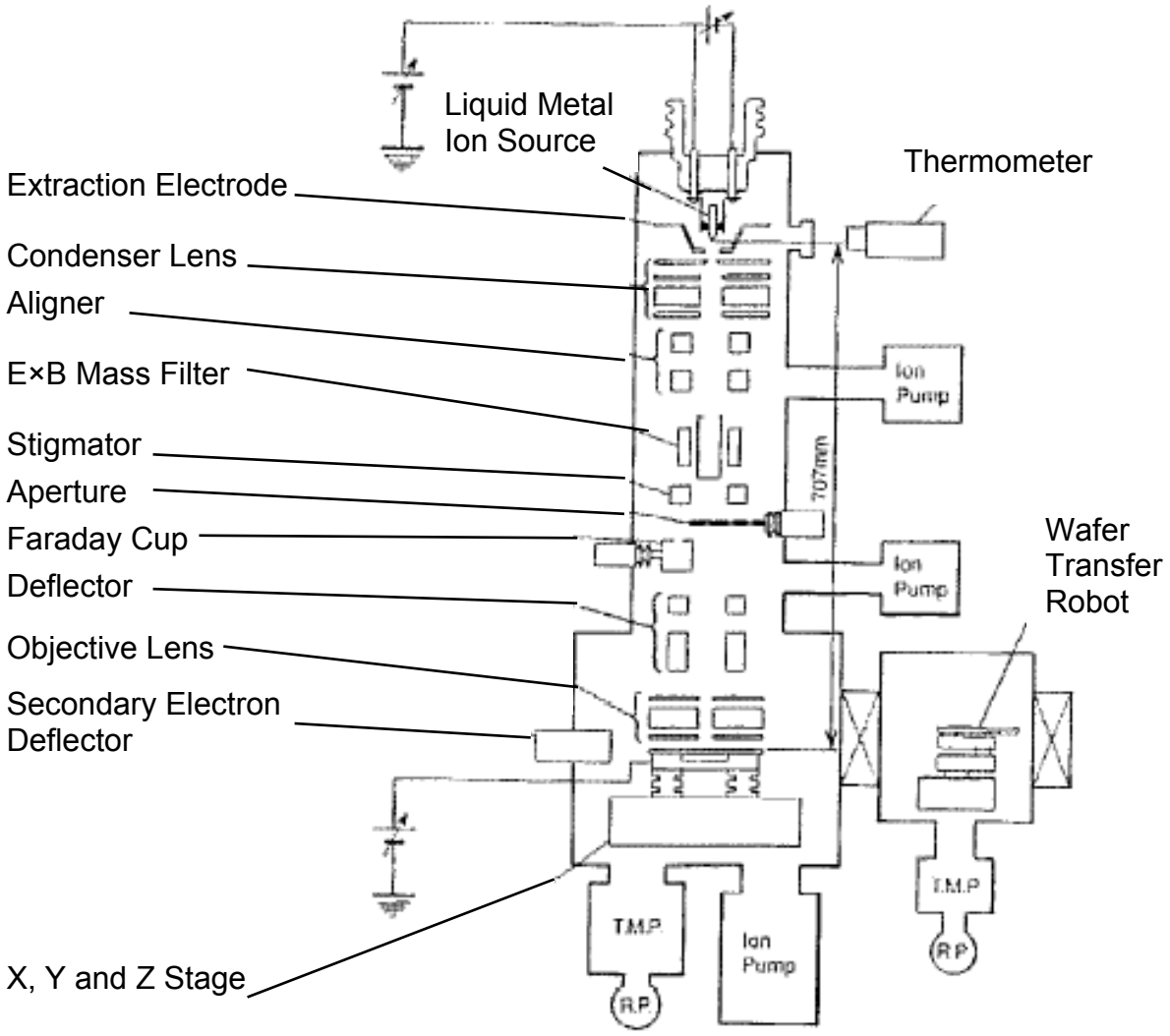

Fig. 2.2.4 Schematic diagram of the low energy focussed ion beam direct deposition apparatus developed by Nagamachi *et al.* (reproduced from Nagamachi *et al.* 1993). No neutral dump is shown, nor described in the paper.

Other work, performed also with an Au_n^+ (n = 1-5) LMIS, shows the dependence of sputtering on gold atom dose, on samples of mono-crystalline

silicon (Döbeli M *et al.*, 1997). For a 30 keV Au_3^+ beam (θ not specified), in the dose range 0-2×10^{15} Au cm^{-2}, deposition was detected. In the dose range 2×10^{15}-5×10^{17} Au cm^{-2}, sputtering was detected, being proportional to the dose. Nonlinear sputtering was reported with $E_0 = 10$ keV and dose 5×10^{17} Au cm^{-2}: $K_2 = 1.08$ and $K_3 = 1.23$. Ion radiation damage was measured by thermal wave analysis (TWA). The results show the damage does not depend on cluster nuclearity, in the conditions of dose 1×10^{11}-5×10^{12} Au cm^{-2}, E_0 = 6-10 keV. In the other words, the damage is linear, i.e. being proportional to the dose irradiated on the sample surface.

Nonlinear damage, however, was discovered in the work conducted in Houston, USA, with a negative gold cluster ion source (Liu J R et al., 2002). The source, based on Billen's design (Billen James H, 1981), generates negative gold ions by sputtering a gold target by Cs^+ ions, the same operating principle as ours. Radiation damage induced by gold ions on mono-crystalline Si wafers was characterized by Rutherford backscattering spectrometry/channeling (RBS) in the number of Si atom displacements per Au atom. With $E_0 = 6$ keV (θ not specified) and the dose of 8×10^{12} Au cm^{-2}, the damage increased with the ion nuclearity, contrary to Döbeli's report. This nonlinear effect was discovered to be dependent on dose in the use dose range, 8×10^{12} to 1.2×10^{15} Au atoms cm^{-2}. At higher doses, sputtering and overlapping of the damage reduce the defect per Au atom, therefore reducing the nonlinear effect. The disagreement with Döbeli's work was explained by the difference in measurement techniques, regardless the difference of ion polarity – the RBS technique is very sensitive to the disorder in the uppermost layer under the surface, whilst the TWA one is sensitive down to several microns.

The nonlinearity of Si_m^+ (m = 1-17) ion yields induced by Au_n^- (n = 1-3) bombardment was studied in details by Belykh and his co-workers (Belykh S F *et al.*, 2001). This negative gold cluster ion source, as the prototype of the source used in our work, will be described in Chapter 3. Mono-crystalline silicon was bombarded using $E_0 = 9$ and 18 keV, $\theta = 45^{\circ}$. The secondary ion yields, normalised to corresponding primary ion current, were found to increase with E_0 and n. The ion yield enhancement factor K increased with m, for example $K_2 = 2.5$, 40, 200 for Si^+, Si_4^+, Si_6^+. Ratios of (secondary) atomic ions to cluster ions decreased when n increased.

Al_n^- (n = 1-2) ions were generated from the same source and studied. The nonlinearity was much less than gold ions, particularly for secondary cluster ions. For example when E_0 = 9 keV, K_2 = 1.7, 2 for Si^+, Si_4^+. Besides, larger ions such as Si_m^+ ($m > 4$) could not be observed. When E_0 was reduced to 6 keV, K_2 increased to be 2.1, 25 for Si^+, Si_4^+. It was thus suggested that for any given combination "molecular projectile-target", there exits an optimal value of E_0 which leads to maximum K.

Simulation of nonlinear sputtering of silicon by gold and aluminium clusters was investigated by Medvedeva in Pennsylvania State University (USA) (Medvedeva M *et al.*, 2003). The factor K_2 was found to be 7.0 for gold and 1.7 for aluminium, in the conditions: E_0 = 1.5keV, $\theta = 45^{\circ}$. Besides, K_2 is higher for secondary clusters, particularly in the case of gold bombardment where K_2 = 10.8 for clusters and 1.1 for monomers (Note: in this paper, all secondary particles consisting of more than one atom are counted as clusters). The ratio of cluster-yield/total-yield is 0.94 by Au_2 bombardment, compared to 0.6 by Au_1. Au_2 is better than Al_2 in terms of sputtering. Besides, the simulation shows that at 28 fs after impact, Au_2 remains as a dimer at 2-4Å under the surface, whilst Al_2 atoms quickly disintegrate and act individually thereafter, and are distributed at 8-16 Å under the surface. Consequently, Au_2 bombardment results in more localised energy deposition and increases surface specificity for the emission of atoms or clusters.

Chapter 3 The Instrument and Ion Source – Overview

3.1 EVA 2000

The EVA 2000 SIMS instrument (Fig. 3.1.1), on which the sputter cluster ion source (SCIS) is tested, improved and characterised, was designed and built in 1980 by Dowsett. The instrument has been being improved to keep up with the development of material growth and doping technology (Cooke G A, 1992).

The instrument now has a floating low energy ion gun (FLIG) as its primary column, which will be detailed in section 3.2. Secondary ions are extracted and energy filtered by a parallel plate energy analyser based on the type developed for the DIDA SIMS instrument (Wittmaack K, 1982). The relatively weak secondary ion extraction field makes it suitable for the use of low energy primary beams. The mass analyser is a quadrupole mass spectrometer produced by Extracnuclear Laboratories Ltd., model 162-8. The rods (Ø 19 mm) are operated at 1.5 or 3 MHz, giving a mass range of 0-200 Da or 0-30 Da respectively. The mass analysed ions are detected by a channeltron (Galileo 4816), which multiplies the signals by a factor of ~ 10^8. The multiplied signals are counted and fed into a computer system.

The vacuum which can be achieved in the sample analysis main chamber (MC) (Fig. 3.1.2) is 1×10^{-10} mbar after 24-36 hours of baking. The MC is normally firstly evacuated by the load lock (LL) pumping system to about 10^{-7} mbar and then by an ion pump to 2×10^{-9} - 1×10^{-10} mbar. Both the LL and

the FLIG are evacuated first by a rotary pump and then a turbomolecular pump. In between the LL-MC and FLIG-MC there is a valve for maintaining the vacuum in the MC whilst samples are being loaded and the FLIG or the SCIS is being serviced.

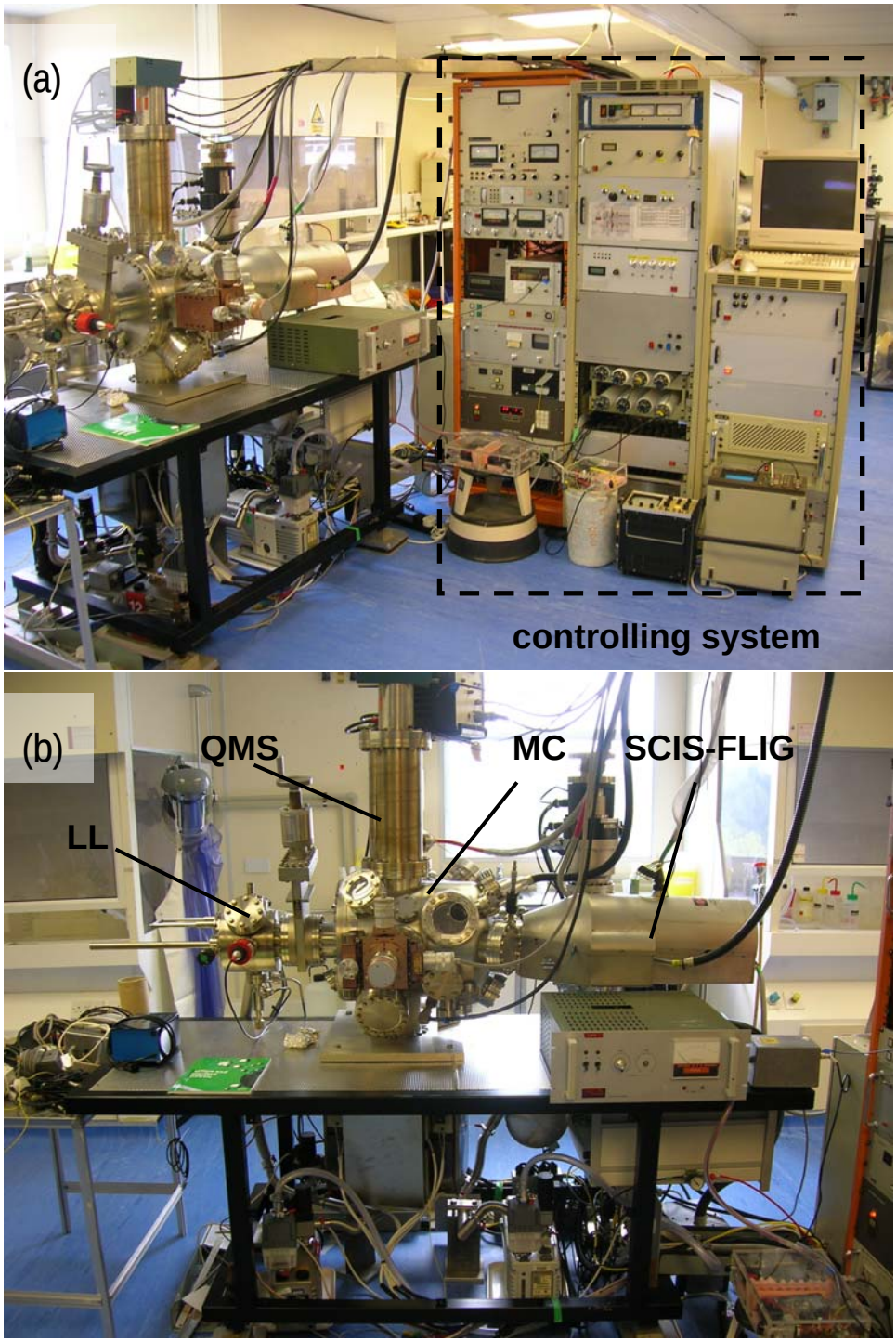

Fig. 3.1.1 The EVA 2000 SIMS instrument.

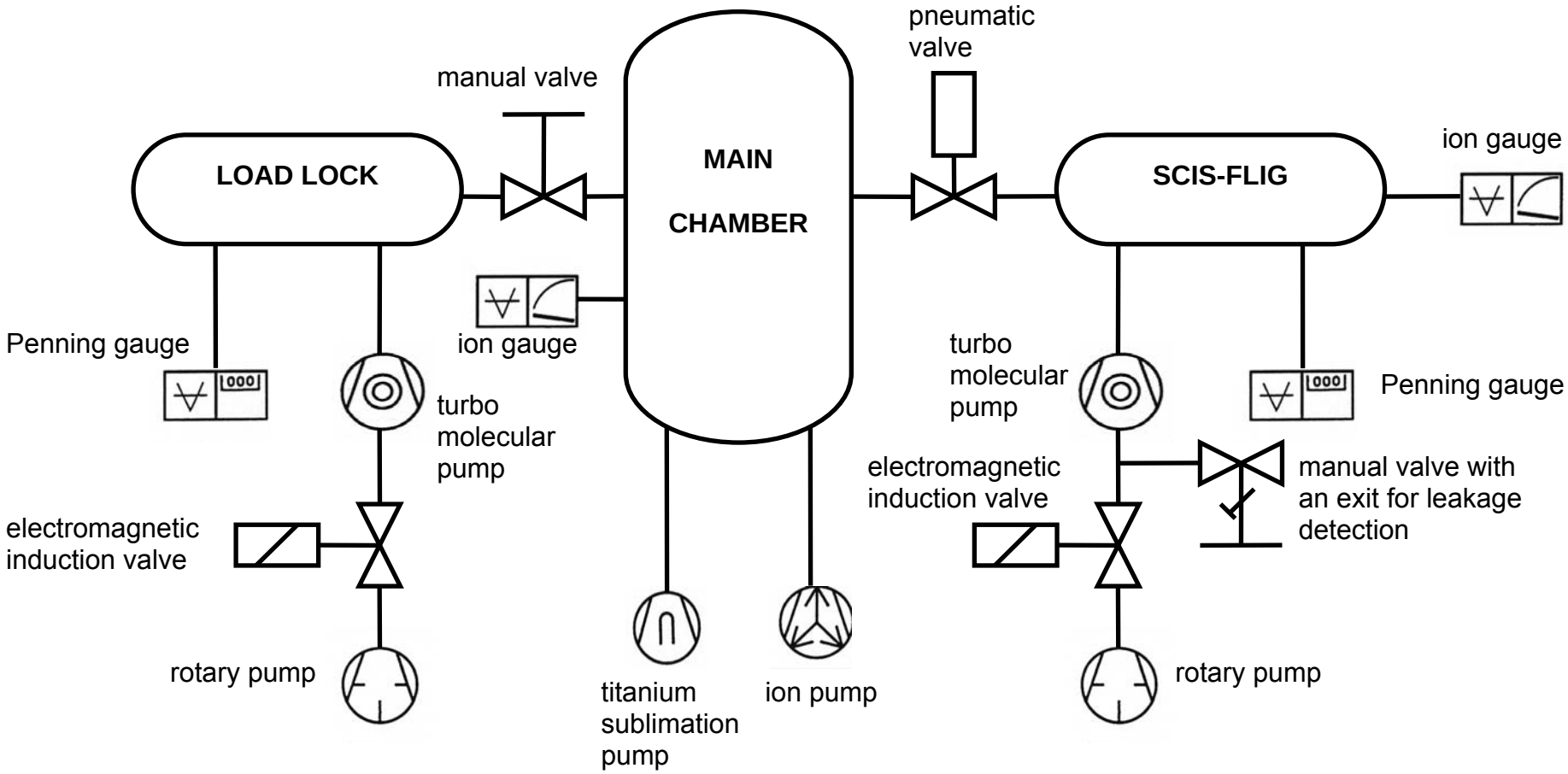

Fig. 3.1.2 Schematic diagram of the EVA 2000 vacuum system.

The sample to be analysed is attached to a sample holder (Fig. 3.1.4) by conductive silver paint or springs. The sample holder is mounted on a stage which can be controlled with four degrees of freedom, namely $\hat{x}$, $\hat{y}$, $\hat{z}$ and $\hat{\theta}$ (the relative angle between the incident beam and the sample normal), as shown in Fig. 3.1.3.

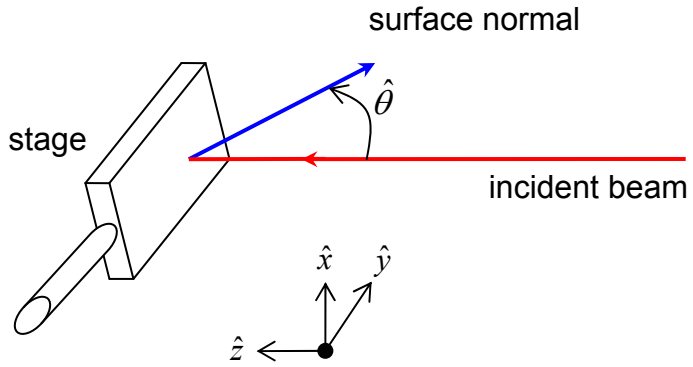

Fig. 3.1.3 Schematic diagram of the four degrees of freedom, namely $\hat{x}$, $\hat{y}$, $\hat{z}$ and $\hat{\theta}$, that the stage can be controlled, on which the sample holder (Fig. 3.1.4) is fixed.

Two sample holders are used in this project. To monitor the characteristics of the ion beam, one sample holder supports spot-welded tantalum foils to form a rectangular hole of 700 μm×700 μm through it, and the other has a circular hole of Ø100 μm (Fig. 3.1.4). The former allows the study of the beam profile, and the estimation of its size before using it for any sample analysis. The latter allows the study of the beam current density versus different energies, for example. This is combined with a Faraday cup co-designed by the author and Dr Belykh, which is mounted on the sample stage as shown in Fig. 3.1.5. A plate in front of the cup can be biased with a negative potential to suppress secondary electrons for accurate current measurement.

The electronics and power supplies on the EVA 2000 SIMS instrument are fully controlled by computer through a program designed by R. Gibbons. However, in this work almost all power supplies are controlled manually, except that for beam alignments which float on the FLIG potential (V_F) and those for the scanning system. The power supplies used in this project will be discussed in

Chapter 4 and 5. The versatile scanning system allows the user to define a crater size from as small as 1 μm×1 μm up to 11 mm×20 mm.

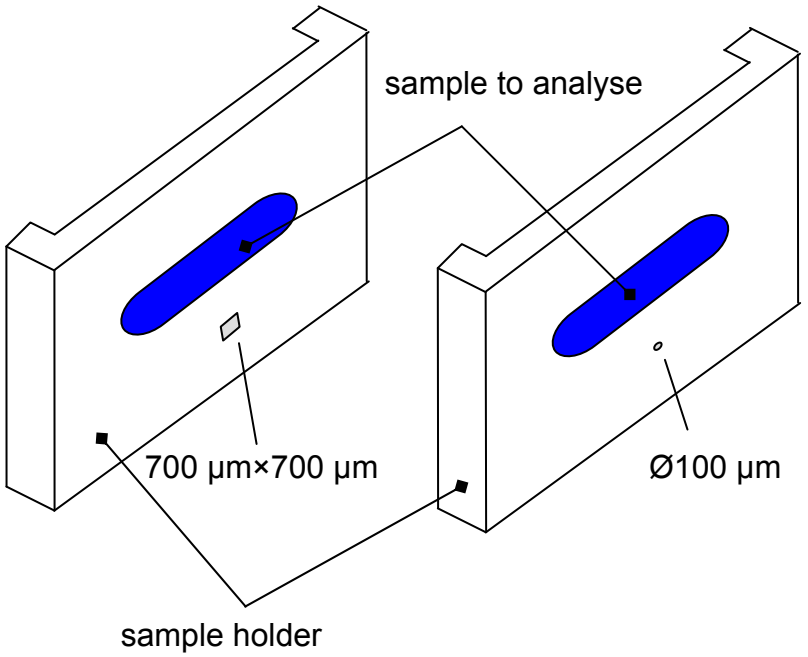

Fig. 3.1.4 Schematic diagram of two sample holders: one with a rectangular hole of 700 μm×700 μm through it, another with a circular hole of Ø100 μm.

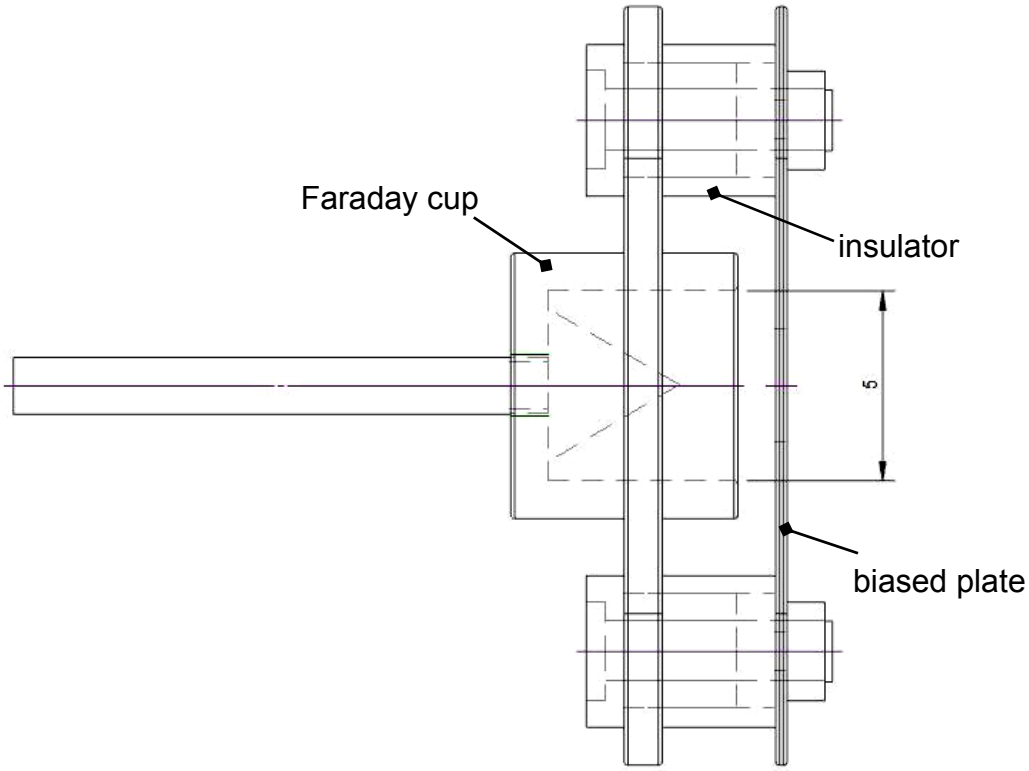

Fig. 3.1.5 The cross-sectional view of the designed Faraday cup mounted on the EVA 2000 sample stage. (dimension shown in mm)

3.2 Floating low energy ion gun (FLIG)

The floating low energy ion gun (FLIG) was designed and built in the Advanced SIMS Projects (ASP) group at Warwick. The column is intended to deliver an ultra low energy ($\leq$ 1 keV), high current density (> 25 mA cm^{-2}), O_2^+ beam onto sample, which makes routine dynamic SIMS at high depth resolution possible on near-surface and nm-scale buried features. The notion behind the invention of the FLIG is to alleviate space charge effects and ion-optical aberrations by floating the extraction and beam transport stage (compared to conventional ion guns which are normally connected to ground) and retarding the ion beam as close to the sample as possible.

Fig. 3.2.1 displays the schematic diagram of the FLIG (Dowsett M G *et al.* 1997). Although the FLIG onto which the SCIS is fitted is a modification of the type published, the principle is the same. The ion beam generated from a duoplasmatron is extracted and accelerated between the source anode, denoted as A, and the extraction electrode, Ex. The beam forms a cross-over in the extraction electrode which is then projected by lens 1 (L1) onto the beam limiting variable aperture (VA) strip. The Wien filter (WF) in between L1 and variable aperture serves to remove unwanted ion species. The Wien filter is so designed as to give an approximate balance of electrical and magnetic fields at the fringe area (Dowsett M G, 1986). In front of the Wien filter, a pair of electrostatic deflection plates is presented to correct any misalignments. After having passed variable aperture, the beam is bent of 2-3 ^{o} by a pair of electrostatic deflection plates, to get rid of any neutral components. A second pair provides beam alignment. The image formed by L1 is then projected by lens 2 (L2) onto the sample surface. The high precision scan unit immediately after L2 is designed (Dowsett M G, 1986) for maintaining a uniform ion dose across the user-defined crater area on the sample.

From L1 onwards the beam is accelerated to the floating potential in the range of 3-10 kV until L2, and all the internal electrodes in between L1 and L2 are floated. Because ions travel through the column with high energies, ion optical aberrations such as space charge effects and chromatic aberration are diminished (Smith N S, 1996).

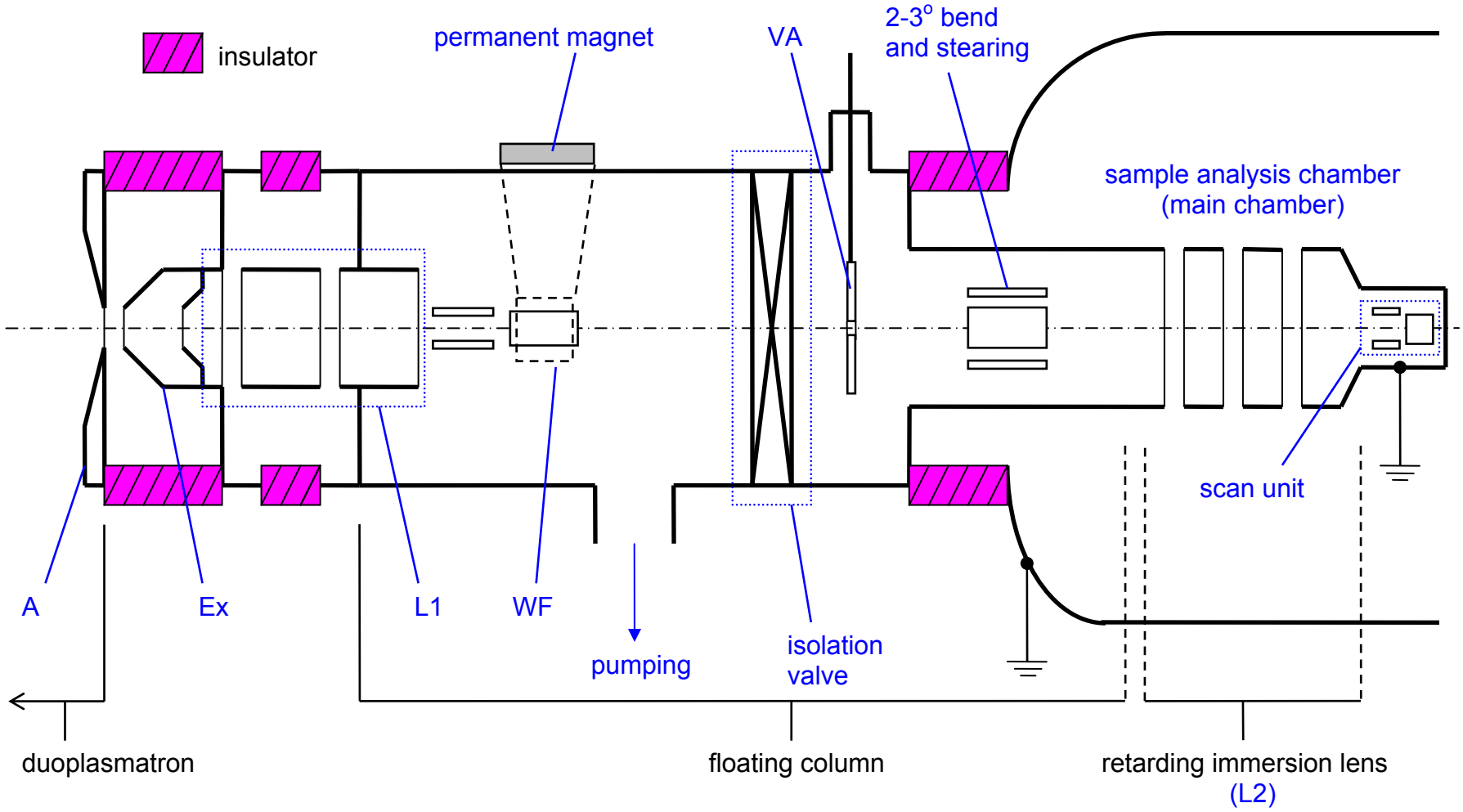

Fig. 3.2.1 Schematic diagram of the FLIG. Explanations are given in the text.

Space charge effects will be discussed in detail in Chapter 4. Principally, the higher the energy at which the ion beam is transported through an optical system, the less the time there is for ions within the beam to repel to each other. Consequently, the beam broadening due to space charge is reduced.

As defined earlier, chromatic aberration occurs when ions carrying different energies emerge into an optical system. It can be due to either the intrinsic energy distribution of an ion source or ripples on the power supply systems that provide electric potentials to the ion column. For ions emitted from the optic axis the aberration can be shown as in Fig. 3.2.2. The blue ray and black ray emerge from the same object with the same angle θ with respect to the axis, but differ in energy by ΔE. After passing through the lens, these two rays are imaged at different points along the axis. The resulting aberration disc, *the disc of least confusion*, has a radius of (Klemperer O, 1971)

$$\Delta r_c = \frac{C_c \theta' \Delta E}{2E}, \qquad \text{(Eqn. 3.2.1)}$$

where C_c is the chromatic aberration coefficient, θ' the ray angle in the image space. In the case of FLIG, $E = e(V_F - V_A)$, where V_A is the anode potential. Thus the aberration decreases when V_F increases.

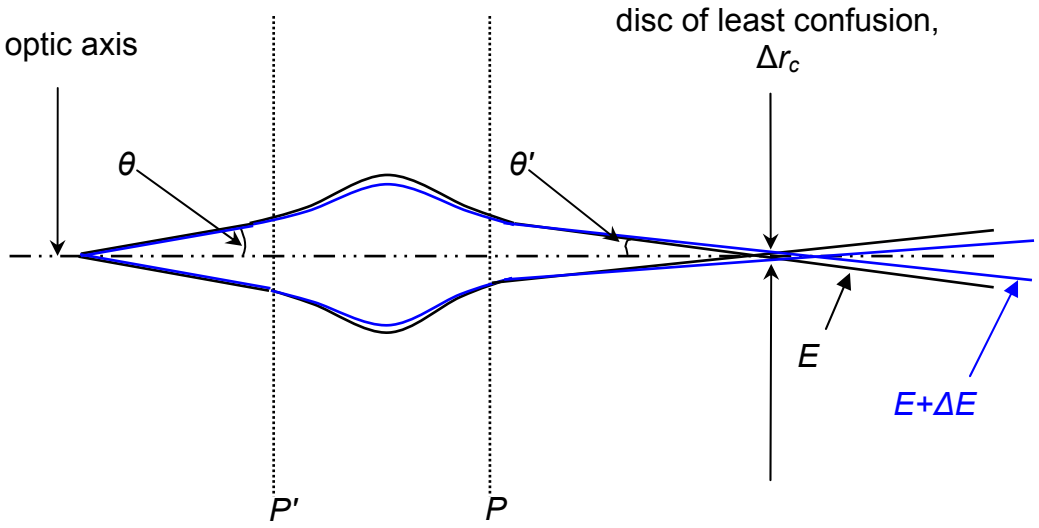

Fig. 3.2.2 Chromatic aberration and the disc of least confusion, Δr_c. P and θ are the principle plane and ray angle in the object space respectively, and P' and θ' the counterparts in the image space.

The floating potential is however limited by the geometry at L2, which is a retarding immersion lens. Given other conditions fixed, the higher ratio of V_F/V_A leads to bigger minimum probe size. This is explained by the Helmholtz equation (Longhurst R S, 1967),

$$nh\theta = n'h'\theta', \qquad \text{(Eqn. 3.2.2)}$$

where n, h and θ denote the refractive index, object radius and ray angle in the object space respectively; and n', h', θ' in the image space (Fig. 3.2.3). In electrostatic ion optics, refractive index is proportional to the square root of the local potential measured with respect to the source potential, $n = \sqrt{V}$. Thus the magnification, $M = \frac{h'}{h}$, of the lens can be expressed as (Klemperer O, 1971)

$$M = \sqrt{R}\frac{\theta}{\theta'}, \qquad \text{(Eqn. 3.2.3)}$$

where R is the retarding ratio,

$$\sqrt{R} = \sqrt{\frac{V}{V'}} = \frac{n}{n'}. \qquad \text{(Eqn. 3.2.4)}$$

The θ's are controlled by physical apertures and working distance and usually are fixed values.

Suppose a transportation energy of 6 keV through the FLIG column and the impact energy (E_p) of 1 keV are to be desired, V_A would be -1 kV for a negative (singly charged) ion beam and V_F be 5 kV. This makes V = 6 kV and V' = 1 kV (for QMS SIMS, the sample is normally connected to ground), and thus R = 6. If however the desired impact energy is 0.5 keV and the transport energy is to be maintained, R increases to 12 ($=\frac{V}{V'} = \frac{6}{0.5}$). As a consequence, the magnification is $\sqrt{2}$ times large. On the other hand, if the same retarding ratio is to be kept, in order to keep the magnification, V would be 3 kV and V_F be 2.5 kV. This leads to the reduction of the transportation energy to 3 keV, and thus makes space charge effects and chromatic aberrations more prevalent.

The use of cluster ions could be a solution for this dilemma. The retarding ratio can be kept as low as the case of E_p = 1 keV or even higher, whilst each constituent atom in a cluster ion carries a sub-keV energy. Fig. 3.2.4 shows the upper column of the FLIG and the SCIS fitted together.

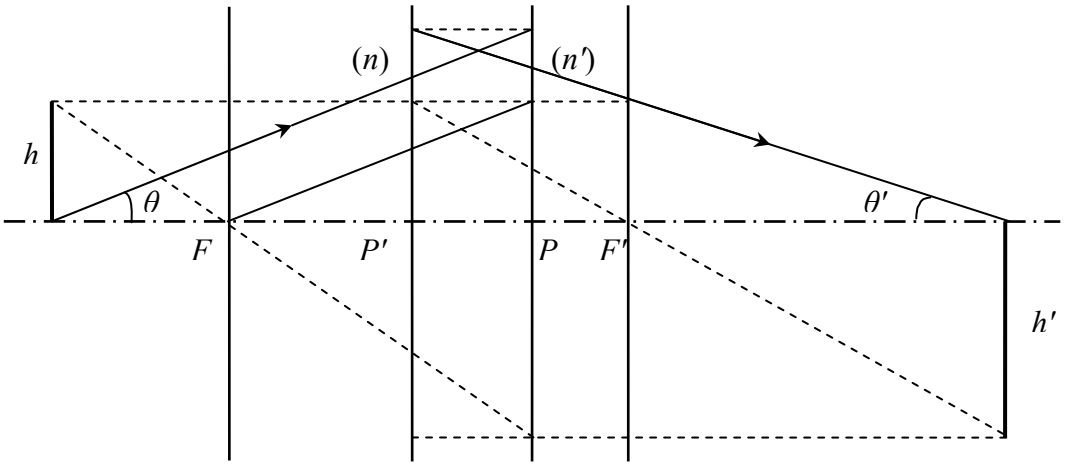

Fig. 3.2.3 Geometrical optics showing lateral magnification. P and F are the principal and focal planes in the object space, respectively, with a refractive index n; P', F' and n' are the counterparts in the image space.

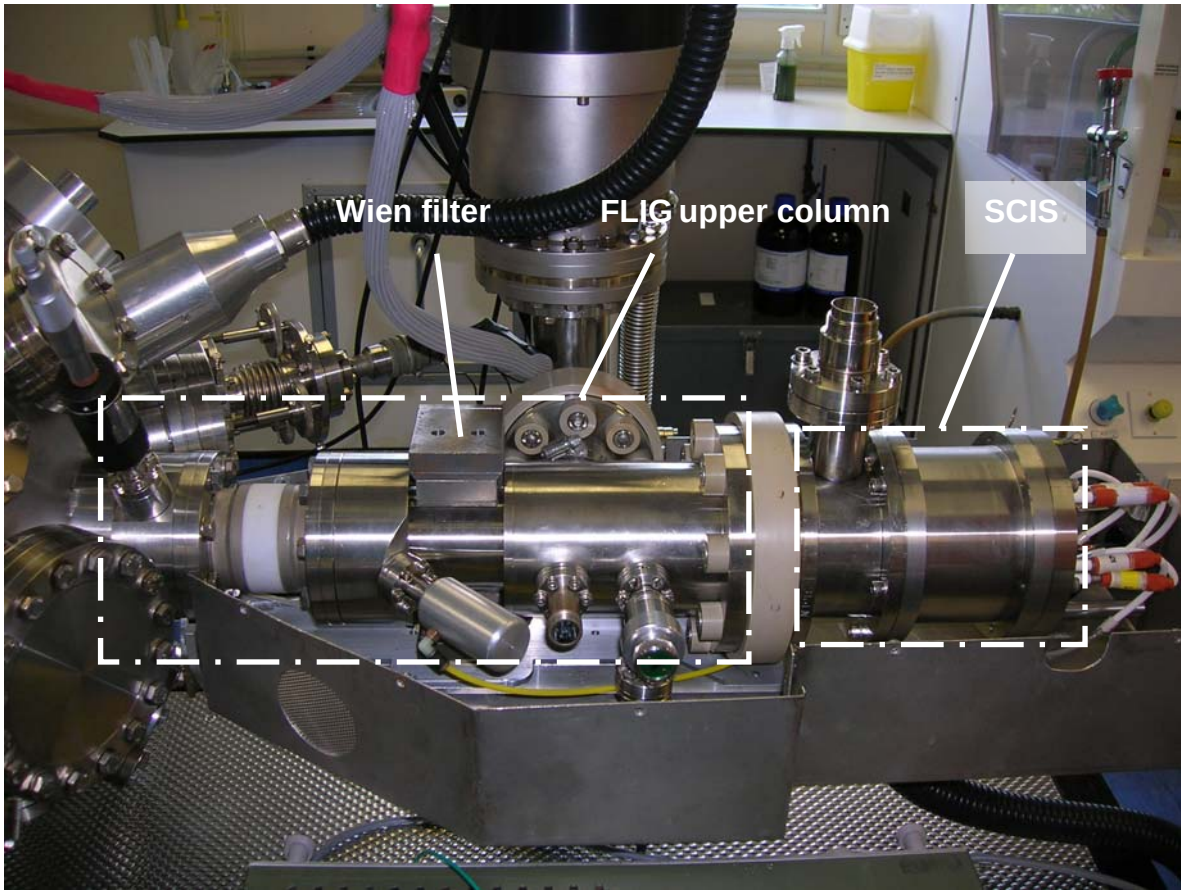

Fig. 3.2.4 The FLIG (only upper column) fitted with the SCIS on EVA 2000.

3.3 The sputter cluster ion source (SCIS)

The organisation and the operational principles of the sputter cluster ion source studied in this work are discussed in this section.

The SCIS was designed based on a prototype source which was developed at the Arifov Institute, Uzbekistan (Belykh S F *et al.*, 1992). The SCIS, prior to its transfer to Warwick for its combination with the FLIG column, was originally designed for fitting to a CAMECA IMS 4f SIMS instrument in Antwerp University, Belgium (Belykh S F, 1997). A brief history of the source development and the previous study is given, as the basis of the development of the source on the FLIG.

3.3.1 The set-up

The $Au_n^{\pm}$ cluster ion source is based on the sputtering of a gold target by Cs^+ ion bombardment. It consists of a surface ionisation Cs^+ source, a sputter target in the form of a cone and electrodes for directing trajectories of Cs^+, $Au_n^{\pm}$ cluster ions as well as controlling the emission of undesirable secondary electrons. The source is designed in a similar geometric configuration to Middleton's (Middleton R, 1977), in which the bombarding Cs^+ ions and the sputtered cluster ions are aligned on the same optic axis.

The source is illustrated in Fig. 3.3.1, and the list of numbers is given in Table 3.3.1. Note that there is another filament for the CsCl reservoir. An orthographic projection of the source is drawn from the program Alibre Design® and shown in Fig. 3.3.2.

The housing of the source is divided into two parts: one accommodates the Cs^+ ion emission system ((1)-(4) in Fig. 3.3.1), and the other covers the sputter cone and the lens set ((5)-(9)). This separate housing design has the advantage of allowing the user to refill the CsCl reservoir or replace the sputter cone leaving the other part intact. The latter housing was re-designed in this work (as shown in Fig. 3.3.2) to fit the source mechanically and ion-optically to the FLIG column, which will be detailed in Chapter 4. The two houses are sealed to each other and to the FLIG column by Viton® O-ring, and all electrical feedthroughs to connect

Table 3.3.1 The list of numbers corresponding to Fig. 3.3.1

(1)	the caesium chloride (CsCl) reservoir	(6)	the sputter cone
(2)	the Cs^+ ioniser	(7)	the cone base
(3)	the ioniser filament	(8)	the 1st $Au_n^{\pm}$ cluster ion extractor
(4)	the Cs^+ ion extractor,	(9)	the 2nd $Au_n^{\pm}$ cluster ion extractor
(5)	the shield		

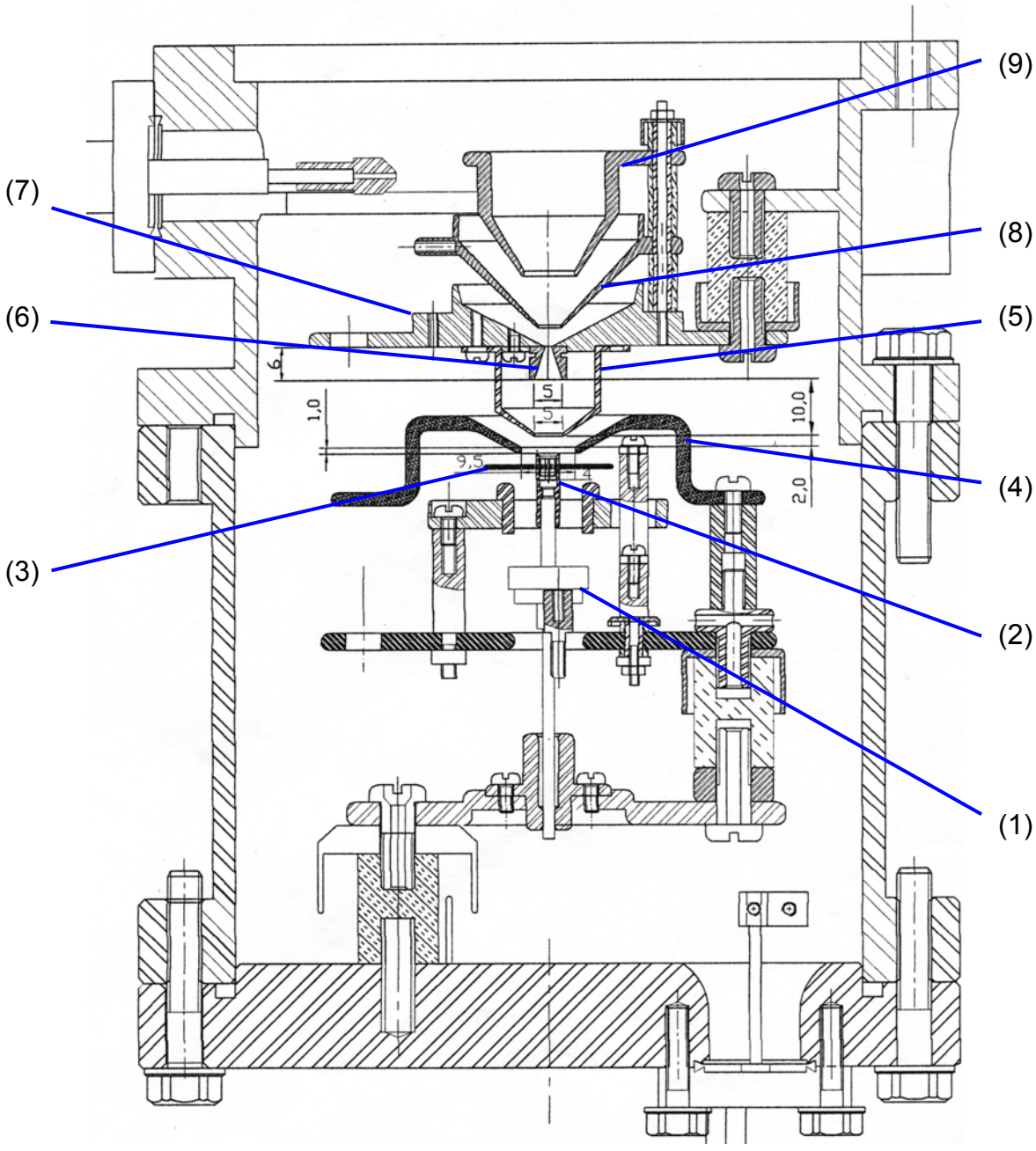

Fig. 3.3.1 The SCIS assembly as designed to fit onto a CAMECA IMS 4f SIMS instrument in the University of Antwerp, Belgium.

to the source are sealed by copper gaskets so as to maintain high vacuum in the column (< 10^{-7} mbar).

All electrodes, fastenings as well as housing components are made of stainless steel 304, except the electrical connection for the filaments which are made of copper and BeCu for delivering the required current (up to 5 A through each filament), and the filament washers which are made of molybdenum for high temperature performance (~2500 ^{o}C) (Belykh S F, 2007). The materials used for the Cs gun are described in next section. High density recrystallised alumina is used for electrical insulation in the source.

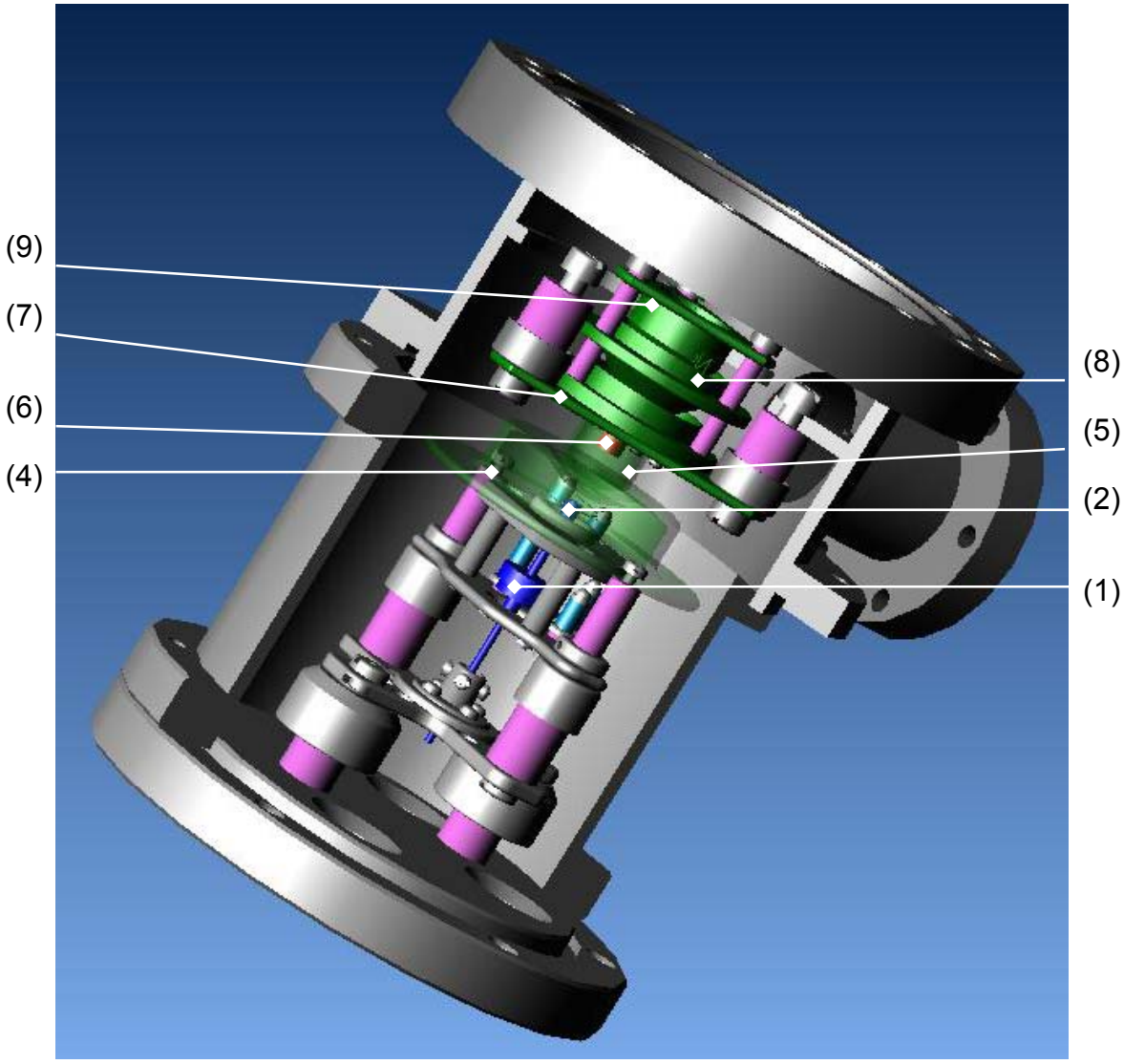

Fig. 3.3.2 Orthographic cut-away projection of the SCIS assembly, after the modifications had been made for its fitting with the FLIG. The numbers are referred to Table 3.3.1.

3.3.1.1 The Cs^+ emission system

The Cs^+ emission system is based on a surface ionisation ion source (Vályi L, 1977). The Cs emitting element is inserted into the ioniser tube of a CAMECA microbeam source (Slodzian G *et al.*, 1991), replacing the foil emitter. It is similar to the design of Middleton and Adams (Middleton R and Adams C T, 1974). It consists of a CsCl (Alfa Aesar, 99.999%) revervoir, an ioniser holder and an ioniser tube (Fig. 3.3.3), the first two of which are made of tantalum and the latter of tungsten.

Tungsten wires of diameter 20 μm and length of 3 mm are pressed into the ioniser tube (tantalum). A thicker tungsten rod of diameter 1 mm is inserted into the centre of the tube intended to prevent Cs^+ / Cs^0 particles passing through the cone aperture, which will contaminate the insulators between the lens electrodes and may exacerbate space charge effects when the source is run in positive mode (emitting positive cluster ions). The ioniser tube is kept in place by the ioniser holder.

The reservoir encloses ~0.1 g CsCl and is sealed by an Au gasket because copper gaskets are found to corrode seriously, leading to loss of CsCl from the reservoir (Belykh S F, 2006). The ioniser and the reservoir are heated by electron bombardment by two separate tungsten filaments (Advent Research Materials Ltd., Ø 0.2 mm, purity 99.95 %, annealed, ref. No. W558009). The maximum filament current is 5 A and the maximum emission current is 4 mA per filament.

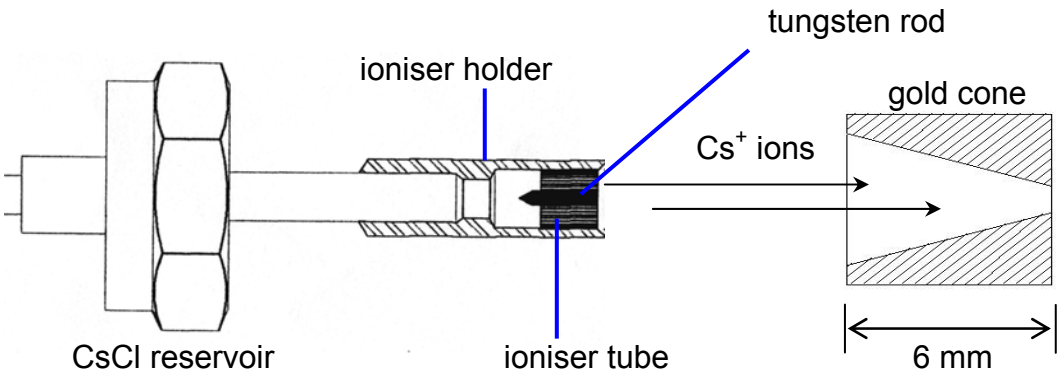

Fig. 3.3.3 Schematic diagram of the Cs emission system.

The Cs^+ gun assembly of the SCIS as built in Antwerp is shown in Fig. 3.3.4 below.

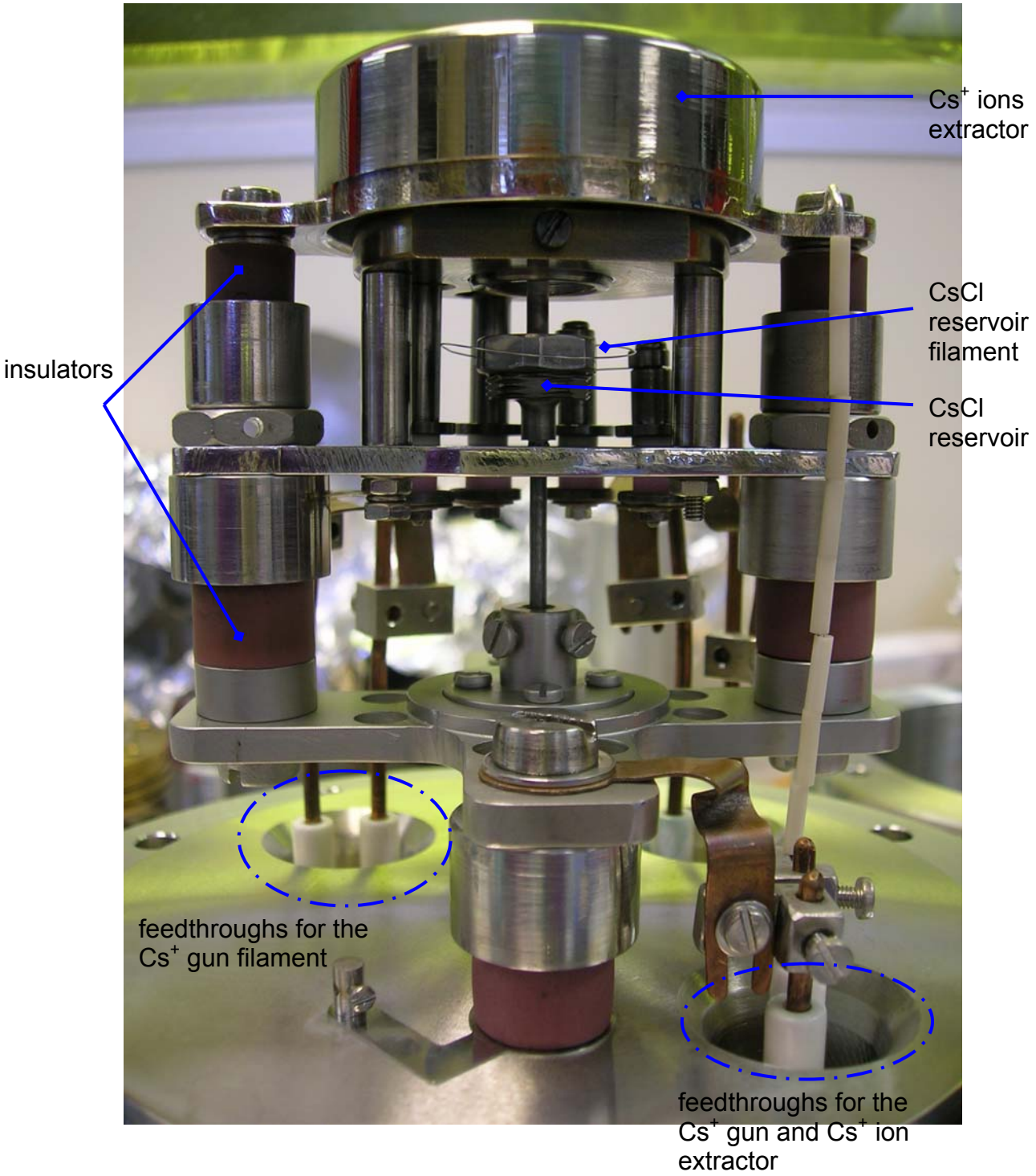

Fig. 3.3.4 The Cs^+ gun assembly as built in Antwerp University and subsequently modified at Warwick. The numbers are referred to Table 3.3.1.

3.3.1.2 The sputter cone

The first sputter cones were machined from silicon or copper in the shape of a Ø 6.5 × 6 mm long rod with a conical hole drilled through its centre (Fig. 3.3.5). They were made for use at Antwerp, where the mass filter of the primary column cannot separate heavier ions such as $Au_n^{\pm}$. The end facing of the Cs^+ ioniser is known as the *cone entrance* (Ø 5 mm), and the other (facing the lens set) as the *cone aperture* (Ø 1 mm). In this work a cone was machined from stainless steel 304, and then an Au foil 0.5 mm thick (Goodfellow Ltd., ref. No. 095-204-88, 99.95% pure) was pressed onto the cone surface that the overall geometry is kept unchanged. It is very difficult to machine a cone from pure gold without disfiguring the shape.

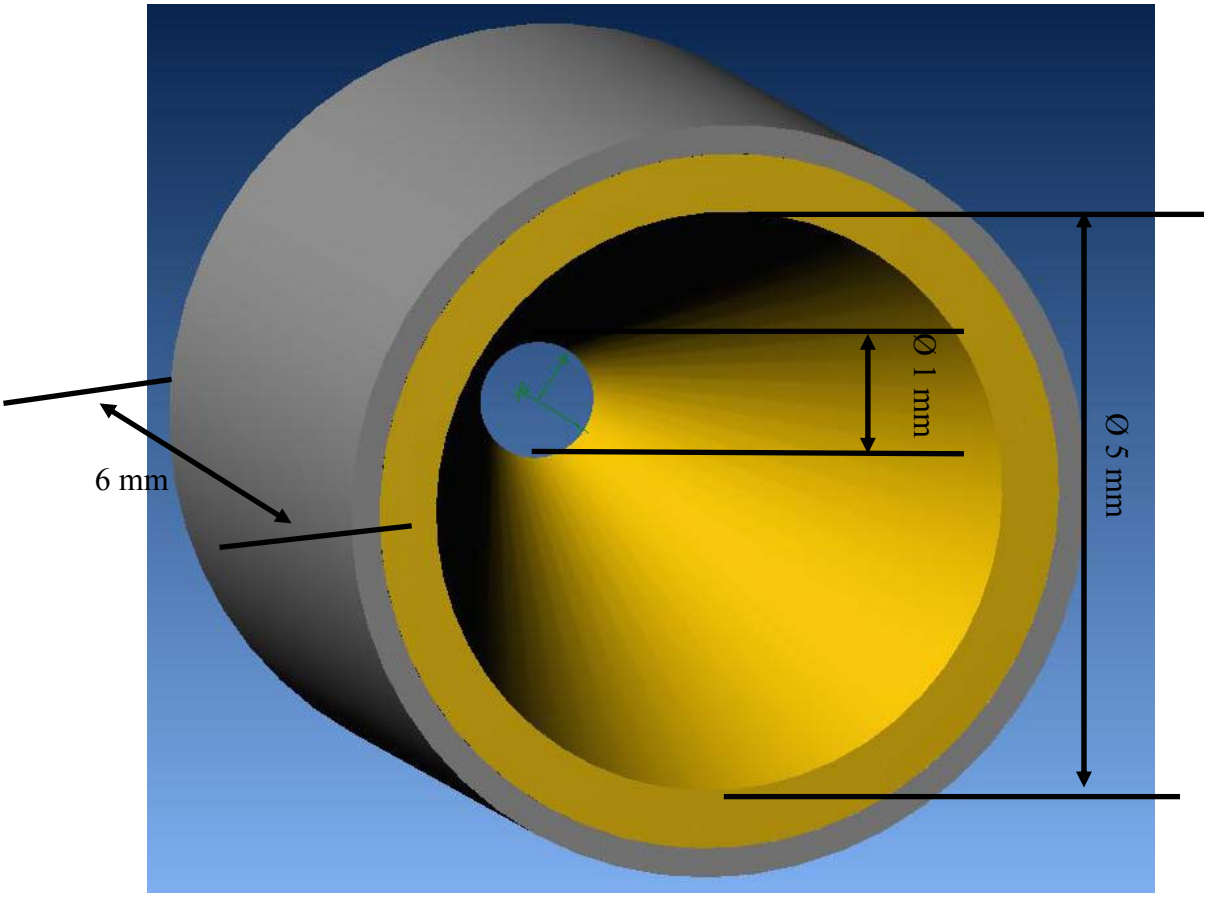

Fig. 3.3.5 Orthographic projection of the sputter cone.

3.3.2 The principles of operation

The CsCl evaporates on heating and is transported to the ioniser. It dissociates upon contact with the hot tungsten wire (the temperature cannot be measured with the current experimental set-up, however in the prototype source it was found to be 1100 ^{o}C (Belykh S F, 2007)). Surface-ionised Cs^+ ions are extracted, accelerated and focussed by the electric field due to the Cs^+ ioniser, Cs^+ extractor, the shield and the cone, bombarding the cone surface (see simulations in Chapter 4). The impact energy (E_{Cs^+}) is normally 4-5 keV, at which the sputtered cluster yield is at its highest (Belykh S F *et al.*, 1992). The total Cs^+ current (I_{Cs^+}) is controlled by the temperature and can normally exceed 200 μA. The shield was designed to direct $Au_n^{\pm}$ ions to exit the cone aperture as well as to prevent $Au_n^{\pm}$ ions bombarding the Cs^+ ioniser.

The gold foil is sputtered by Cs^+ ions and the secondary $Au_n^{\pm}$ cluster ions are extracted from the cone aperture by the electric field due to the shield and the 1st extractor ((5) and (8) in Fig. 3.3.1). After having passed through the FLIG column with the variable aperture at Ø 800 μm, the 1 keV Au_1^- current is usually measured to be approximately 10^{-4} of the Cs^+ current on the sample position, and the ratio of Au_1^-:Au_2^-:Au_3^- approximately 13:1.2:1, under the conditions: E_{Cs^+} = 5 kV (±1 %), I_{Cs^+} = 1-50 μA, with the FLIG chamber pressure < 5×10^{-7} mbar. This will be described in more detail in Chapter 5.

3.3.3 History of the source development and previous study

Under a NATO scientific project (Belykh S F *et al.*, 1997), the SCIS was designed and built to fit onto the CAMECA IMS 4f primary column. It is based on the prototype source developed and built by Belykh *et al* (Belykh S F *et al.*, 1992). The main difference is that the optic axes and consequently the trajectories of the bombarding Cs^+ ions and the sputtered $Au_n^{\pm}$ ions of the prototype are orthogonal to each other, whilst in the SCIS both ions travel on the

same axis. The performance and previous studies of nonlinear ion yield due to cluster ion bombardment are described here.

3.3.3.1 The prototype source

Under the conditions typically used: I_{Cs^+} = 30 μA, E_{Cs^+} = 2.4 keV, T_{target} = 293 K, background pressure = 10^{-8} Torr, the source generated an Au_1^- current ~ 10^{-6} A and the intensity ratio of Au_1^-:Au_2^-:Au_3^- = 100 : 3 : 1 (Belykh S F *et al.*, 1992). The increase of the partial oxygen pressure (10^{-8} to 10^{-6} Torr) in the gold target environment was reported to decrease the negative ion yields by more than a half, but the effect is opposite with the positive species. The maxima of Au_n^- (n = 1-3) yields were found when E_{Cs^+} = 5 keV. Au_2^- and Au_3^- were observed to increase more rapidly than Au_1^- when E_{Cs^+} changed from 2.5 to 5 keV.

The prototype source was employed for the study of nonlinear effects due to cluster bombardment on a SIMS instrument based on the commercial MI-1201 mass spectrometer produced in SELMI (Sumy, Ukraine) (Belykh S F *et al.*, 1997, 2000a, 2000b, 2001). Targets made of gold or aluminium (Al) were sputtered by Cs^+ ions to generate primary ion beams with E_0 = 4-18 keV (E_0 defined in section 2.2.1). The stability of the Au_n^- (n=1-3) ion current was established to be 1% by a Faraday cup on the sample (for an unspecified time), and the beam spot is Ø ~1 mm. The current density of Au_1^- is some 10^{-6} A cm^{-2}, and Au_2^- and Au_3^- 10^{-7} A cm^{-2}. (The ratio of Au_1^-:Au_2^-:Au_3^- in this case is about 10 : 1 : 1 and different from that reported earlier, 100 : 3 : 1. The author did not explain this discrepancy.) Samples of tantalum, niobium, silicon and silicon uniformly doped with carbon were studied with the cluster ion beam impacting 45 ^{o} to the sample normal. Other than the general observation of nonlinear enhancement of secondary ion yield due to cluster ion bombardment, it was also reported that:

(1) the secondary ion yields increased with the overall primary impact energy;
(2) the nonlinear factor (Eqn. 2.2.1) increased with increasing nuclearity (section 2.2.1) of the primary ion as well as of the secondary ion, which was as high as 2000 for Si_7^+;
(3) cluster ion bombardment led to lower yields of doubly-charged Si^{2+} ions;

(4) for the application of analysing C in Si samples, it was suggested that the detection of carbon-containing cluster ions Si_mC^+ instead of C^+ gave higher sensitivity;

(5) when the Si sample was bombarded by Al_n^- (n = 1-2) ions, with E_0 = 9 keV, the nonlinear effect did not increase with the size of the secondary ions (Si_m^+), and larger clusters Si_m^+ (m = 5-17) were not observed, contrary to the situation for Au_n^-. On the other hand, when E_0 decreased to 6 keV, the nonlinear effect did increase with the secondary ion Si_m^+ size. This was explained by the fact that the ion yield enhancement depends not only on the incident energy E_0, but also on the penetration depth of the primary ion which determines the energy density at the top surface layers where sputtering and ion emission take place (Belykh S F *et al.*, 2001).

3.3.3.2 The SCIS

The first sputter cone was made of silicon. It was bombarded by 7.5 keV Cs^+ ions at a current of 60 μA and generated Si_n^- ions with currents of 5.6, 2.8, 0.48, 0.085, 0.028 and 0.0063 nA for Si_1^-, Si_2^-, Si_3^-, Si_4^-, Si_5^- and Si_6^- respectively, as measured on the Faraday cup (Belykh S F *et al.*, 2001). The Si_n^- ions were then used to bombard a Si sample with E_0 = 12 keV (spot size Ø 60 μm). The secondary ion yields were observed to increase with the primary ion size (Si_n^-, n=1-3) by a factor of 5-12 for impurity and molecular ions, and by a factor of 1.5-3 for secondary Si_m^+ (m = 1-5) ions. This difference in ion yield enhancement was explained by different binding energies. Moreover, the use of Si_n^- ions (E_0 = 12 keV) has a similar effect to Al_n^- ions (E_0 = 9 keV) in that they do not lead to effective emission of larger clusters, and this was attributed to the light mass of the constituent atoms of the ions and deep penetration of the ions into the samples. From the other studied sample of indium gallium phosphide (InGaP) (Belykh S F *et al.*, 2003a) it was observed that the nonlinear effect is more pronounced than the silicon samples, for all types of secondary ions. This was explained by a higher energy density being deposited into the subsurface layers on the heavy target due to the back-scattering effect, which in turn enhanced the sputtering process.

Chapter 4 Simulations and Retrofitting of the SCIS to the FLIG

Simulations were performed in order to understand the characteristics of the SCIS, including ion trajectories and operational details. This was to serve as the basis for retrofitting the source onto the EVA 2000 FLIG, and proved to be quite useful for understanding the practical performance of the combination of SCIS-FLIG.

The ion-optical aberration, *space charge effect*, was taken into consideration in the simulation: for a beam of charged particles carrying high current density at low energy, the fields created within the beam by ions themselves will dominate the transport property (Klemperer O, 1971). It was reported that a current of ~10 μA (including e^-, $Cu_n^{\pm}$ and Cs^+) was measured behind a copper cone aperture on the CAMECA IMS 4f instrument in the University of Antwerp (Belykh S F *et al.*, 2001), and the total Cu_n^- (n = 1-3) current was found to be ~ 4 nA after the magnet sector of the primary ion column (Belykh S F, 2004). This means a fraction of 0.04 % of Cu_n^- ions was produced, and the majority of the rest should be Cs^+ ion induced secondary electrons. With a cone made of gold, it was assumed there would be a higher fraction of secondary electrons due to the higher electron affinity of gold (Au: 2.309 eV; Cu: 1.235 eV; Lide David R, 2007). Thus, it is expected when the SCIS is mounted on the EVA 2000 FLIG, the beam would suffer strongly from space charge effects in the space after the extraction and before the Wien filter, where the abundant electron current is present.

A brief introduction of the analysis of space charge effects in field-free space by El-Kareh and El-Kareh (1970) is presented in section 4.1. These effects in field-free space and in SCIS-FLIG were simulated and displayed respectively in sections 4.2.3 and 4.2.4. The simulation in SCIS-FLIG, however, can only be seen as an approximation, because the program used, SIMION® (version 7.0, Dahl D A, 2000), cannot simulate space charge properly, particularly in the ion extraction region. SIMION can only simulate space charge with beams that are mono-species, mono-energetic and cylindrically

symmetric. In reality, the charged particles generated by the SCIS include Cs^+, Au_n^+, Au_n^-, e^- and probably also Au_nCs^-. They are neither mono-energetic, nor cylindrically symmetric.

4.1 Space charge

There are two kinds of interactions between charged particles: one is the coulomb repulsion, another is the magnetic attraction for particles travelling in the same direction. The latter effect is negligible when the velocity of the beam is small with respect to that of light, i.e. non-relativistic. Consider this simple case – a beam consisting of two rays moving with the same velocity v in the same direction. The net force, F, imposed on a unit length of each ray would be

$$F = F_e - F_m = \frac{q^2 n^2}{2\pi\varepsilon_0}\left(1 - \frac{v^2}{c^2}\right)\frac{1}{r}, \qquad \text{(Eqn. 4.1.1)}$$

where F_e is the electrostatic repulsive force and F_m the magnetic attractive force, q is the charge on an electron, n the number of charged particles per unit length, ε_0 the permittivity in free space, c the velocity of light and r the distance between these two rays. In the case of SCIS-FLIG, if the cone potential is -1 kV and floating potential 5 kV, Au_3^- ions would be transported with an energy of 6 keV. Then, v can be obtained to be about 7.7×10^4 ms^{-1} which is really inconsiderable compared to the speed of light.

The minimum space charge limited beam waist and position due to coulomb repulsion have been analysed by El-Kareh and El-Kareh (1970). The analysis is based on the assumptions that the beam is mono-energetic, homogeneous and cylindrically symmetric, and that the beam is present in an external-field free space after leaving an aberration-free electrostatic focussing field. The potential difference between the centre and boundary of the beam resulting from space charge should also be very small compared with the beam voltage. Although realistically these assumptions do not hold, the approximation

provides information about how the beam would behave and thus what countermeasures may be made.

Fig. 4.1.1 represents the cross section of a homogeneous beam of circular symmetry about the axis $\hat{z}$. The beam has a radius of r_i when leaving the focussing electrode, and should be focussed at a distance d_i from the electrode end if space charge does not exist. The minimum beam waist obtainable, r_m, is derived as

$$r_m = r_i \exp\left[-\left(\frac{vm\varepsilon\pi}{Iq}\right)\dot{r}_i^{\,2}\right], \qquad \text{(Eqn. 4.1.2)}$$

and

$$\dot{r}_i = \left.\frac{dr}{dt}\right|_{r=r_i}, \qquad \text{(Eqn. 4.1.3)}$$

where v is the beam velocity along the axis, m the mass of the ion, ε the permittivity, I the beam current, $\dot{r}_i$ the initial radial component of beam velocity inwards (El-Kareh and El-Kareh, 1970). Clearly, the minimum beam waist can be reduced by increasing v and decreasing I. The position at which r_m occurs is found to be

$$d_m = 2v\xi^{1/2} r_i \exp\left(-\xi\dot{r}_i^{\,2}\right)\int_0^{\xi^{1/2}\dot{r}_i} e^{x^2}\,dx, \qquad \text{(Eqn. 4.1.4)}$$

where

$$\xi = \frac{vm\varepsilon\pi}{Iq}. \qquad \text{(Eqn. 4.1.5)}$$

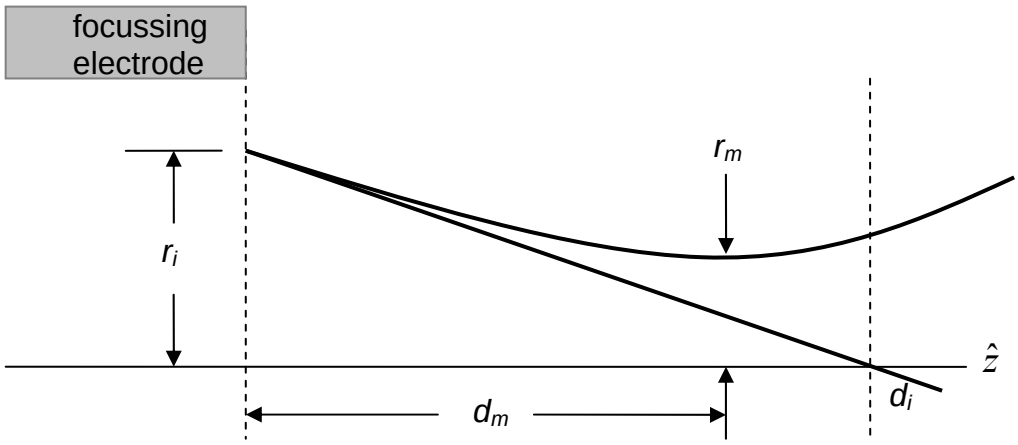

Fig. 4.1.1 The view of the cross section of a circular beam symmetrical about the $\hat{z}$ - axis. The beam has a radius of r_i when leaving the focussing electrode, and should be focussed at a distance d_i if space charge does not exist. Due to space charge the beam reaches its minimum beam waist (radius), r_m, at a distance of d_m from the electrode.

4.2 Simulation of ion emission and space charge

4.2.1 Experimental

The SCIS model was constructed full size in the SIMION program (Fig. 4.2.3 and Fig. 4.2.4). At the very left is the Cs^+ thermal ioniser, and to the right are in turn: the Cs^+ ion extractor, the shield, the gold (Au) cone and the two Au_n^- ion extractors. They correspond to (2), (4), (5), (6), (8) and (9) in Fig. 3.3.1, respectively. (Note in the simulation the shield was modelled into two pieces with the intention of gaining the independent control of Cs^+ and Au_n^- ion trajectories, because the Cs^+ extractor and the shield of the original design influence ion trajectories, as explained in section 4.2.2.)

The initial energy of the simulated Au_3^- clusters was assumed to be 1-5 eV. This assumption was based on the secondary ion energy distribution studies of Au_1^- sputtering Ta_n^+ ($^{197}Au_1^- \rightarrow {}^{181}Ta_n^+$) (Veryovkin I V *et al.*, 2004), $^{197}Au_1^- \rightarrow {}^{115}In_n^+$ (Samartsev A V *et al.*, 2006) and $^{131}Xe^+ \rightarrow {}^{28}Si_n^+$ (Wittmaack K, 1979), from which the most probable energy of the sputtered ions is found to be 1-10 eV and where cluster ions have smaller energy spread than atomic ones. The combination of $^{133}Cs^+ \rightarrow {}^{197}Au_n^-$ was not found in literature. The emission angles were chosen 10 ^{o} to 80 ^{o} to the surface normal, similar to the cosine angular distribution described by Sigmund P (1977). The Au_3^- ion was arbitrarily chosen as the representative for ion trajectory of Au_n^- (as well as its positive counterpart, Au_3^+, if all electrode potentials are reversed).

The cone surface was categorised into five areas for emission simulation (Fig. 4.2.1 (a)): the 1st was at the cone entrance position, the 2nd was 1.5 mm closer to the cone aperture and so on, and the final one was at the cone aperture position. For each area there were four emission points: two (0.55 mm apart) in the $\hat{x}\hat{y}$ plane and the other two in the $\hat{x}(-\hat{y})$ plane (Fig. 4.2.1 (b)). Each point has an emission of 192 ions defined by the program SigmaPlot® 8.0 as follows. There are 24 equispaced rays on each of the 8 ray cones, with the 1st ray cone 10^o apart from the surface normal, and 2nd 20^o, and so on (Fig. 4.2.1 (c)).

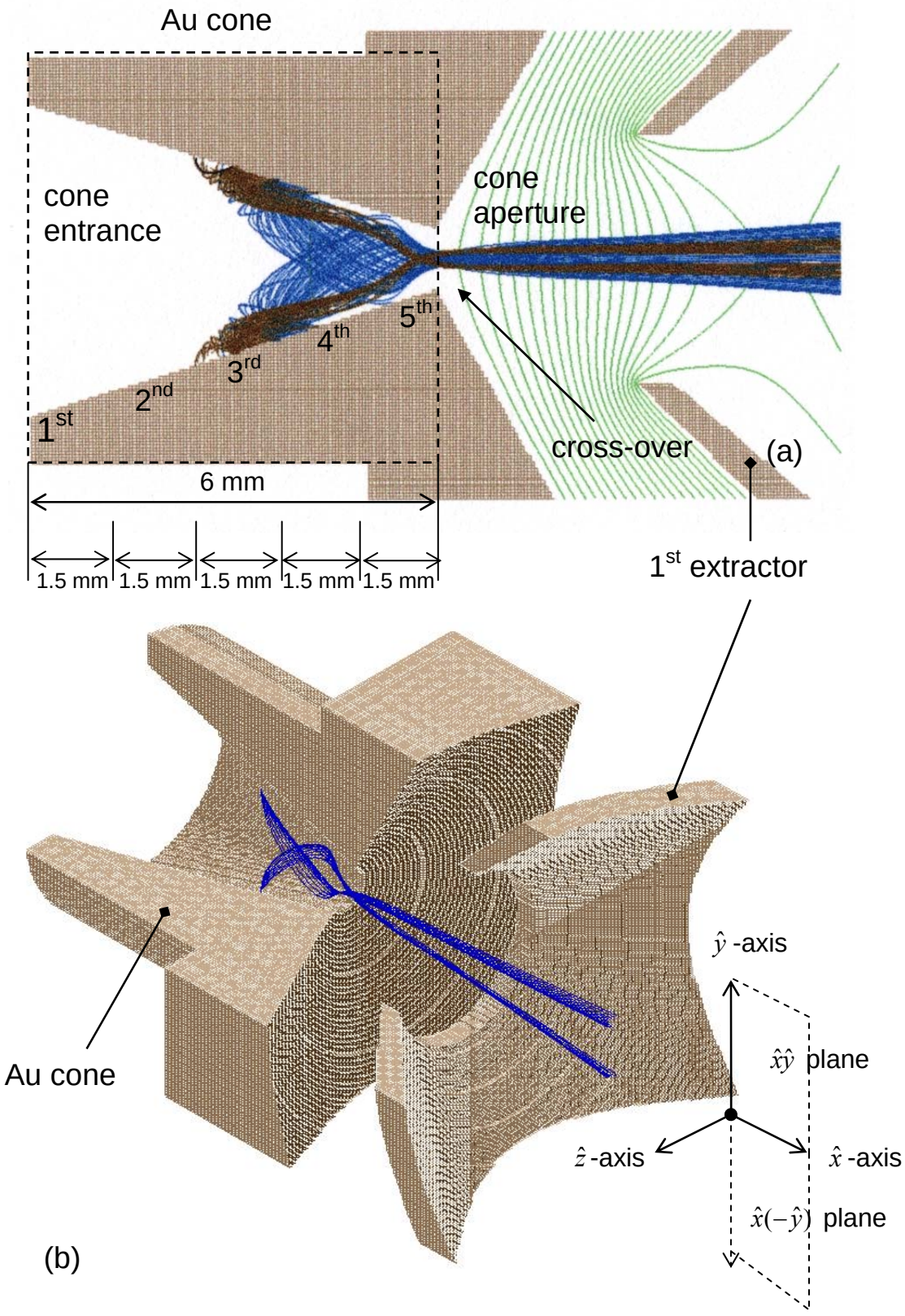

Fig. 4.2.1 (a) the Au cone, the cone entrance, the cone aperture and the five emission areas. (b) The orthographic projection: ions are emitted from the cone surface in the $\hat{x}\hat{y}$ and $\hat{x}(-\hat{y})$ planes.

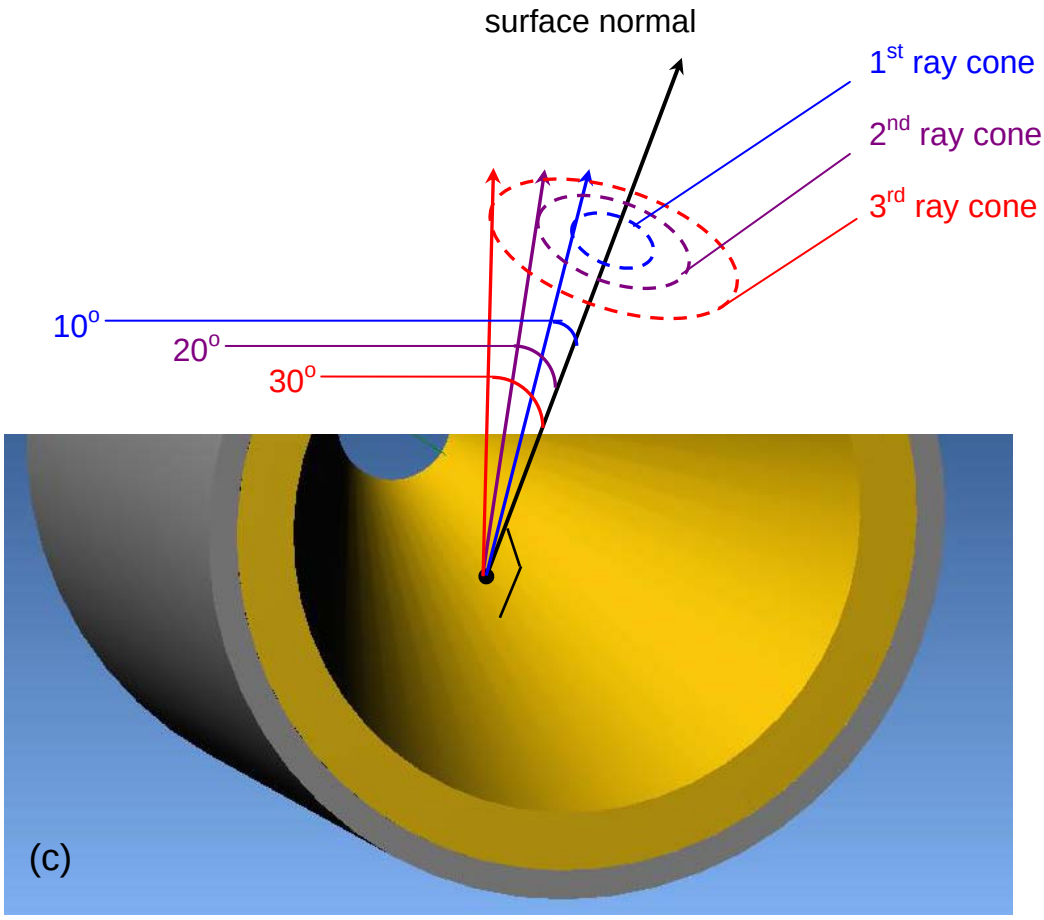

Fig. 4.2.1 (c) The definition of Au_n^- ions. There are 8 ray cones, and each ray cone has 24 equispaced rays, making a total of 192 rays from an emission point.

In summary, each of the five areas was simulated by 768 rays (= 4 points × 192 rays/point). For each area, a set of electrode potentials was sought for optimal emission – maximum ion transmission through the cone aperture in addition to minimum cross-over immediately afterwards.

Two sets of Cs^+ ions were defined. The first has five emission points from the tungsten wires (each 275 μm apart) and one from the tungsten rod (section 3.3.1.1). For each emission point, there are 9 ray cones with initial angles 0^o-80^o to the emitter surface. Each ray cone has 24 equispaced rays. Thus, in total there are 216 (=9×24) rays per emission point. The second set has only 20 equispaced ions across the emitter surface, with the initial angle normal to the emitter surface. The initial energy of Cs^+ ions was set to 0.1 eV assuming a Maxwellian velocity distribution as the temperature on ioniser is about 1100 ^oC (Vályi L, 1977).

To verify the fidelity of SIMION space charge simulation, a simple problem was set up. A beam was designed to pass through a field-free space in SIMION, and the results were compared to the analytical values calculated using a script for SigmaPlot written by Dowsett, using the approach derived by El-Kareh and El-Kareh (1970). The diameter of the beam defined is 2 mm as shown in Fig. 4.2.2. Except for the centre which has only one ray, there are 8 equispaced rays on each of the 10 concentric rings. The ring radius increments by 0.1 mm. Each ray carries 1 positive charge and was given a charge weighting factor (CWF) in SIMION ensuring that the defined beam is electrically homogeneous. Without space charge the beam was set to focus at a distance of 100 mm from the emitting position, the origin. The ion mass was arbitrarily chosen to be 130 Da with an energy of 5 keV.

The parameters of the beam, such as ion mass, charge state, etc., were then changed to simulate the space charge effects that may occur in SCIS-FLIG. The beam was sourced from the cone aperture, with a total Au_3^- current of 10-100 nA (section 4.2.4). The initial angle of each ray was set to be normal to the aperture surface, and the beam diameter was Ø 1 mm instead of Ø 2 mm. The mode of *Beam Charged Repulsion* was used throughout the simulation of space charge in SIMION (Dahl D A, 2000), with which the user observes and estimates space charge effects against the beam current.

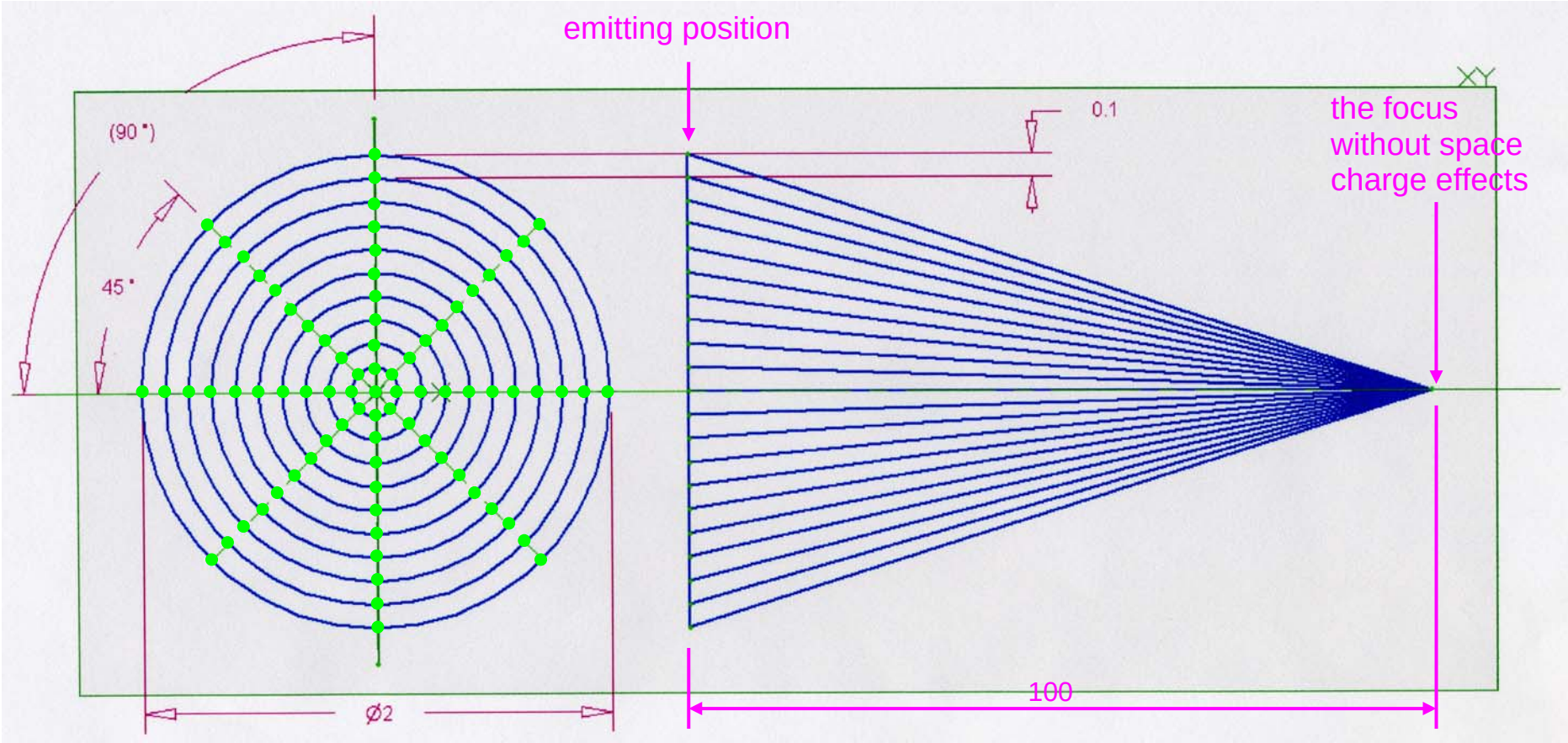

Fig. 4.2.2 Schematic diagram of the beam design for SIMION space charge effect simulations (in mm).

4.2.2 Au_n^- ion emission

The trajectories of ions emitted from the 1st and the 3rd positions were shown in Fig. 4.2.3 and Fig. 4.2.4 respectively. The potentials of the Cs^+ extractor, the shield and the Au_n^- extractors play a crucial role in directing Au_3^- ion trajectories, where the first two act to repel Au_3^- ions towards the cone aperture and the Au_n^- extractors to push them out and focus. The emission from the cone surface is very sensitive to the potentials of the Cs^+ extractor and the shields. For example, for optimal emission from the 1st and 3rd areas, the required potential of the Cs^+ extractor changes from -1.5 kV to 0 kV, and that of the shield from -3.017 kV to -3.3 kV. Ions which cannot pass through the cone aperture either hit the opposite cone surface due to an inadequate electric field above the emission area or are simply suppressed due to an excessive field. This means that, with a given set of potentials, only one area can emit ions optimally, and the cone surface would be sputtered non-uniformly. This eventually leads to a change in the cone shape, and the previous set of potentials would no longer be optimal for the emission; however, they might be then optimal for emission from other areas. Ions which hit the other side or are suppressed remaining the same surface may form a loose nanoparticle film on the surface and can be more easily sputtered than the intact surface (T*ä* rvi T T *et. al.*, 2008; Zimmermann Steffen *et. al.*, 2008).

As only a certain area can emit ions optimally with a given set of potentials, it is advisable to focus the Cs^+ ions onto that area by changing the Cs^+ extractor potential. This idea of mine and Dr Belykh's was tested, and it was found the Cs^+ trajectories did not change much with the Cs^+ extractor potential, and that they mainly fell in the region of 3rd-4th of the cone. The change of the Cs^+ extractor potential influences more the Au_3^- ion trajectories than that of Cs^+ ions as described above. A countermeasure may be made in the future to avoid Cs^+ extractor affecting Au_3^- ion trajectories, so that Cs^+ and Au_3^- ions may be able to be controlled separately.

The transmission and cross-over diameter of each emission area are compared in Fig. 4.2.5. Amongst 768 ions generated from the 5th position (the cone aperture position) there were 662 ions (transmission of 86.2 %) passing through the cone

aperture forming a cross-over of Ø 0.55 (± 0.004) mm. The diagram shows a paradox – the 1st and 2nd areas render small cross-overs but low transmission, whilst the 5th a large cross-over but high transmission. In light of the result and that Cs^+ ions mainly fall in the region of 3rd-4th, the area in 3rd was thus considered a compromised choice for the next stage of simulation – the ion trajectories through SCIS-FLIG.

The Au_3^- ion beam was found to be hollow, which is not surprising as the emission comes from a virtual ring object (Each emission as shown in Fig. 4.2.1(b) can be seen as a ring). Most ion trajectories lie around the fringe of the beam leaving the centre scarce of ions. These off-axis rays have large angles to the optic axis and are consequently more subject to lens aberrations such as coma and astigmatism (Klemperer O, 1971). This will also result in a strong loss of ions in the FLIG column which contains 5 apertures in total. A stick or disk sputter target was then suggested by Prof Dowsett as a replacement for the cone design, and preliminary simulations showed that an Au_n^- beam with high transmission, a filled centre and a cross-over with a similar diameter can be obtained. However, due to constraints of time this idea was not implemented and will be described in Chapter 7 (Conclusions and Further Work). On the other hand, the hollow beam is favourable for reducing space charge effects (Klemperer O, 1971), which are caused by the inner charges of a beam according to Gauss's law.

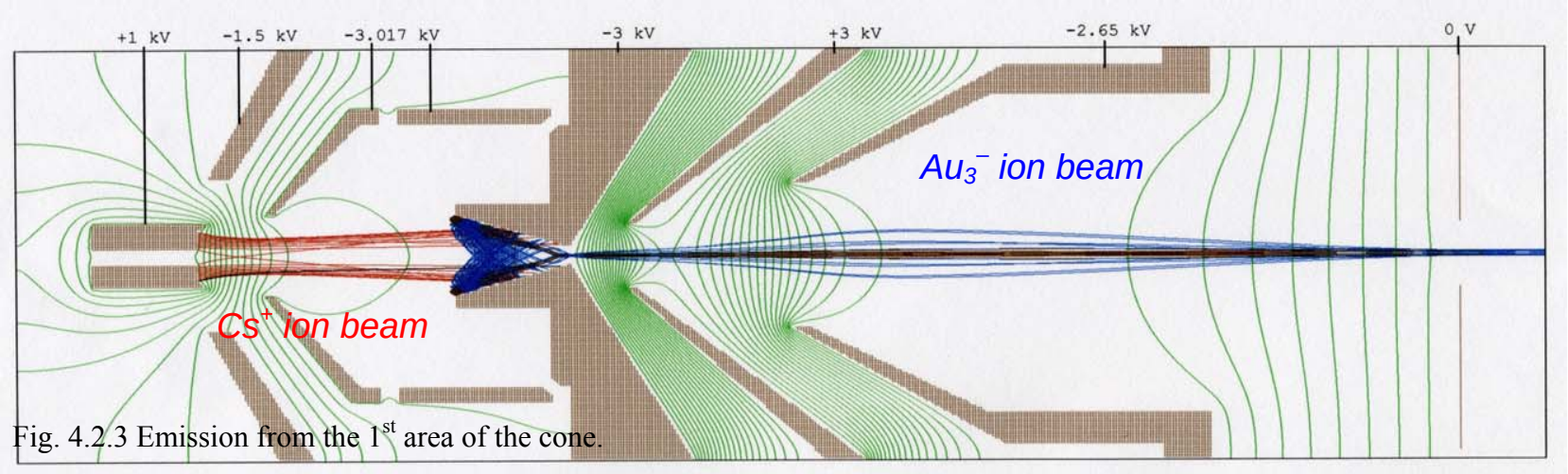

Fig. 4.2.3 Emission from the 1st area of the cone.

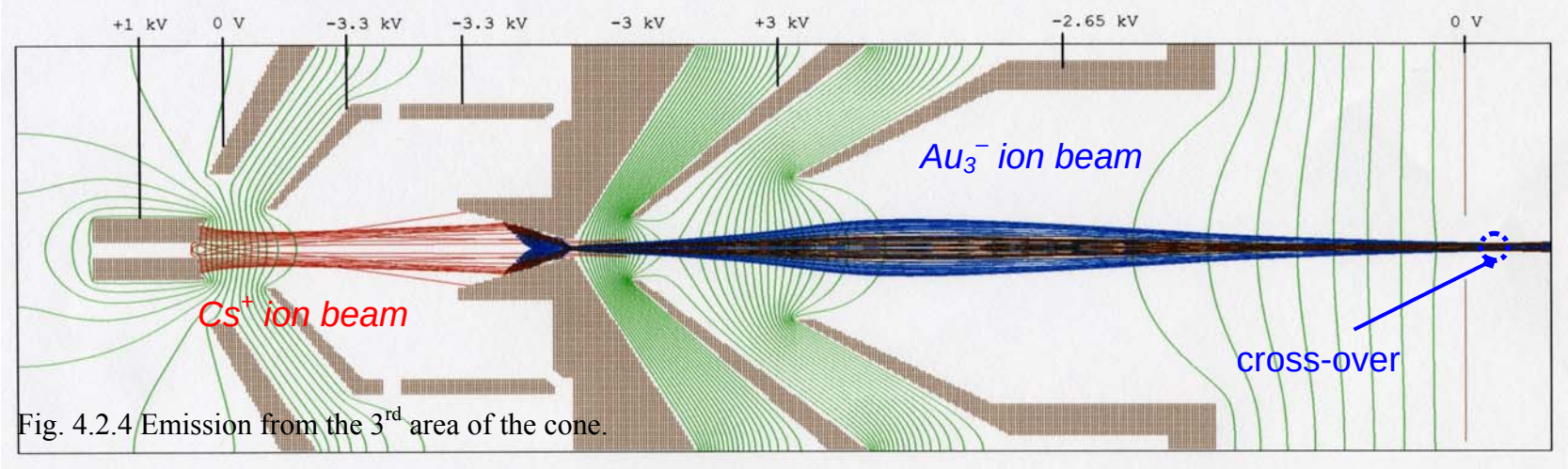

Fig. 4.2.4 Emission from the 3rd area of the cone.

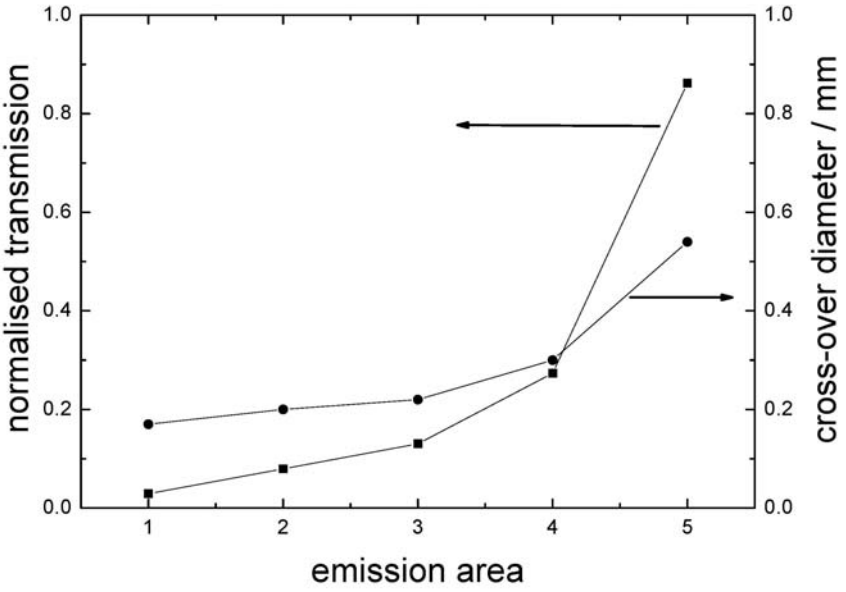

Fig. 4.2.5 The transmission and the cross-over diameter of the 5 emission areas. The errors for the transmission and the diameter are <0.01% and ± 0.004 mm respectively.

4.2.3 Space charge – comparison of SIMION simulation and El-Kareh and El-Kareh's theory

Without space charge effects, the cylindrically symmetric beam simulated in SIMION was focussed at 99.975 (± 0.0004) mm from the emitting position with a radius 0.1 (± 0.04) μm. This large radius, instead of being nil, is caused by the approximate ray position definition: e.g. for a coordinate of $\frac{0.1}{\sqrt{2}} \cong 0.0707106781$ mm, 0.0707 mm was entered for simulation. It is also because there are several thousand calculations between the start and end of a trajectory, which are subject to rounding errors. The analytical values calculated by El-Kareh and El-Kareh's method are 100.0034 (± 0.00004) mm with a radius 0 (± 0.00004) mm (Fig. 4.2.6).

The beam starts to suffer from space charge when the current reaches 197 nA where the beam radius starts to increase measurably. At this current, the beam waist is at 104.3 mm (from the emitting point) as calculated by El-Kareh and El-Kareh's method, and 104.6 mm in SIMION. Data were acquired for currents up to 1000 nA. As shown in Fig. 4.2.6 the beam waist position does not

differ much between the two methods, and the beam radii start to agree when the current is more than 500 nA.

In short, the simulation of space charge by SIMION can determine the position of the waist of a cylindrically symmetric beam in a field-free environment, but not the radius of the beam waist. Overall, the simulation should only be treated as a qualitative reference, as described above.

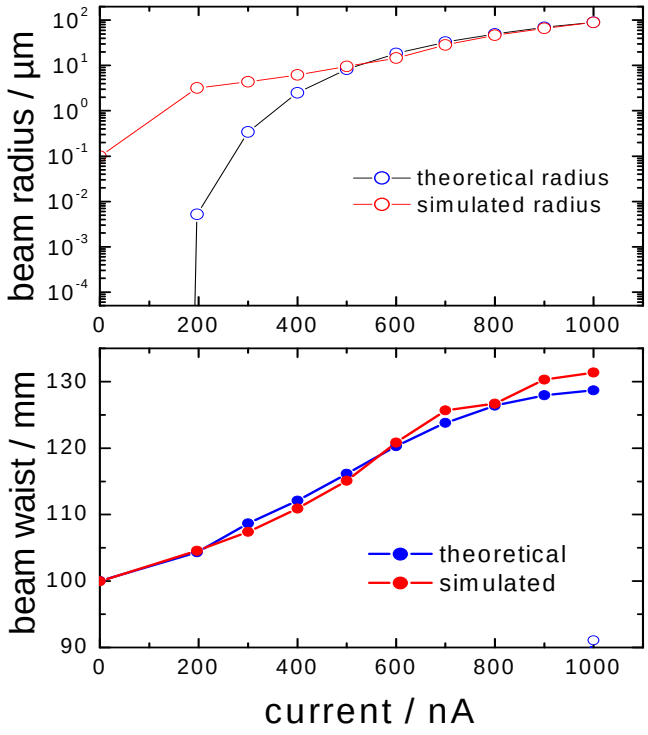

Fig. 4.2.6 Comparisons of beam waist position and radius between SIMION simulation and analytical calculations using the method of El-Kareh and El-Kareh. Errors are given in the text.

4.2.4 The simulation of space charge in SCIS-FLIG

An Au_3^- current of 10 nA was tested. The cone extractor potentials were optimised for best beam transmission through the FLIG column, as shown in Fig. 4.2.7(a). The floating potential was fixed at 5 keV, and the cone -1 keV, which lead to an accelerating energy of 6 keV for the ions. The beam successfully transmitted through the column without any loss. The current was then increased to 100 nA which can be considered as the case in which the

secondary electrons also participate in the beam. As shown in Fig. 4.2.7(b) most ions stop at the variable aperture (Ø 500 μm). Attempts were made to improve the beam transmission by changing the extractor potentials but these failed. Currents higher than 100 nA led to even worse results. (Note that rays of electrons should stop in front of the Wien filter as shown in Fig. 4.2.7 (c). The effect however cannot be shown in Fig. 4.2.7 (b), because SIMION only allows simulation of space charge effects with a single species.) In practice, it is expected that the abundant electrons present in the beam before the Wien filter would result in strong space charge effects to the beam and reduce the transmission of gold ions.

Later on a magnet array was added surrounding the SCIS, as shown in Fig. 4.2.7 (c), which created a magnetic field of 1.8×10^{-3} T (± 2.2 %) in the extraction field and easily deflected electrons (red rays) out of the beam without disturbing the Au_3^- ion (blue rays) trajectories. This is because the force exerted on the charged particles by the magnetic field is proportionate to the particle's velocity, and with the same initial energy electrons have a much higher velocity compared to gold ions due to its much lower mass. Thus, the Au_3^- ions (10 nA) can now pass through the column as if there were no significant space charge. In this figure, it can also be seen that the electrons cannot pass the high magnetic fringe field of the Wien filter.

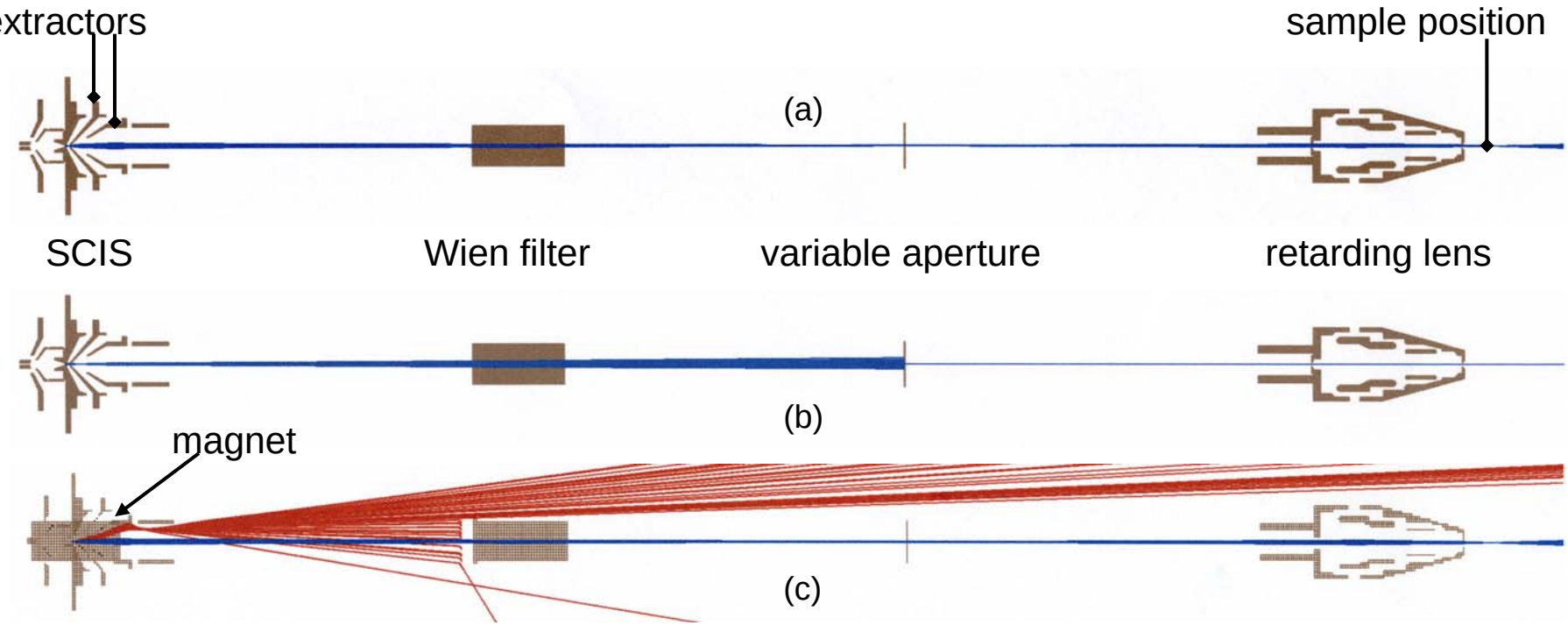

Fig. 4.2.7 Simulations of space charge of the SCIS-FLIG: (a) 10 nA Au_3^-, (b) 100 nA Au_3^-, (c) 10 nA Au_3^- (blue rays) with the secondary electrons (red rays) deflected by the additional magnetic field.

4.3 The retrofit of the SCIS to the FLIG

The SCIS was originally designed as such to fit onto the primary ion gun of the CAMECA IMS 4f instrument with compatible ion-optics, power supplies and vacuum connection. For the EVA 2000 primary FLIG column, these features needed to be reconsidered and possibly redesigned. Additionally a new mass separator (Wien filter) was required in order to separate the intended ions of Au_n^- as well as other undesirable molecular ions such as Au_nCs^- from each other (e.g. $^{527}Au_2Cs^-$ from the $^{591}Au_3^-$).

4.3.1 An additional lensing electrode and manifolds

The SCIS was originally equipped with two electrodes to extract and accelerate the ions sputtered from the cone. These two extractors were simulated and found to be incapable of transmitting the cluster ions through the FLIG column. An additional ion-optical lensing electrode was thus designed.

As shown in Fig. 4.3.1, the SCIS model was combined with that for the FLIG (Dowsett M G, copyright designs, 1995) on the optical bench of SIMION. All pieces were positioned with their relative distances as in the EVA 2000 FLIG column. The simulated ions are as defined in section 4.2.1, but the ions now have an energy of 1 keV at the sample. This was later proved to be an incorrect approach, as latter simulations and experimental results show that the highest current density on the sample is due to the emission from the cone aperture area. This will be discussed in Chapter 5, which deals with the improvement of the source.

The simulation was aimed at obtaining highest ion transmission through the column with smallest beam spot at the sample position, by changing electrode potentials, the relative position of the SCIS to the FLIG and designing additional ion optics. The optimal condition we obtained was with a beam of Ø 0.86 (± 4.7%) mm at the variable aperture (Ø 0.5 mm) position at a

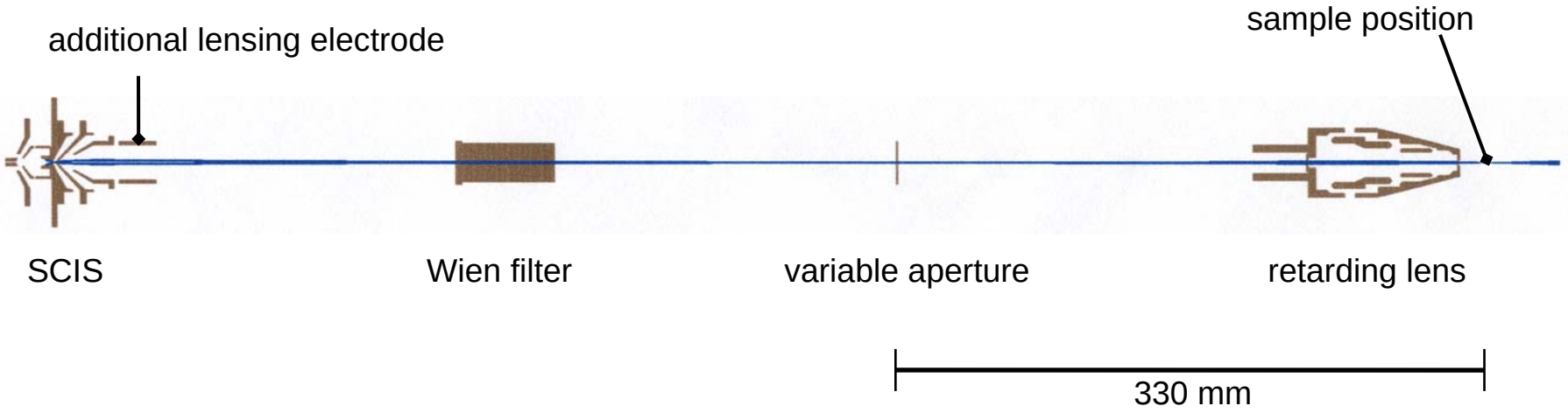

Fig. 4.3.1 The simulation of an Au_3^- ion beam transmitting through the FLIG column and the designed additional lensing electrode.

transmission of 36 % through the variable aperture, and Ø40 (± 1%) μm at the sample position. (Note the transmission through the variable aperture was calculated as the ratio of the ions that pass through the aperture to all the ions that travel to the aperture position which may or may not pass.)

After the simulation, the engineering drawing of the additional lens electrode was made by the author using the CAD software, Alibre Design®. The orthographic projection of the electrode is shown in Fig. 4.3.2. The piece was machined by Mr Derrick Richards.

A set of Conflat® vacuum manifolds, shown in Fig. 4.3.3, was designed to mechanically match the SCIS to the FLIG. These three manifolds are meant to conjoin the SCIS and the FLIG, to hold the accelerating lenses and to accommodate electrical feedthroughs.

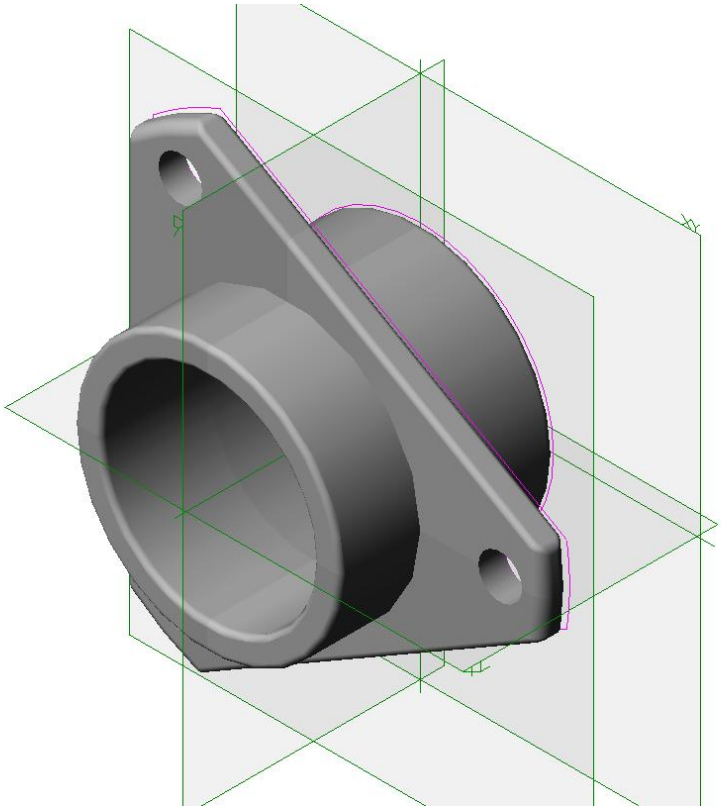

Fig. 4.3.2 Orthographic projection of the additional lensing electrode.

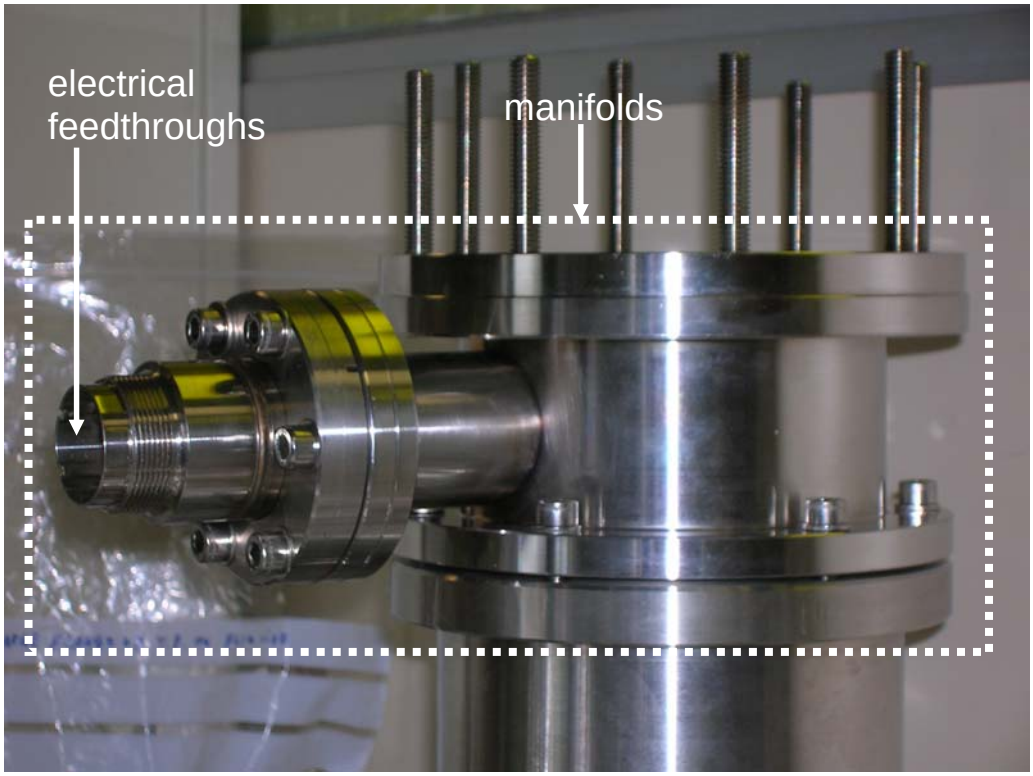

Fig. 4.3.3 The manifolds designed to retrofit the SCIS onto the FLIG.

4.3.2 Mass separator (Wien filter)

Wien filters are often used in ion columns for separating primary ions with different masses and can be easily explained by the Lorentz's force equation,

$$\vec{F} = q\,(\vec{E} + \vec{u} \times \vec{B})\,, \qquad \text{(Eqn. 4.3.1)}$$

where $\vec{F}$ is the overall force the ion experiences. $\vec{E}$ is the electric field, $\vec{B}$ is the magnetic field, $\vec{u}$ is the velocity of the ion and q is the charge the ion carries (Fig. 4.3.4). If each ion in a beam carries the same charge, when they arrive the field they would have been accelerated by the same differential potential regardless of their mass, and thus ions with different masses (m) will pass through the Wien filter with different velocities:

$$u = (2qV/m)^{1/2}\,, \qquad \text{(Eqn. 4.3.2)}$$

where V is the differential potential. Thus for a given fixed set of fields, only the ions having a velocity satisfying

$$\vec{E} = -\vec{u} \times \vec{B} \qquad \text{(Eqn. 4.3.3)}$$

can pass through the field without any deflection.

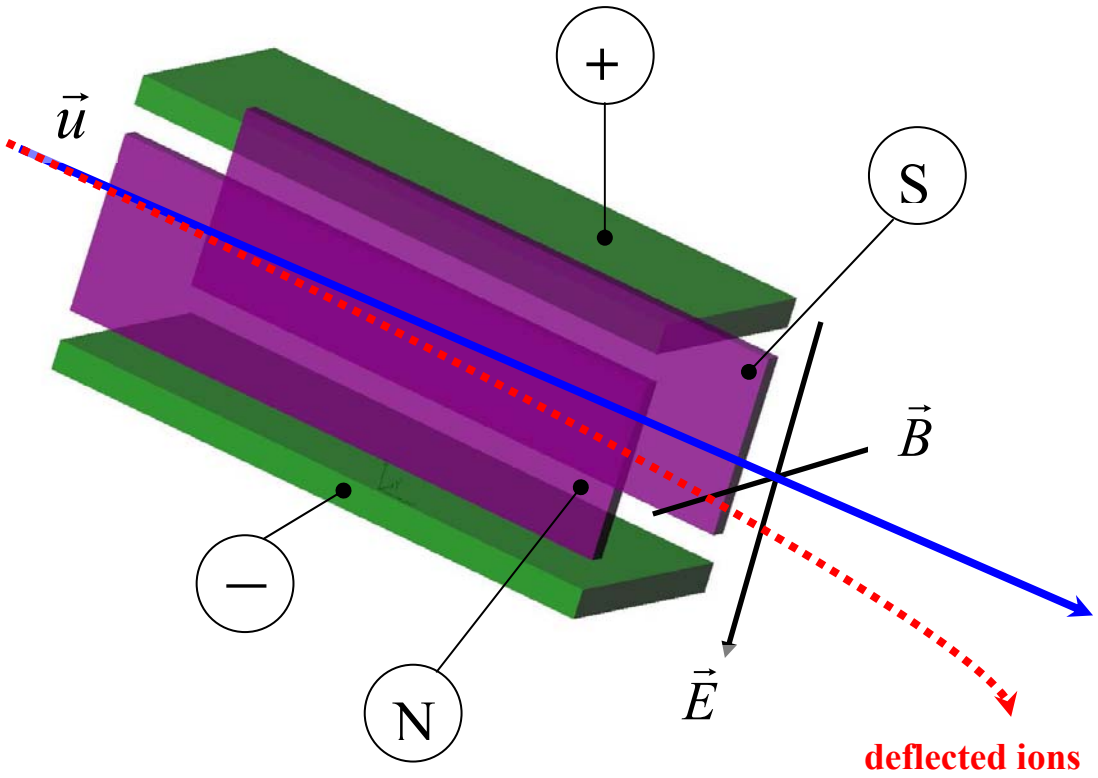

Fig. 4.3.4 Schematic diagram of the Wien filter used for mass separation. (Note in the FLIG, all electrodes of the Wien filter are floated.)

In the case of the SCIS-FLIG, changes in the float potential V_F and/or the cone potential V_c lead to change of V (= V_F-V_c). Thus $\vec{E}$ in the Wien filter will need to change so as to pass the same ion species through the Wien filter, provided other parameters remain the same. For example, if V changes from 1 kV to 5.7 kV, $\vec{E}$ would need to increase by a factor of $\sqrt{5.7}$. Similarly, if one desires to change the ion species in terms of ion mass, say from Au_1^- to Au_2^-, one would need to change $\vec{E}$ by a factor of $\frac{1}{\sqrt{2}}$.

The Wien filter on the EVA 2000 FLIG was originally designed to separate light mass gas ions, such as $^{32}O_2^+$. The Au cone after having been sputtered will generate various high mass species including Au_n^- (n = 1-5) and Au_nCs^- (n = 1-4). We employed SIMION to simulate the old Wien filter, and the results indicated the magnetic field needed to be at least doubled so as to separate $^{591}Au_3^-$ from $^{527}Au_2Cs^-$ and $^{724}Au_3Cs^-$ at the variable aperture (Ø 500 μm),

provided the positions of the Wien filter and the variable aperture in the FLIG remained as they were. The author bought a pair of neodymium-iron magnets (Eclipse Magnetics Ltd., part No. N35A605015) and designed a new outer magnetic circuit for the Wien filter, which sits outside the FLIG, as shown in Fig. 4.3.5 (a) (also Fig. 3.2.4). The magnetic flux density ($\vec{B}$) at the magnet surface was measured 2.6×10^{-1} T (the old one is 2.3×10^{-1} ($\pm 4\times10^{-3}$) T), and since its total area is 2.9 times greater, the total flux is estimated to be 3.2 times that of the original. Because the inner magnetic circuit of the Wien filter (inside the FLIG chamber), as shown in Fig. 4.3.5 (b), through which the flux flows, remains the same, the magnetic field that the ions would experience is 3.2 times that of the original, neglecting any fringing effects. Obviously, the design of an outer magnetic circuit makes changing magnetic field inside the FLIG easier.

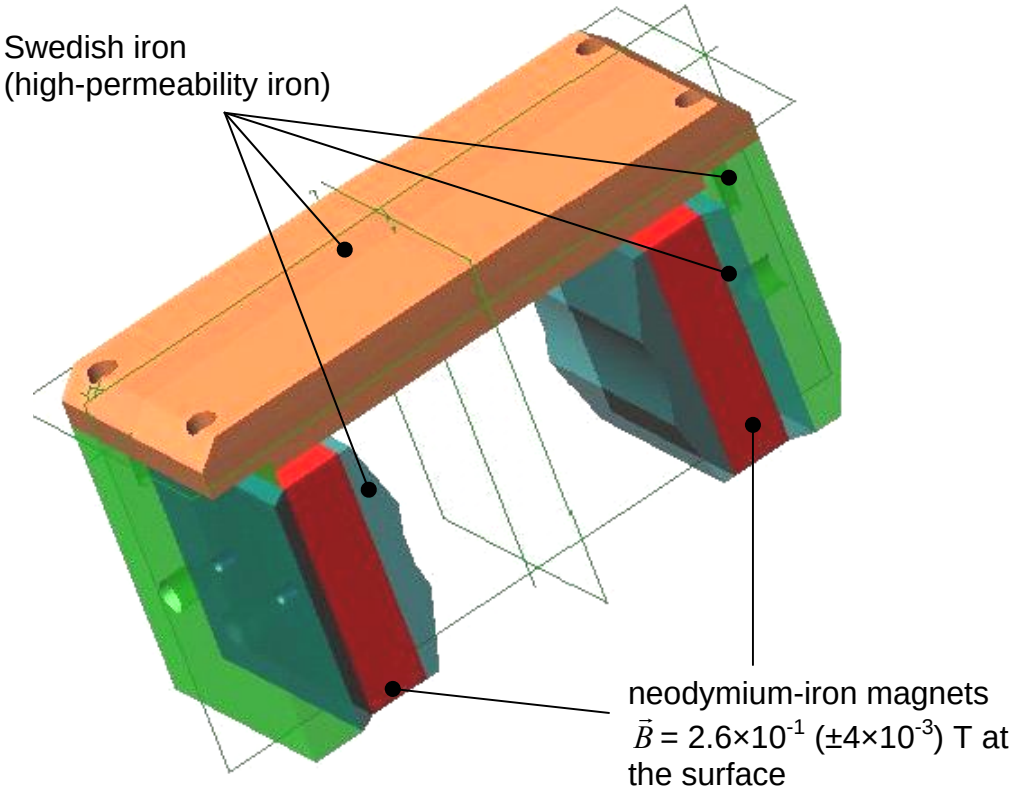

Fig. 4.3.5 (a) The newly designed outer magnetic circuit for the Wien filter to separate gold ions.

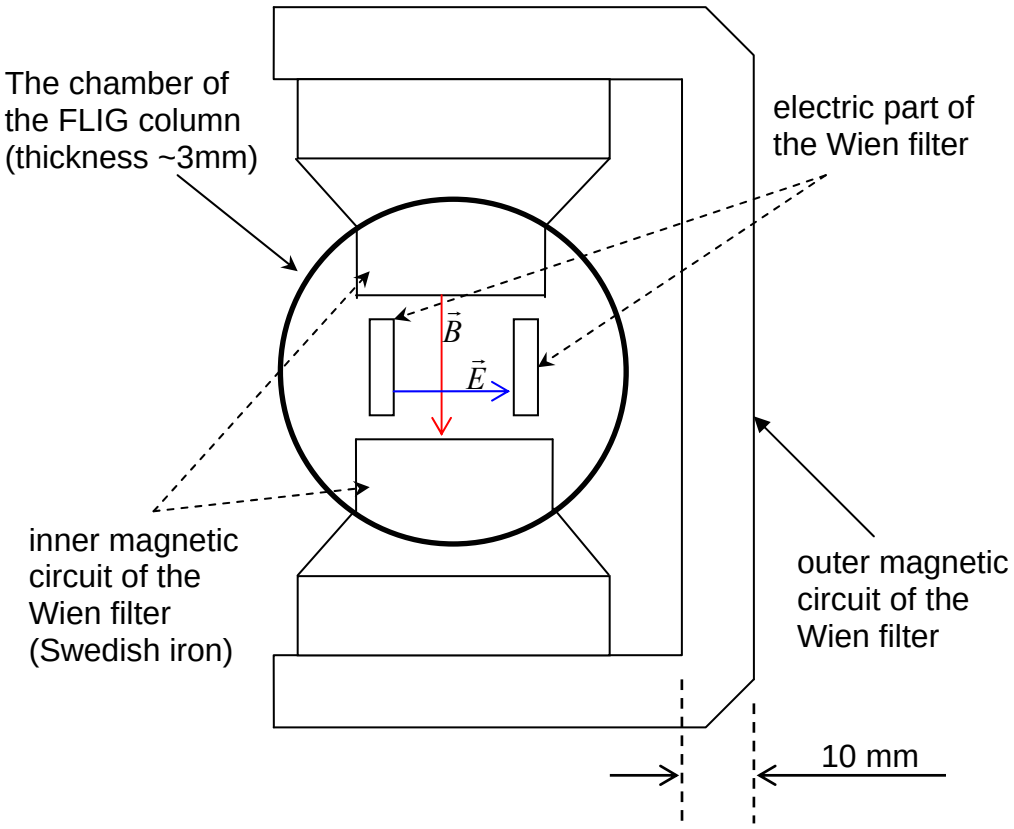

Fig. 4.3.5 (b) Schematic diagram of the cross-sectional view of the designed Wien filter (Fig. 3.2.4), including both the electric and magnetic parts. The magnetic part consists of the inner and outer circuits, which make changing the magnetic field inside the FLIG easier.

4.3.3 The design of the electrical scheme

In order to meet our experimental requirement that the primary cluster ions can have an impact energy in the broad range of ± 1-10 keV, an electrical scheme was designed as shown in Fig. 4.3.6 with it specifications listed in Table 4.3.1. In addition to these specifications, the following requirements were also imposed:

- Voltage ripple needs to be constrained at < 0.1%. Ripple contributes to chromatic effects (section 3.2) in the ion beam and also positional instability, consequently reducing the transmission of the beam through the ion column.

- Any ripple on the power supply units from the cone onwards through the FLIG needs to be synchronised, so that the resulting errors do not accumulate.
- The existing power supply units which provided FLIG potentials for normal use (O_2^+ and Cs^+ ions) only gave negative potentials and so needed to be adapted for bi-polar ion transmission.

As can be seen in Table 4.3.1, power supply units 1-6 are commercial modules, and 10-13 which supply lenses were custom-designed by Mr Adrian Lovejoy in the Physics Electronics Workshop in order to diminish power supply ripple problems. The units 10-13 were constructed by the author.

It was found later from experiments that secondary electrons sputtered from the cone had not been taken into consideration in the first design, and many units such as those responsible for the potentials of the Cs^+ gun, first and second extractors (of Au_n^- ions) and even the FLIG column had too large an output impedance to maintain stable potentials – i.e. an inadequate sink or source current. The electrical scheme was then extensively modified to correct this problem (Chapter 5).

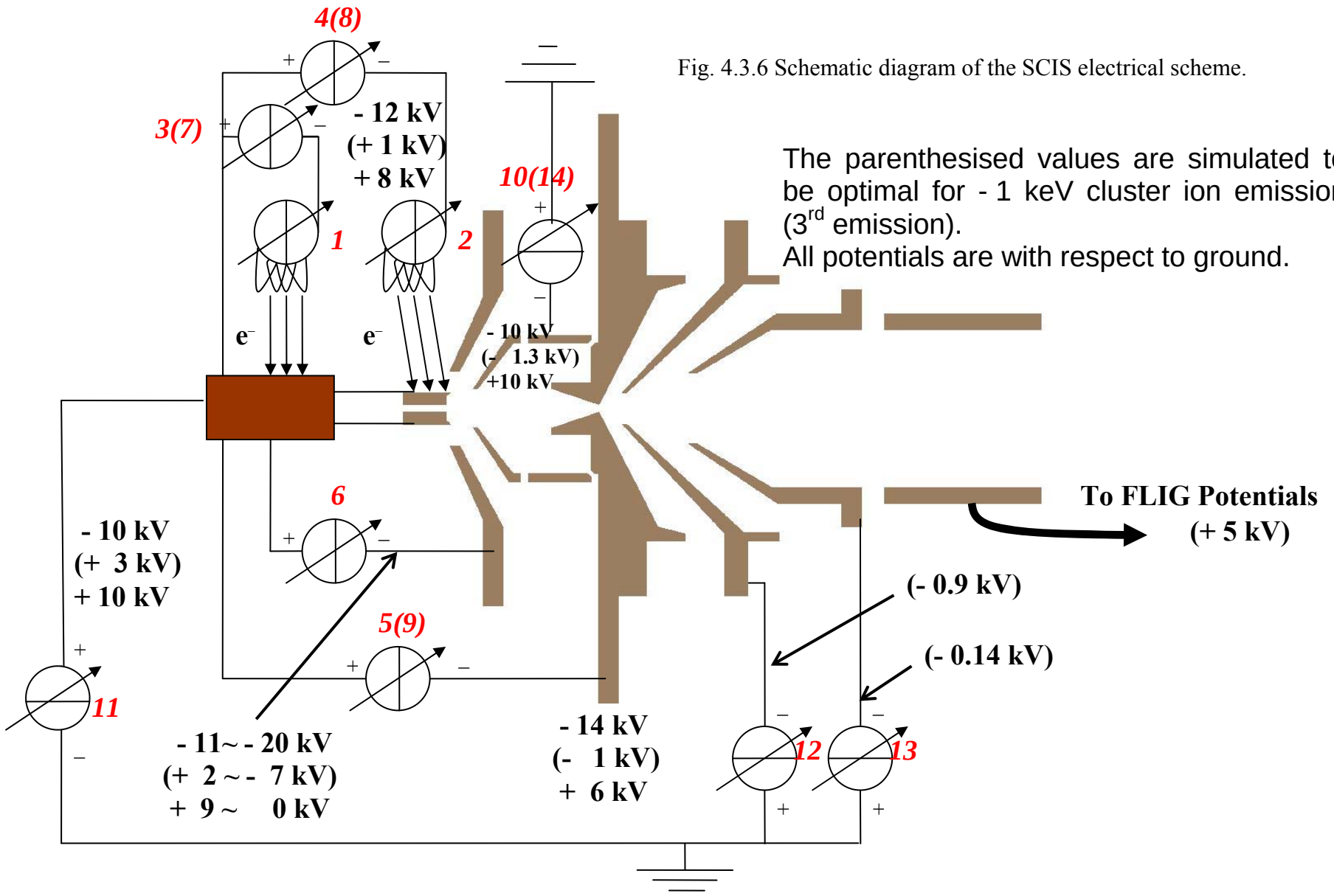

Fig. 4.3.6 Schematic diagram of the SCIS electrical scheme.

The parenthesised values are simulated to be optimal for - 1 keV cluster ion emission (3rd emission).
All potentials are with respect to ground.

Table 4.3.1 Specifications of the SCIS power supplies.

Number	Descriptions	Specifications	Module	Quantity
1, 2	The electron emission filament PSUs to heat up the CsCl reservoir and the Cs^+ ioniser	7.5 V at 5 A, isolated to 5 kV	Applied Kilovolts FF005DAA060, ripple less than 200 mV peak to peak	2
3(7), 4(8)	The PSUs to maintain the relative potential between the Cs^+ gun and the filaments	- 10 V to - 2.5 kV at 4 mA (10 watts)	Applied Kilovolts HP2.5NAA025, ripple 10 mV peak to peak	2
5(9)	The PSU to maintain the relative potential between the Cs^+ gun and the sputter cone	+ 10 V to - 5 kV at 2 mA (10 watts)	Applied Kilovolts HP005NAA025, ripple 20 mV peak to peak	1
6	The PSU to maintain the relative potential between the Cs^+ gun to its extractor	- 20 V to - 10 kV at 1 mA (10 watts)	Applied Kilovolts HP010NAA025, ripple 50 mV peak to peak	1
10(14), 11, 12, 13	The PSUs to maintain the potentials of the shield, Cs^+ gun and two extractors	± 20 V to ± 10 kV at 10 μA (0.1 watts)	Custom-designed in the Departmental Electronics Workshop and constructed by the author	4

Chapter 5 Improvements and Characterisation of SCIS-FLIG

The source was fitted on the FLIG with the devices designed (Chapter 4). Before the characterisation was begun, the source was tested deliberately to find problems that would affect the source operation. Some of the problems discovered were solved, in that the source reliability and stability were established to a certain degree; whilst others remain as further work (Chapter 7). The characterisation of the 1 keV Au_n^- (n = 1-3) ion beams is discussed in this chapter in terms of current, mass spectra, spot size, reliability and the dependence on vacuum status and Cs^+ sputtering energy. Ions carrying higher energy (> 1keV) and positively charged ions (Au_n^+) were studied, nevertheless in less details. A new emission system was designed and proved to provide higher beam transmission through the FLIG.

5.1 The defects and improvements of the source

Several issues were identified which delayed the characterisation of the source. Generally, they are about the electrode insulation, the vacuum and the capability of the used power supply units (PSUs) in terms of heat dissipation and sinking and sourcing currents.

5.1.1 Arcing and current leakage

Electrical arcing was a serious problem in initial tests, and some PSUs were damaged. It was found arcing occurred at the pins of the electrical feedthrough (Fig. 4.3.3) which supply potentials to the cone and the lens. The pins themselves are rated for potential difference more than 10 kV, but if the connector that couples the pin to a wire is not clamped well, arcing occurs

between connectors, as shown in Fig. 5.1.1. This problem was solved by putting the connectors into PTFE tubes to enhance the insulating strength.

Since the source is based on sputtering, after some time of operation insulators would be coated by metallic materials, such as caesium, gold, and iron and nickel from stainless steel. This induced current leakage and arcing, which happened most frequently between the cone, the shield, and the caesium ion gun. As a result, there was cross-talk between the applied potentials. This also happened often between the cone and the 1st extractor. Generally, leakage worsens with time due to increased metal coverage. A longer insulator might have improved things, but might also have affected the source performance.

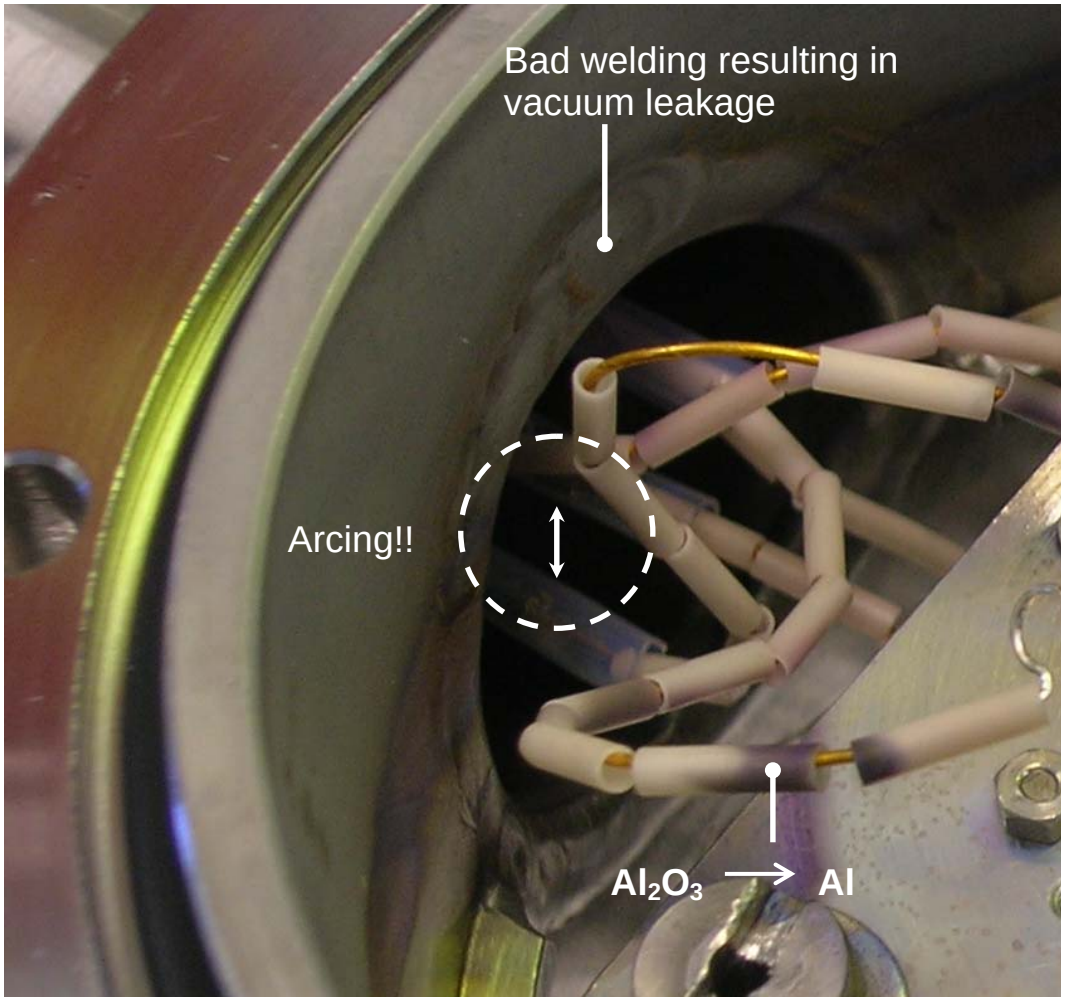

Fig. 5.1.1 Arcing was observed between the connectors (linking the wires to the feedthrough pins) when the source was tested for the first time. The connectors were put in PTFE tubes and the arcing prevented. Also shown is one of the badly welded areas that gave rise to vacuum leakage (section 5.1.4). The used insulator Alumina (Al_2O_3) changed to aluminium (Al) when the oxygen was taken away by the deposited Cs atoms, which resulted in electricity leakage.

5.1.2 Filament issues

The heating system for Cs^+ ion emission used electron bombardment (section 3.3.1.1), and consists of two tungsten wires, one for the ioniser and another for the CsCl reservoir. It was found that the filament was flexible when being heated for the first time and could short to the surrounding electrodes or itself, as shown in Fig. 5.1.2. Consequently, the electron emission would be reduced or stop. After heating, the filament became rigid (and brittle) and so the shorting problems happened less frequently. This problem was solved by very slowly heating the filament when it was used for the first time. A better way is to add one more filament support, and attention should be paid to preventing the filament from shorting to itself. Alternatively, the heating system can be changed to a conduction type, where filaments are usually protected by insulators. This problem has not yet been observed on the reservoir filament because it is further from its surrounding electrodes, and its two supports are separated by a larger distance that prevents it from shorting to itself.

Another problem was due to the fact that the plate (as shown in Fig. 5.1.2) on which the filament supports stand was electrically grounded. It happened that the ceramics acting as insulators between the filament supports and the plate were attacked by caesium and their surface conductivity increased too quickly. Indeed, because they are made of alumina (Al_2O_3), the surfaces of the ceramics were always found covered by a grey film which was aluminium from the reduction of alumina (Fig. 5.1.1). As a consequence, the filaments were shorted to ground and emitted no more electrons. To solve the problem, the plate was electrically connected to one end of a filament.

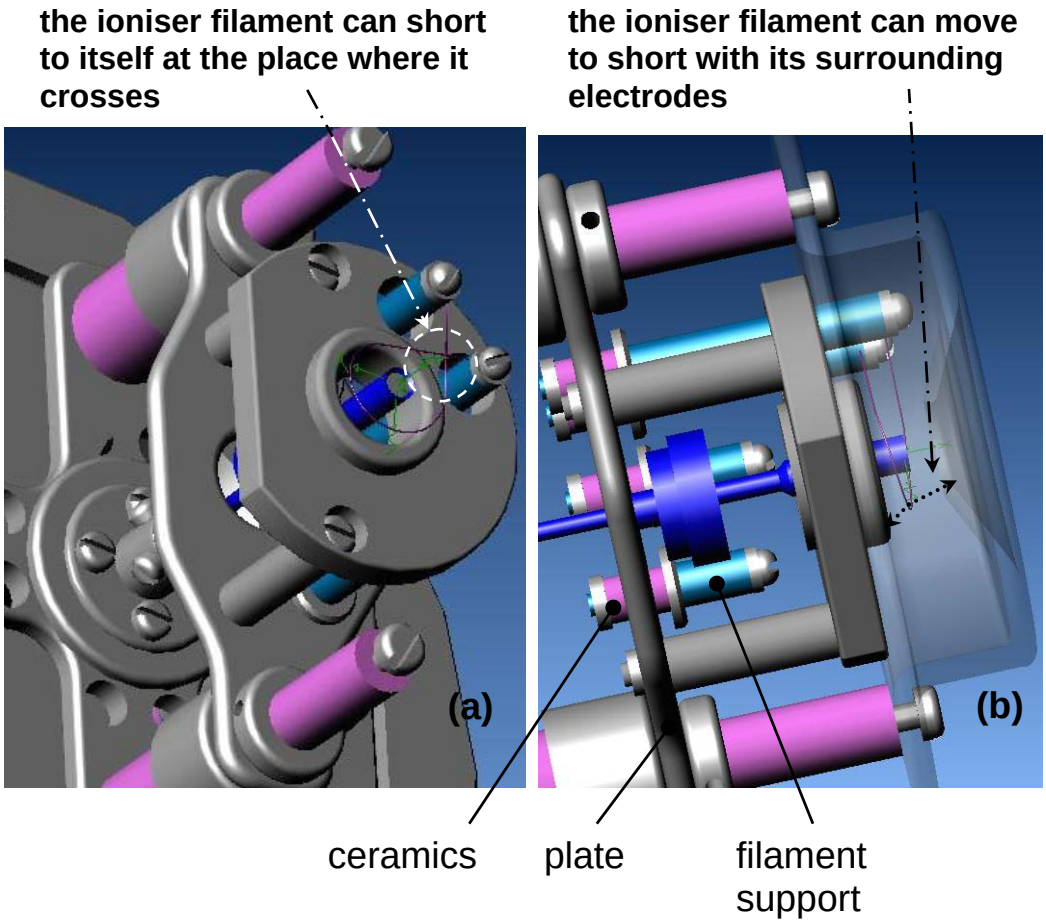

Fig. 5.1.2 The ioniser filament was found to easily short to itself (a), and the surrounding electrodes (b), when it was heated up for the first time. The ceramics in between the filament supports and the plate which fixes the supports were found covered by metallic materials that the insulating properties stopped (b). (referred to Fig. 3.3.1 and 3.3.2)

Another problem induced by the ioniser filament is that the emitted electrons can be also attracted to the Cs^+ extractor if it has a more positive potential (Fig. 5.1.3). This effect was observed when the Cs^+ extractor potential was regulated to focus the Cs^+ ions into the cone to get a larger current at the sample. However, the potential was found to depend on the ioniser filament emission current, and could not be regulated to more than +100 V with respect to the filament potential.

We observed that, by regulating the extractor potential to a more positive potential, a bigger gold current on the sample was obtained. Simulation also showed that a potential of 0 to +0.5 kV with respect to the ion gun results in more Cs^+ ions falling on the $4^{th}/5^{th}$ area on the cone (Fig. 4.2.1 (a)). This area was later confirmed to make the major contribution of the gold ion current at the

sample. A screen was thus devised to prevent electrons from reaching the extractor in order to obtain proper control of its potential. This device was made and is shown in Fig. 5.1.4.

The screen was tested and proved to be advantageous for obtaining higher current at the cone and the sample. Nevertheless due to the small gap between the device to the extractor and the ioniser filament, it tended to short to one or the other, and consequently led to frequent source maintenance. The screen was taken away eventually and further design is required.

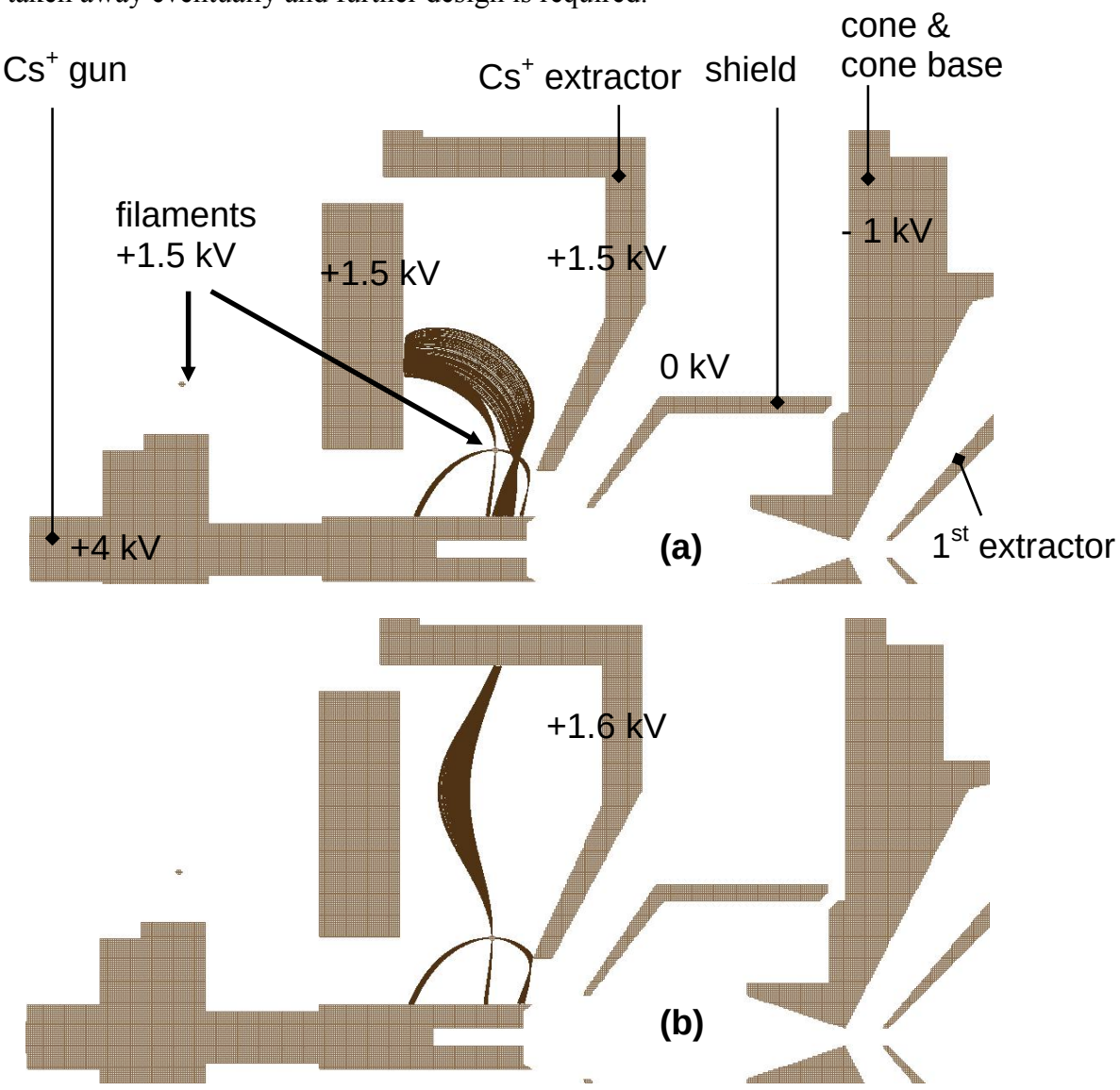

Fig. 5.1.3 Simulation of the electron trajectories emitted from the ioniser filament. The electrons emitted from the ioniser filament are attracted to the Cs^+ ion extractor when the extractor potential is more positive than that of the filament. This limits the controllability of the extractor potential, and thus the Cs^+ ion trajectories. All the electrode potentials in (b) are the same as in (a) except that of the extractor is 100 volts more.

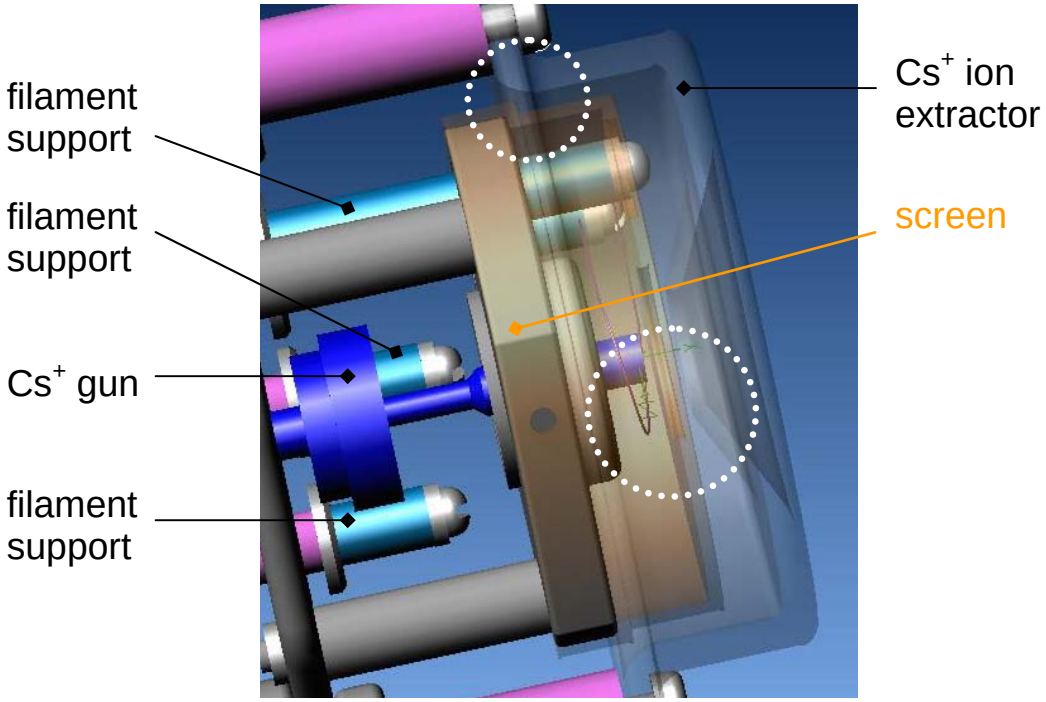

Fig. 5.1.4 The designed screen to prevent the electrons emitted from the ioniser filament from being attracted to the Cs^+ ion extractor. The device was found to short with the extractor or the filament easily (dotted circled area) when the source was hot.

5.1.3 Issues related to power supply units

Several PSUs were found to be uncontrollable, and thus the beam was not stable and the lenses could not be operated at their best condition. Basically the problems were categorised into two groups: (i) the PSUs were not adequate in sourcing or sinking the current which is generated by the source, and (ii) heat dissipation in PSUs.

5.1.3.1 Inadequate sourcing and sinking currents

Inadequate sourcing and/or sinking of current was discovered for the PSUs which supply V_F (floating potential), V_i (Cs^+ ioniser potential), V_1 (the 1st $Au_n^{\pm}$ ion extractor potential) and V_{sh} (shield potential).

As the operation of SCIS is based on sputtering, the source generates Cs^+ ions, $Au_n^{\pm}$ ions and secondary electrons, e^-. These charged particles can be collected by the shield electrode, the Cs^+ ioniser, the 1st and 2nd extractors as well as the FLIG column (Fig. 5.1.5), which may result in PSU potential instability.

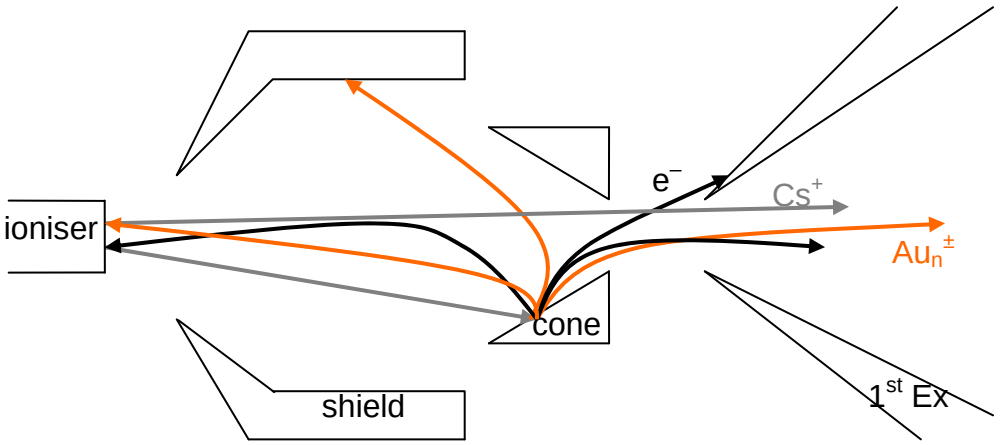

Fig. 5.1.5 Schematic diagram of the trajectories of the charged particles generated in the SCIS.

A PSU that has an output impedance which is too high will have the problem of inadequate sourcing and/or sinking current (Fig. 5.1.6).

In terms of a sourcing current,

$$V_{OUT} = V_S - I_{SO}R_S, \qquad \text{(Eqn. 5.1.1)}$$

where V_{OUT} is the potential on the instrument (load), and V_S, I_{SO} and R_S are the source potential, sourcing current and output impedance of the PSU in question respectively. V_S and R_S are fixed, and therefore when I_{SO} increases V_{OUT} decreases. For example, this happened at the V_F PSU, which supplies a positive current. The e^- current infusing into the PSU through the FLIG column is equivalent to an addition to its I_{SO}.

In terms of a sinking current,

$$V_{OUT} = V_S + I_{SI}R_S, \qquad \text{(Eqn. 5.1.2)}$$

where I_{SI} is the sinking current of the PSU. When I_{SI} increases, V_{OUT} increases too. This was usually observed at the PSUs for V_{sh} and V_1, both supply a negative current for Au_n^- emission. Because they absorbed a lot of secondary e^-, the potentials on these two electrodes were found to be out of control and to follow the Cs^+ ion emission current that generates secondary e^-.

The defective PSUs were either replaced by supplies with smaller output impedance, or by shunting the current through an additional resistor in parallel to R_S.

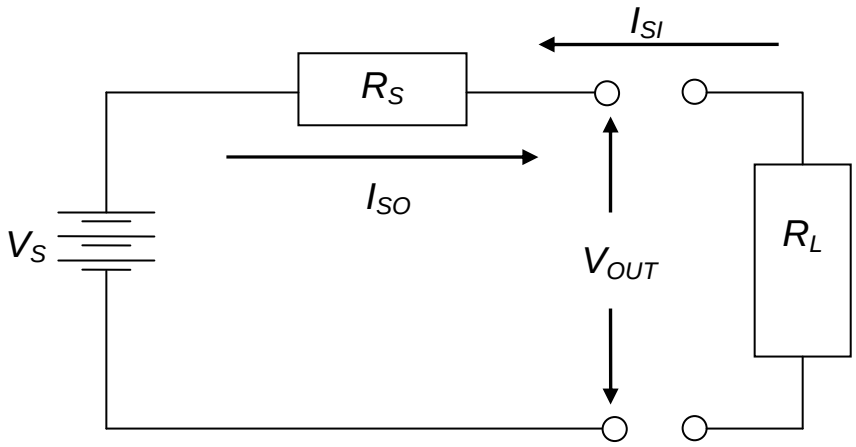

Fig. 5.1.6 Circuitry showing that the output voltage of a PSU, V_{OUT}, is influenced by its output impedance R_S, the sourcing current, I_{SO}, and the sinking current, I_{SI}.

5.1.3.2 Heat dissipation

Another problem was related to the PSUs which controlled the potentials of the Wien filter as well as the steering plates behind the variable aperture (VA, Fig. 3.2.1). They were designed and built in a case which was floated on the FLIG column, V_F, and this floated case was then put into another case which is electrically grounded with a means for insulation. This double-case design made heat dissipation inefficient, and consequently the electronics malfunctioned. The lid of the inside case was omitted (so there is only one lid on top of all the electronics) and a fan was added for ventilation.

5.1.4 Low vacuum and leakage

Vacuum leaks were in the manifolds due to bad welding at the joint area when the source was first time pumped for high vacuum. Fig. 5.1.1 shows one of the welds that leaked. The leaks were repaired by re-welding.

The degree of vacuum in the SCIS-FLIG (Fig. 3.1.2) affects two things. One is the reliability of the source operation, and the other is the Au_n^- ion yields. The originally used turbo-molecular pump (Pfeiffer Vacuum Inc., Model: TPU170, pumping speed of N_2: 170 L s^{-1}) for the source was found to have too low a pumping speed. The pressure P_F (the pressure measured in the SCIS-FLIG column) always rose from 10^{-7} mbar to 10^{-6} mbar when the filaments started to emit electrons, and worsened to almost 10^{-5} mbar before any electrical arcing occurred and experiment sessions stopped. This not only made precise experiments impossible, but also frequently damaged the power supply units. Besides, when the pressure was about 10^{-6} mbar the $\frac{I_{Au_1^-}}{I_{Cs^+}}$ ratio usually dropped to less than half of that when the pressure was 10^{-7} mbar ($I_{Au_1^-}$ being the monomer gold ion current measured at the sample, and I_{Cs^+} the caesium current measured at the cone). The poor vacuum is also bad for the dimmer and trimmer gold ion emissions, the ratio $I_{Au_1^-} : I_{Au_2^-} : I_{Au_3^-}$ was approximately 30:20:1 for $P_F \sim 10^{-6}$ mbar and 18:1.3:1 for $P_F \sim 10^{-7}$ mbar. This effect was also reported in the work by Belykh (Belykh S F *et al.*, 1992), where the yield of Au_1^- drops with the worsened pressure (for 10^{-6} Torr, the yield was about 30% of that when the pressure was 10^{-8} Torr). This problem was solved by the replacement of a new turbo pump, which has a higher pumping speed (Leybold Vakuum GmbH, Model: TURBOVAC 340M, pumping speed of N_2: 320 L s^{-1}).

5.2 Characterisation of 1 keV Au_n^- ion beams

A set of experiments was performed in order to understand the characteristics of the source on the FLIG. The first observations of ultra low energy Au clusters were made, and insight into how the source can be improved so as to be more useful for the SIMS tasks was discussed.

5.2.1 Experimental

Because of the problems mentioned above, some of the preliminary data revealed here do not present the best performance of the source.

The cone aperture was Ø 0.5 mm or Ø 1 mm. The sputter energy of gold by the Cs^+ ions was 4-6 (±0.05) keV, and the gold cone was applied -1 (±0.05) kV. The Faraday cup sitting behind the sample holder was used to measure the current of ions passing through the FLIG. It was connected to ground through a bias of 0-27 V and a nano-amp meter. V_F was +4.7-5 kV ($\pm 5\times10^{-3}$ kV), except when we looked for gold ions for the first time in the FLIG column (at the variable aperture) it was applied ~0 V. The Au_n^- ion energy at the sample was thus about -1 keV. The potential on the Wien filter is denoted as V_{WF}. The measured current between the cone and the Cs^+ ion gun, I_{Cs^+}, was in the range 5-33 μA (this current includes Cs^+ ions, $Au_n^{\pm}$ ions and secondary electrons). The current on the 1st Au_n^- ion extractor ((8) in Fig. 3.3.1), I_1, was also monitored. The pressure P_F was 10^{-6}-10^{-7} mbar, and the pressure in the main chamber, P_{MC}, was about $2\text{-}8\times10^{-9}$ mbar. The variable aperture in the FLIG was Ø 800 μm if not otherwise stated (it can be easily changed to Ø 100, Ø 200 and Ø 300 μm).

5.2.2 Mass spectra

The first experimental objectives were to find -1 keV gold ions at the variable aperture, i.e. in the upper column of the FLIG, and to test the ion

separation of the Wien filter. This was done by connecting the variable aperture to ground, through a bias of +18 V (to attract the sputtered secondary electron by gold ion bombardment) and a nano-amp meter. The FLIG column was also connected to ground; lens 1 of the FLIG ("L1" in Fig. 3.2.1) thus operated as an Einzel lens (Klemperer O, 1971). In this case, the isolation valve (Ø 4 mm; Fig. 3.2.1) sits upper-stream of the variable aperture became the defining aperture for the Wien filter. The spectra were obtained by first optimising all the electrode potentials for highest Au_1^- transmission, and then swinging V_{WF} to find other ions (therefore the transmission for other ion species may not be ideal). The normalised mass spectra are shown in Fig. 5.2.1 as the blue dotted line. The peak magnitude of $I_{Au_1^-}$ is about -1.42 nA.

Efforts were then made to obtain the Au_n^- ions through the FLIG to the sample. V_F was set to +4.7 kV, and because the ion velocity in the FLIG was increased by a factor of $\sqrt{5.7}$, V_{WF} also needed to increase by a factor of $\sqrt{5.7}$ (section 4.3.2). The normalised mass spectra are shown as the green dotted line in Fig. 5.2.1, with $I_{Au_1^-}$ about -0.74 nA.

Clearly both mass spectra show three species, and they correspond to a monomer, a dimmer and a trimmer according to the V_{WF} value (section 4.3.2). No other species were found. Later, energy dispersive spectrometry in the SEM (Chapter 6) was used to measure the composition of the bombarded sample surface, and only gold and oxygen were found, other than the matrix materials. This proves the detected ions are of gold, i.e. Au_1^-, Au_2^- and Au_3^-. The values of V_{WF} were later simulated and showed the new Wien filter generates a total flux 2.8 times that of the old one, close to the initial estimation of 3.2 times (section 4.3.2).

The mass resolution for $I_{Au_1^-}$ in the Wien filter was measured by the full width half maximum (FWHM) as 8.5 V and 15 V for V_F = +0.018 and +4.7 kV respectively. The extrapolation of the spectra with V_F = +4.7 kV shows that when V_{WF} was tuned for Au_2^- emission there was 16 (±0.4) % of Au_3^- ions present in the beam; and when V_{WF} was tuned for Au_3^- emission there was 23 (±0.4) % of Au_2^- ions present. This low mass separation was mainly because the lens PSUs accumulated charge and could not be controlled for best ion

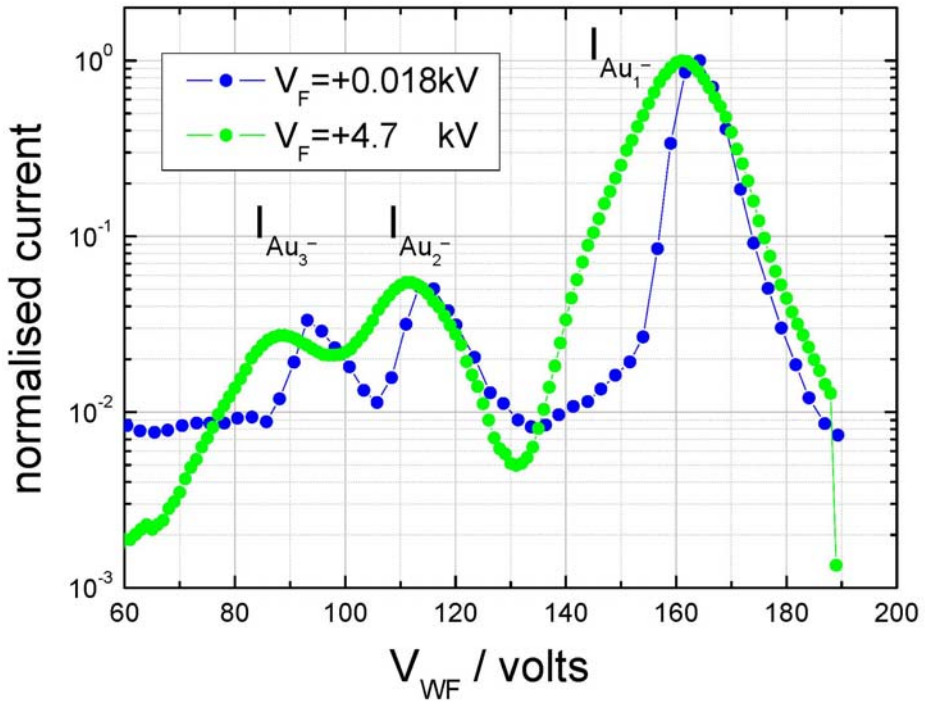

Fig. 5.2.1 The normalised ion mass spectra, measured at the variable aperture (V_F = +0.018 kV) and at the Faraday cup (V_F = +4.7 kV). The detected monomer, dimmer and trimmer ion species were proved to be of gold. No other species can be observed. The error was in the range of 2.8×10^{-3} % to 2.8×10^{-1} %.

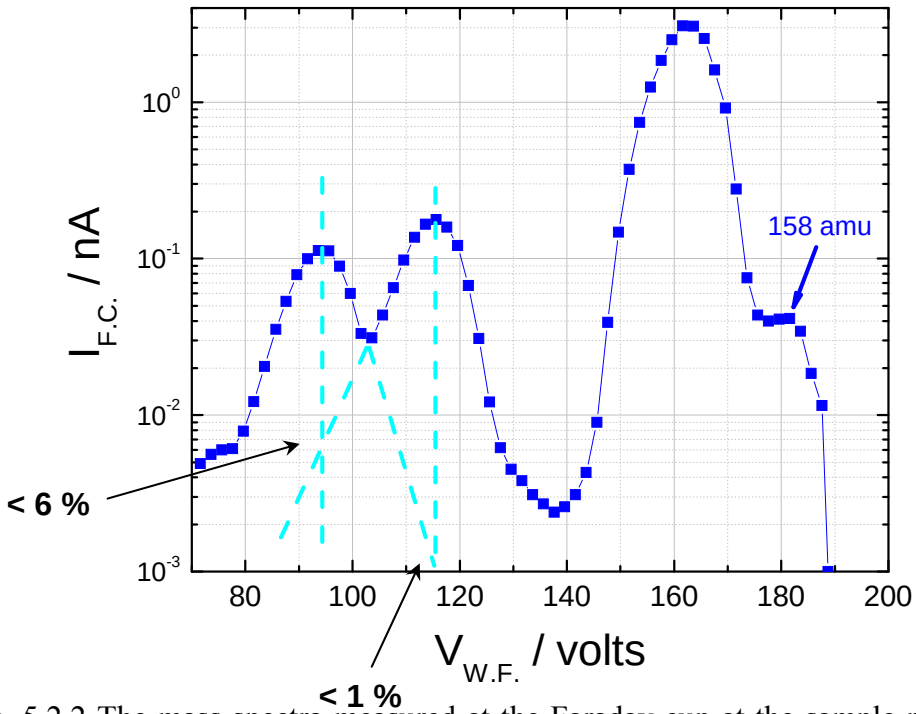

Fig. 5.2.2 The mass spectra measured at the Faraday cup at the sample position when the controllability of all PSU had been established. The species with 158 Da might be $^{158}(CrCl_3)$, $^{160}(Fe_2O_3)$, $^{162.5}(FeCl_3)$, or a combination of them.

focussing (section 5.1.3.1). Later, when the problem had been solved, a better mass resolution was obtained, as shown in Fig. 5.2.2, where the percentage is reduced to < 1% and < 6% respectively.

The higher background signal (~10 pA) for the measurement with V_F = +0.018 kV was attributed to a leakage resistance from the variable aperture to the FLIG column which was grounded. The different peak positions of Au_n^- for different V_F should be due to the Wien filter PSU errors (±1.3% at 200 V).

5.2.3 Beam profile and transmission at the variable aperture

An experiment was conducted to check the transmission of the ion beam through the variable aperture, in order to better understand the performance of lens 1. This was done after the stability of all PSUs was established, and thus should reflect the true lens performance. The lens was first tuned to acquire the highest Au_1^- current at the sample Faraday cup through a variable aperture Ø 800 μm, and then the beam profile at the variable aperture was obtained by translating the variable aperture with Ø 100 μm across the beam and measuring the current at the Faraday cup. The acquired profile is shown in Fig. 5.2.3.

The beam is approximately Ø 1.7 mm, and slightly centred to one side of the beam. Compared to the profile of a Duo–FLIG oxygen beam measured in the same place (Smith N S, 1996), the beam is broad and flat-topped. It also appears to be a broad beam cut off by an aperture, which should be the isolation valve (Ø 4 mm; Fig. 3.2.1). Irrespective of this loss, the averaged current is 8.7 (± 0.04) pA per Ø 100 μm. Supposing the beam is uniformly distributed, the total current on the variable aperture is estimated to be 2.51 nA (a beam of Ø 1.7 mm represents 289 holes of Ø100μm, 8.7 pA × 289 ≈ 2.51 nA), and the transmission through the variable aperture with Ø 800 μm should be ~0.56 nA, which is close to the measured value ~0.6 nA. This accounts for a transmission of 24 % and a big loss of 76 %. We later understood that most ions obtained at the sample position were form the 4th and 5th area of the cone (Fig. 4.2.1 (a)) and the lenses used are not optimised for this emission (section 5.2.6). Indeed, the

simulation showed that the lenses used can only form a cross-over of the beam far before the variable aperture.

The other issue of the ion beam was with regard to the possibility that it was hollow as simulated (Chapter 4). Because ions are emitted from the cone surface (off the optic axis), the beam is emitted from a ring-shaped virtual object. However, Fig. 5.2.3 shows that it is actually slightly concentrated in the centre. This can be explained by Fig. 5.4.2 (a). This was verified by another experiment that measured the current at the sample whilst the variable aperture was reduced from Ø 800 μm to Ø 100 μm. The transmitted currents were normalised to that with variable aperture Ø 800 μm. These measured values were then compared to the calculated values, as shown in Table 5.2.1. Note the currents are too small to give rise to significant space charge effects (section 4.2.4).

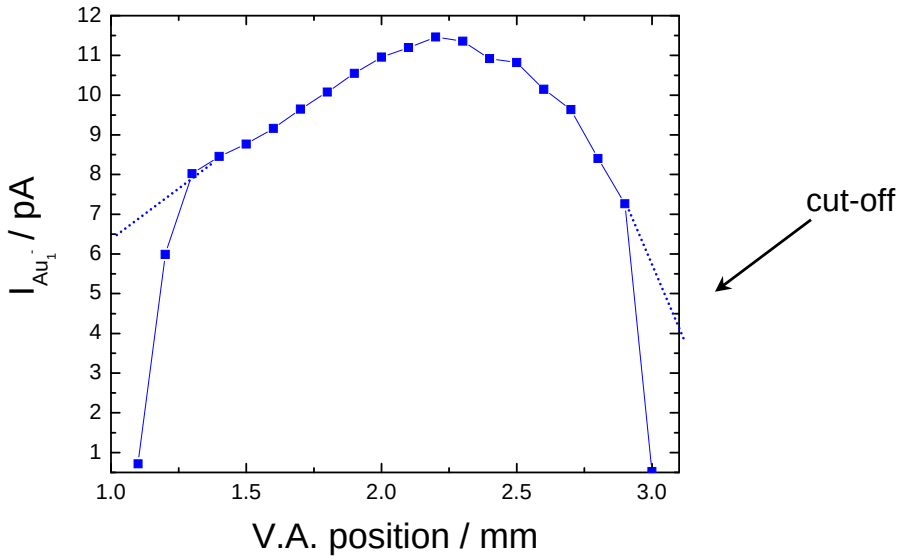

Fig. 5.2.3 The Au_1^- beam profile at the variable aperture position when the lens was tuned to obtain the highest transmission through the variable aperture of Ø 800μm.

Table 5.2.1 The Au_1^- beam transmission through the variable aperture with different sizes

VA diameter / μm (±0.5)	Au_1^- current measured at the Faraday cup / nA (± 3%)	normalised measured values (±0.04-0.4 %)	normalised estimated values (±0.04-0.4%)
800	0.47	100%	100%
300	0.086	18	14
200	0.039	8.3	6.3
100	0.012	2.6	1.6

5.2.4 Spot size and current density

The beam spot size was measured by scanning the beam across a rectangular hole (700 × 700 μm^2) on the sample holder (Fig. 3.1.4), and then measuring the distance between the points when the signal varies between 16%–84% of its peak value (2σ). This estimate is based on the assumption that the beam is approximately Gaussian and the hole edge is straight.

Fig. 5.2.4 shows the profile of a 0.4 nA Au_1^- beam (variable aperture Ø 300 μm) where the current was normalised to the peak value. It was measured to be Ø 56.3 (± 0.04) μm and Ø 62.4 (± 0.04) μm at the two sides of the beam, the difference should be because the beam is not perfectly Gaussian. The other profile which was measured orthogonally was about 70 μm. The elliptical shape is due to the change of the shape of the cone aperture, which was always found to be elliptical after some time of sputtering (Fig. 5.2.6).

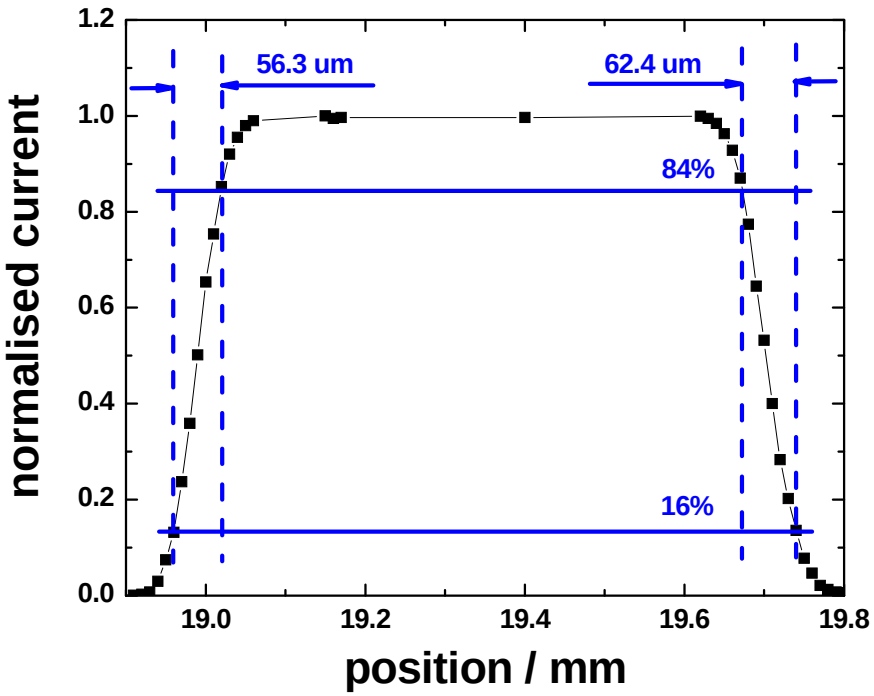

Fig. 5.2.4 An Au_1^- beam profile (normalised) when being scanned across a rectangular hole (700×700 μm^2) for determining the spot size at the sample position. The current was about 0.4 nA.

The demagnification of the beam from the variable aperture to the sample is between 4.3-5.1, which is comparable to the O_2^+ and Cs^+ beams, > 4 and > 3 respectively, through the FLIG column on the commercial Atomika 4500 SIMS instrument (Morris R J H, 2007). The current density was about 12.13 (± 0.004) μA cm^{-2}. However, the maximum current obtainable with a variable aperture Ø 300 μm is ~0.7 nA, and thus the maximum current density is ~21 μA cm^{-2}. This value can be compared to that generated from other caesium sputter gold cluster ion sources: a source was reported to emit a 9 keV Au_1^- beam with a current density 2.4 μA cm^{-2} (Belykh *et al.*, 2000b), and another developed in Duisburg (Germany) can deliver a 5 keV Au_1^- ion beam with a current 100 nA into a spot of Ø 1 mm, which equals a current density of 12.7 μA cm^{-2} (Samartsev A V and Wucher A, 2006). Later on in this work when the new lens was designed and tested (section 5.5), the current density was estimated to be ~38 μA cm^{-2} (1 keV).

5.2.5 Stabilisation and lifetime

Normally, the source requires more than four hours to stabilise, so that the Cs^+ current on the gold cone and thus Au_n^- current at the Faraday cup (or the sample) achieve stability. This means one would have to wait for more than four hours before any precise experiments are allowed. Taking into account the low current of the source, the sputter-based emission and the PSUs used not being computer controlled, at most two experiments can be done in a 8-hour working day. The source is still far from a commercial design. If one wants to take the advantage of running the source one night in advance to get it stabilised, there would still be problems with arcing and current leakage problems (section 5.1.1) and the gold film being quickly exhausted. Once the stabilisation is achieved, the instability of the Au_n^- current at the sample through the FLIG is normally between 1-2% in a period > 0.5 hour.

The lifetime of the source, i.e. between any maintenance or replacement, depends mainly on the sputtering (caesium) current and the gold film thickness. As the source is based on sputtering, ions of any kind can cover parts of the

surface inside the source, particularly the surrounding area of the cone. Insulators, when covered by conductive materials, usually caused PSU potential instability or electrical arcing, and conductors, when covered by insulating materials, may become charged. Should either happen, the beam ceases to be controllable. On the other hand, once the gold film is exhausted due to Cs^+ ion bombardment, the ions detected on the sample may be species other than gold. Fig. 5.2.5 shows the mass spectra obtained when the film had sputtered through in places, where the peak of 179 Da should be due to the addition of $^{197}Au_1^-$ and $^{158}(CrCl_3)^-$, $^{160}(Fe_2O_3)^-$ or $^{162.5}(FeCl_3)^-$ signals. When the source was dismantled and the cone investigated, it was found that the gold film was almost completely gone from the aperture region (Fig. 4.2.1), and the stainless steel was exposed (see Fig. 5.2.6). At the exit area, the cone was covered by insulating materials, which might be iron oxides.

With all the factors taken into account, the lifetime of the source was estimated, in the caesium current and time, to be 1920 μA hrs. This value is equivalent to 40 μA of I_{Cs^+}, or 4 nA of $I_{Au_1^-}$, when the source is optimised, for 2 days continuously.

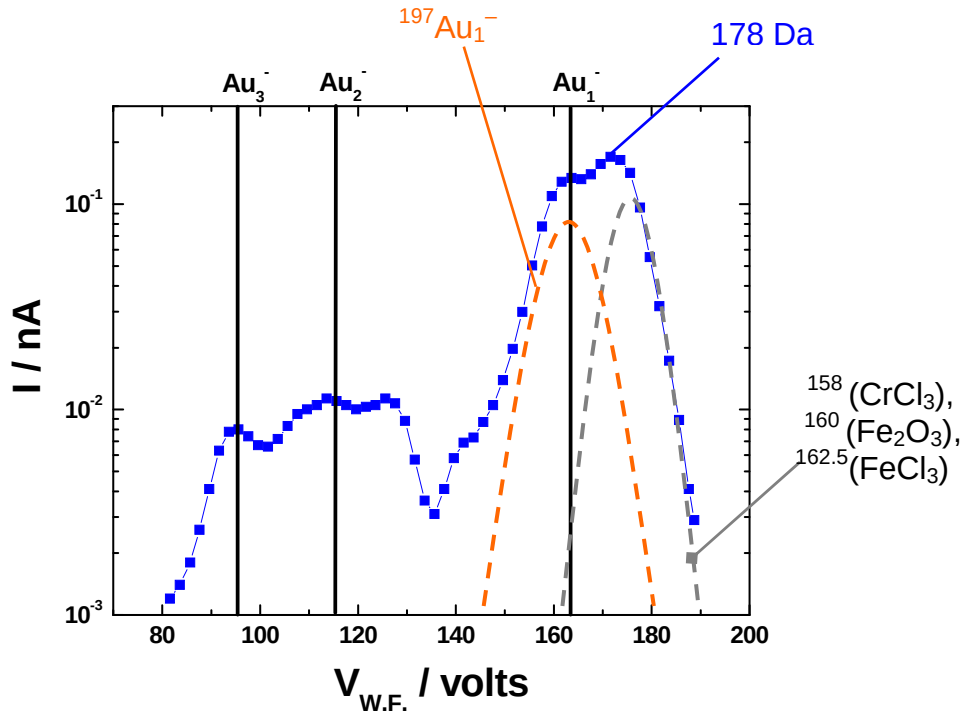

Fig. 5.2.5 A mass spectrum measured at the sample when some parts of the gold film had been exhausted due to sputtering. The peak of 179 Da should be due to the addition of signals of $^{197}Au_1^-$ and $^{158}(CrCl_3)^-$/$^{160}(Fe_2O_3)^-$/ $^{162.5}(FeCl_3)^-$.

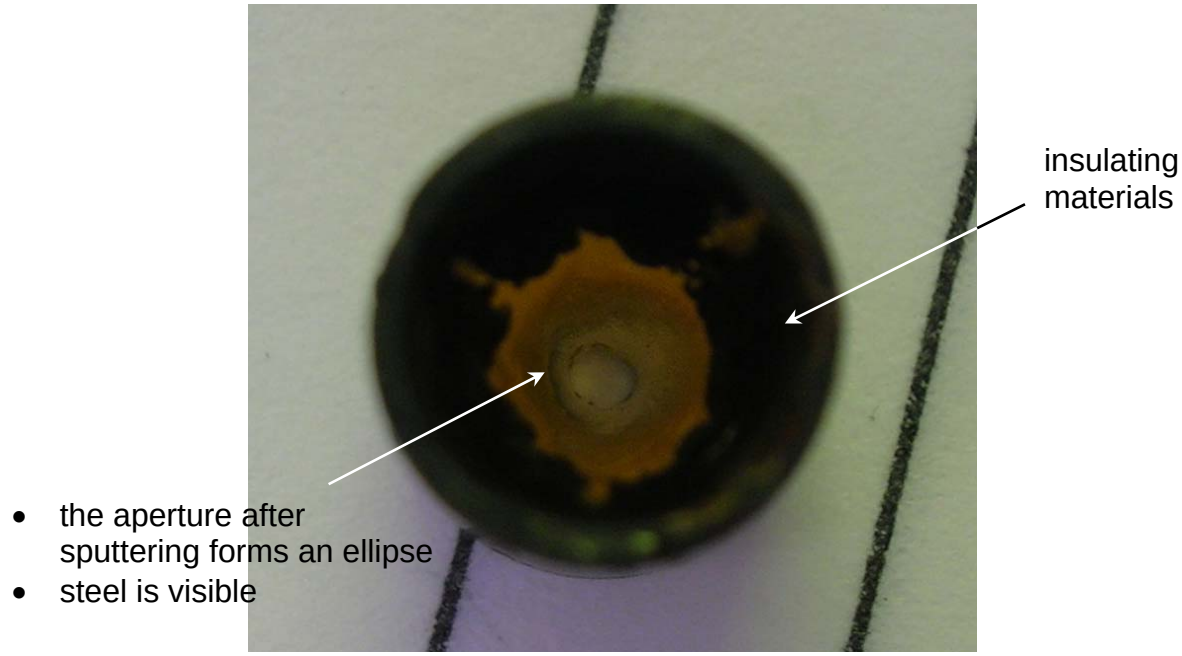

Fig. 5.2.6 Inspection of the cone after observation of impurity ions in the beam. The cone was mainly sputtered at the aperture area, where steel is visible. The entrance area was deposited with insulating materials.

5.2.6 The effective emission area

As can be seen in Fig. 5.2.6, the cone was mainly sputtered at the aperture area when all electrode potentials were tuned to generate highest currents at the sample. It was also found that this optimal set of electrode potentials disagreed with the simulated results (Chapter 4). The experimental potentials were later simulated as shown in Fig. 5.2.7, and it was found that only ions from near the cone aperture could escape, i.e. the 4^{th}-5^{th} area.

This result disapproves the previous expectation (section 4.2.2) that the 3^{rd} area would be responsible for the majority of transmitted ions. It also means that lens 1 needs to be redesigned for best ion transmission from the aperture position. As can be seen in Fig. 5.2.7 (e), the Au_1^- ions from the 5^{th} area, although all passing through the cone aperture, are completely defocussed at the place of the variable aperture. The figures (a) and (b) show Cs^+ ions emitted from 6 points (defined in section 4.2.1) mainly impact the 3^{rd} area, which does not reflect the reality as described above. (c) shows Au_1^- ions emitted from the 1^{st} and 2^{nd} areas cannot

pass the cone aperture but bombard the Cs emitter. Very similar situation happens to (d), which simulates Au_1^- ions emitted from the 3rd and 4th areas.

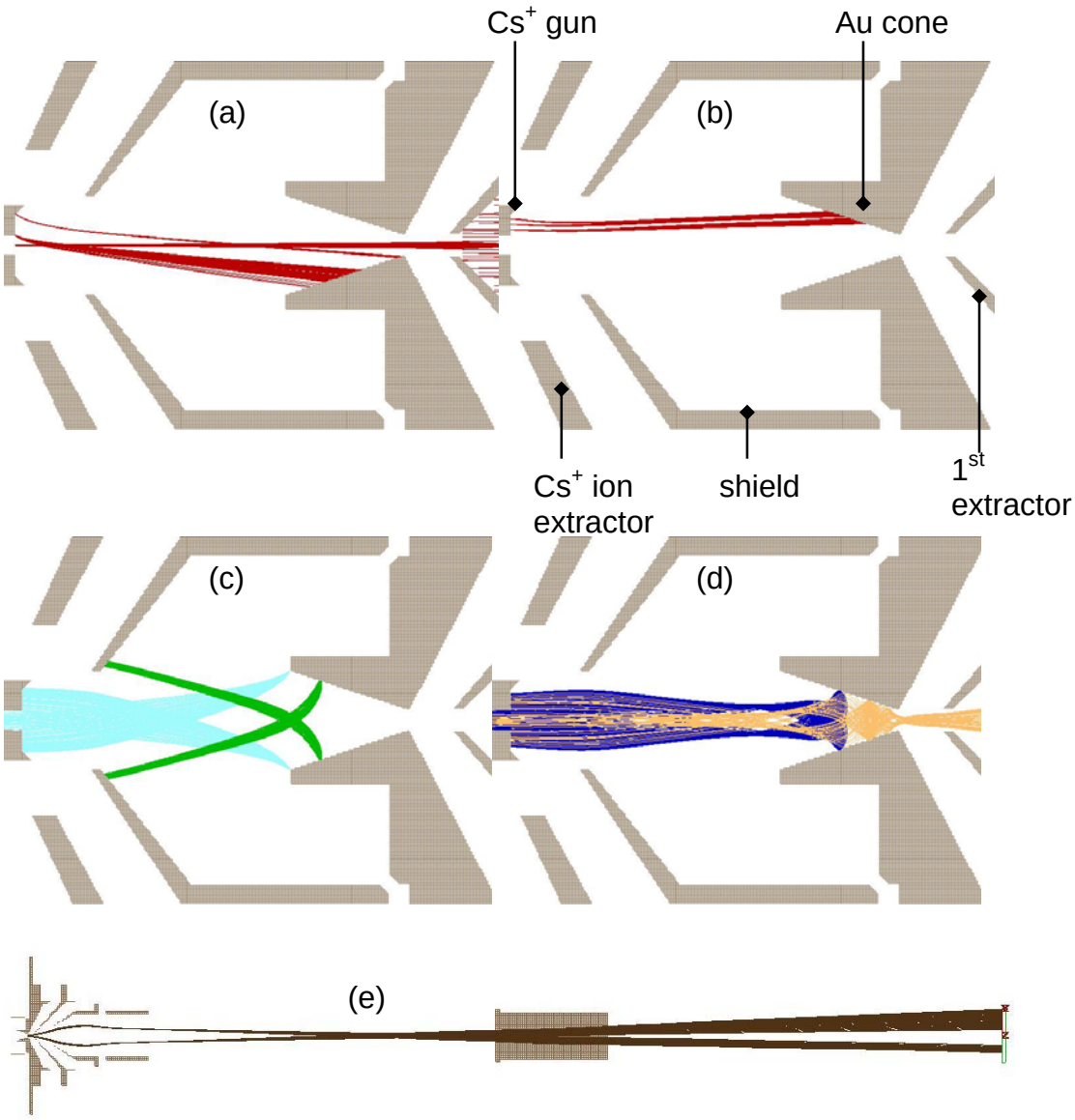

Fig. 5.2.7 The simulation of ion emission when the experimental values of electrical potentials are applied. (a) and (b) show the Cs^+ ions mainly fell on the 3rd area of the cone. (c) and (d) show majority of the gold ions from areas 1st through 4th could not pass through the cone aperture and bombarded the Cs^+ ioniser. (e) shows the gold ions from the 5th area could pass the cone aperture but not the variable aperture of the FLIG.

5.2.7 Gold ion yield ratio v.s. caesium sputter energy

The sputter energy of the gold film by Cs^+ ions, E_{Cs^+}, was tested in the range of 4-6 keV in order to find the highest Au_2^- and Au_3^- yields (1 keV), and the result is shown in Table 5.2.2. This experiment was done when P_F had been improved to 10^{-7} mbar. The ratio of $\frac{I_{Au_1^-}}{I_{Cs^+}}$ was $\sim 8\times10^{-5}$ and changed with the sputter energy in the range of ±5 %.

The ratios of $I_{Au_1^-} : I_{Au_2^-} : I_{Au_3^-}$ deduced from the report by Belykh S F *et al.* (1992) was also presented, although the ratio of $\frac{I_{Au_1^-}}{I_{Cs^+}}$ was not reported at all. In their report, however, it was not specified at which E_{Cs^+} the ratio of 100:3:1 was obtained, but only stated the typical E_{Cs^+} be 2.4 keV. It was thus assumed the ratio does not change much from $E_{Cs^+} = 2.4$ keV to 3 keV, and the ratio be 100:3:1 for $E_{Cs^+} = 3$ keV as shown in Table 5.2.2.

As $\frac{I_{Au_1^-}}{I_{Cs^+}}$ did not change much in the tested range of E_{Cs^+}, the maxima of $I_{Au_3^-}$ and $I_{Au_2^-}$ can be obtained at around $E_{Cs^+} = 5$ keV. Note it was also reported by Belykh *et al.* that $I_{Au_1^-}$ has its maximum at this sputter energy. The difference of results between this work and Belykh's is attributed to the different experimental set-ups, such as sputter angle and the optics of the primary columns.

Table 5.2.2 Au_n^- ion yield ratio v.s. Cs^+ sputter energy ($P_F \sim 10^{-7}$ mbar)

	this work	Belykh *et al.*
sputter energy / keV	$I_{Au_1^-} : I_{Au_2^-} : I_{Au_3^-}$	$I_{Au_1^-} : I_{Au_2^-} : I_{Au_3^-}$
3	N/A	100 : 3 : 1
3.5	N/A	90 : 2.7 : 1
4	18 : 1.3 : 1	88 : 2.6 : 1
4.5	N/A	82 : 2.5 : 1
5	13 : 1.2 : 1	53 : 1.8 : 1
5.5	N/A	64 : 2.1 : 1
6	14 : 1 : 1	N/A

5.2.8 Space charge

As detailed in section 4.2.4, a planar magnetic field should be able to deflect the secondary electrons coming out from the cone aperture. However, the implementation of a planar field would require a major change of the source design as can be seen in Fig. 4.2.7 (c). Based on the assumption that most gold ions and secondary electrons should emit from the 3rd area of the cone, a ring-shaped cylindrical ferrite magnet was purchased instead (Magnet Applications Ltd., ref. No. FE014A-M). A magnetic flux density of 0.03 (±0.004) T was measured in the ring centre. The initial simulation showed that due to the magnetic field created, the electrons emitted from the 3rd area stay in the cone for a longer period and thus can be suppressed by the surrounding electrical field. The trajectories of the gold ions are not influenced.

However, when the magnet was put on to the cone, no increase of gold current at the sample was observed. Since we now have known that most ions, and secondary electrons, are emitted from the cone aperture, this is understandable. Because the electrons emitted from the aperture only spiral about the magnetic field (Fig. 5.2.8), and are still attracted into the FLIG column and participate in the multi-species beam. A planar magnetic field is required in order to deflect

the electrons. As ferrite is nonconductive, charging effects were observed when it was used for the first time without a screen. The magnet was not used subsequently.

Later, when the new emission system was tested (section 5.4), all the electrode potentials were found to be similar to the simulated values (implying the space charge was not pronounced), up to an Au_1^- current of ~9 nA when the Cs^+ current was ~90 μA. If we assume the secondary electron yield (number of electrons sputtered by a primary ion) is 0.1 under the conditions given here (H.S.W. Massey and E.H.S. Burhop, 1952), there would be an electron current of 9 μA coming out of the cone aperture, which alone could have resulted in large space charge according to the simulation in section 4.2.4. This result implies that the gold cluster ions, the secondary electrons and the Cs^+ ions that penetrated through the cone aperture compensated for one another in charge, alleviating the space charge effects.

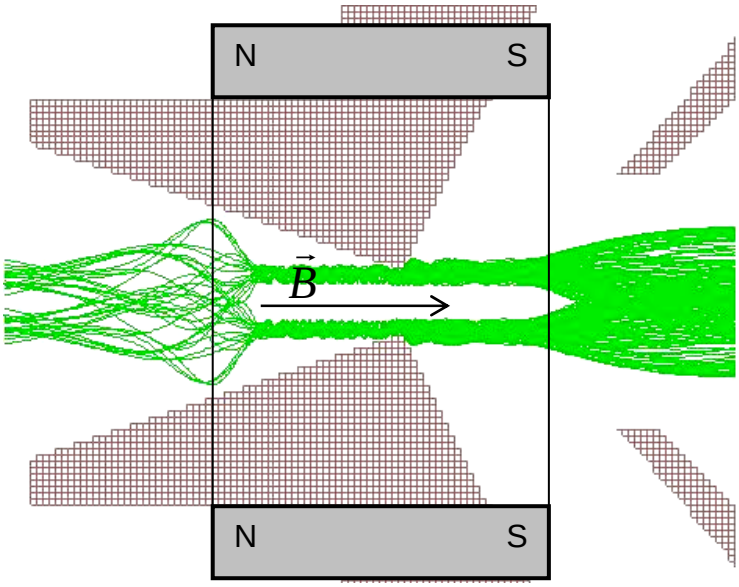

Fig. 5.2.8 Simulation of the spiralling secondary electrons (emitted from the cone aperture) about the magnetic field of 0.03 (±0.004) T. The electrons emitted from this point are still attracted into the FLIG column and participate in the multi-species beam.

5.3 Higher energy and positive ions

The procedure to obtain a gold cluster ion beam with a higher energy (>1 keV) is quite straightforward – all the electrode potentials are to keep the same value with respect to the cone potential, V_c. For example, if when V_c is -1 kV (beam energy 1 keV), V_1 is -0.9 kV and V_F +5 kV, when V_c changes to -3 kV (beam energy 3 keV), V_1 would be -2.9 kV and V_F +3 kV. Nevertheless, there are several things to bear in mind. The potential of L2 (Fig. 3.2.1), V_{L2}, should be always kept at -300% or 75% of the cone potential, e.g. for V_c = -1 kV, V_{L2} = ~ +3 kV or -0.75 kV.

The filament emission status is different when V_c is different. This is because the source chamber is always kept at ground potential but the filament potential has to follow V_c, and thus the electric field surrounding the filaments changes. For energies lower than 1 keV it is worthwhile noting that V_F cannot exceed -1200% of V_c. This is because then L2 cannot focus the beam at a working distance of 40 mm from the exit of L2 (Smith N S, 1996). Thus the difference of 6 kV between V_c and V_F is effectively limited to $V_c \leq$ -0.46 kV. When the value of V_c-V_F needs to be changed in order to obtain lower energy ion beams, V_{WF} should be changed too. The conditions described here also apply to positive mode.

The source was not characterised in detail for the case when the ion beam had an energy exceeding 1 keV. The relative ratios of $I_{Au_1^-} : I_{Au_2^-} : I_{Au_3^-}$ were 30:1.7:1 (±0.08) and 30:1.8:1 (±0.08) for energy of 2.7 and 3.7 keV respectively, and the ratios of $\frac{I_{Au_1^-}}{I_{Cs^+}}$ were 8.2×10^{-5} ($\pm0.4\times10^{-5}$) and 7.9×10^{-5} ($\pm0.4\times10^{-5}$) respectively, when $P_F \sim 10^{-6}$ mbar.

The source was once run in the positive mode, and positive gold cluster ions (Au_n^+) were detected at the sample. To run in this mode, V_F should change from +ve to –ve. The potential on the Cs^+ ioniser and reservoir should still be biased positive with respect to V_c, and the filament potential should still be biased negative with respect to that on the Cs^+ ioniser and reservoir. Due to the

constraints of time, no detailed characterisation was done for this mode unfortunately.

5.4 New emission system

As stated previously in this chapter, the low current density that was obtained with the present design of SCIS-FLIG is one of the main causes that make the study of sputtering and depth profiling time consuming and difficult (section 5.2.5). It is probably the main reason why there have been few publications reporting on depth-profiling using cluster ion sources based on sputtering. Changing the sputter target from a cone to a stick with the caesium beam being focussed to the stick point should enhance the usefulness of both caesium and gold ions (with the current design the caesium ions bombard the area 3^{rd}-5^{th}, but only the aperture (5^{th}) area is useful). However, the limited time we had did not allow for this change. On the other hand, the results of the beam profile on the variable aperture and the study of the effective emission area (sections 5.2.3 and 5.2.6 respectively) imply that a new emission system can be designed to better focus the ions from the aperture area, so as to get a higher current density at the sample.

The old emission system (section 4.3; serving as L1 in SCIS-FLIG) was examined again, taking into consideration that most gold ions come from the 5^{th} area. The analysis is shown in Fig. 5.4.1. Figure (a) shows that according to the initial simulation as described in Chapter 4, a cross-over of Ø 0.86 (± 0.004) mm can be formed at the variable aperture position for ions emitted from the 3^{rd} area of the cone surface. All parameters being the same, ions emitted from the 5^{th} area form a cross-over immediately after L1, after which the beam diverges and has a diameter of 8.76 (± 0.004) mm at the variable aperture position (Fig. 5.4.1 (b)). In this case, the lens error – *coma*, due to off-axis emitted rays having large angles to the optic axis – is also noticeable (Fig. 5.4.1 (c); Klemperer O, 1971).

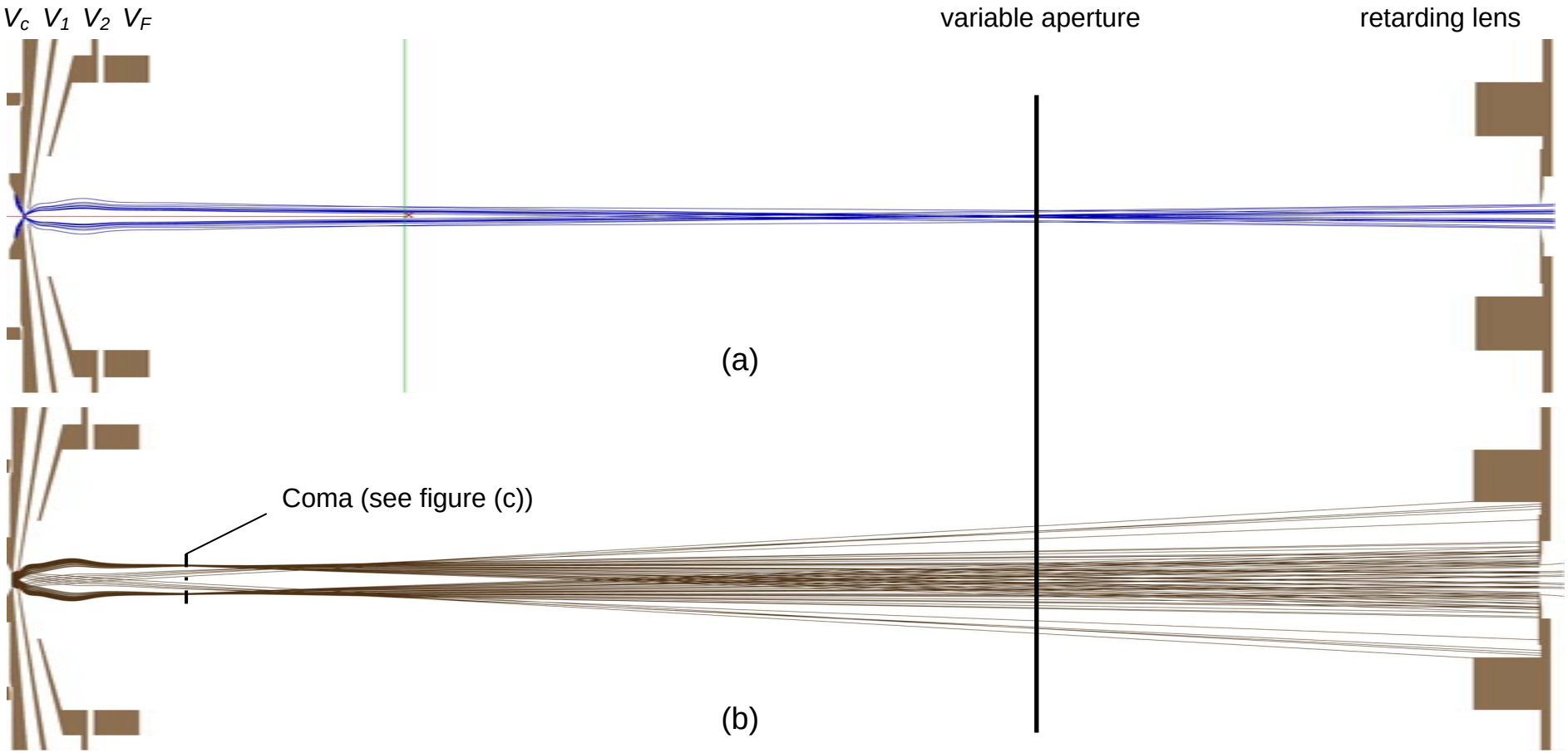

Fig. 5.4.1 The simulations of ion trajectories with the old emission system: (a) emission from the 3rd area, (b) emission from the 5th area. All potentials are optimised to obtain highest ion transmission from the 3rd through the variable aperture. The potentials for V_c, V_1, V_2, V_F are -1, -0.9, -0.14 and + 5kV respectively. The aberration of *Coma* present in (b) is illustrated in figure (c) next page.

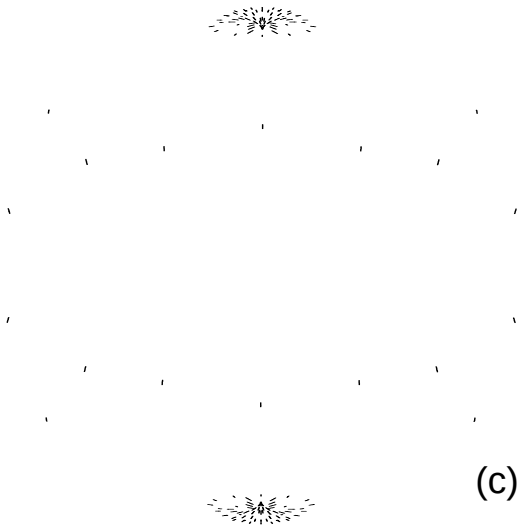

Fig. 5.4.1 (c) The aberration of *coma* present in Fig. 5.4.1 (b).

The parameters of potentials were then optimised for the 5th area emission, and a cross-over of Ø 6 (± 0.04) mm was obtained at the variable aperture, as shown in Fig. 5.4.2 (a). In this case, huge *astigmatism*, another lens error due to off-axis emission, was observed: the images in the $\hat{x}-\hat{y}$ plane and $\hat{x}-\hat{z}$ plane are 40 mm apart.

A new emission system was then designed based upon getting the ions from the 5th area to form a smaller cross-over at the variable aperture, with reduced lens errors. The new emission is composed of the original 1st and 2nd electrodes with an extra electrode (3rd) put before the V_F electrode. Besides this, the whole source was moved 45 mm closer to the variable aperture (Fig. 5.4.2 (b)). The new system works as an immersion lens plus an Einzel lens. As can be seen from the simulation shown in Fig. 5.4.2 (b), a cross-over (also the image) of less than Ø 0.5 mm is formed in between the 1st and 2nd electrodes (the immersion lens), which is projected onto the variable aperture by the Einzel lens formed by the 2nd, 3rd and V_F electrodes. The cross-over formed at the variable aperture is Ø 3 (± 0.04) mm. The astigmatism is reduced; the two images formed in the $\hat{x}-\hat{y}$ and $\hat{x}-\hat{z}$ planes before the variable aperture are 20 mm apart. No noticeable coma can be observed.

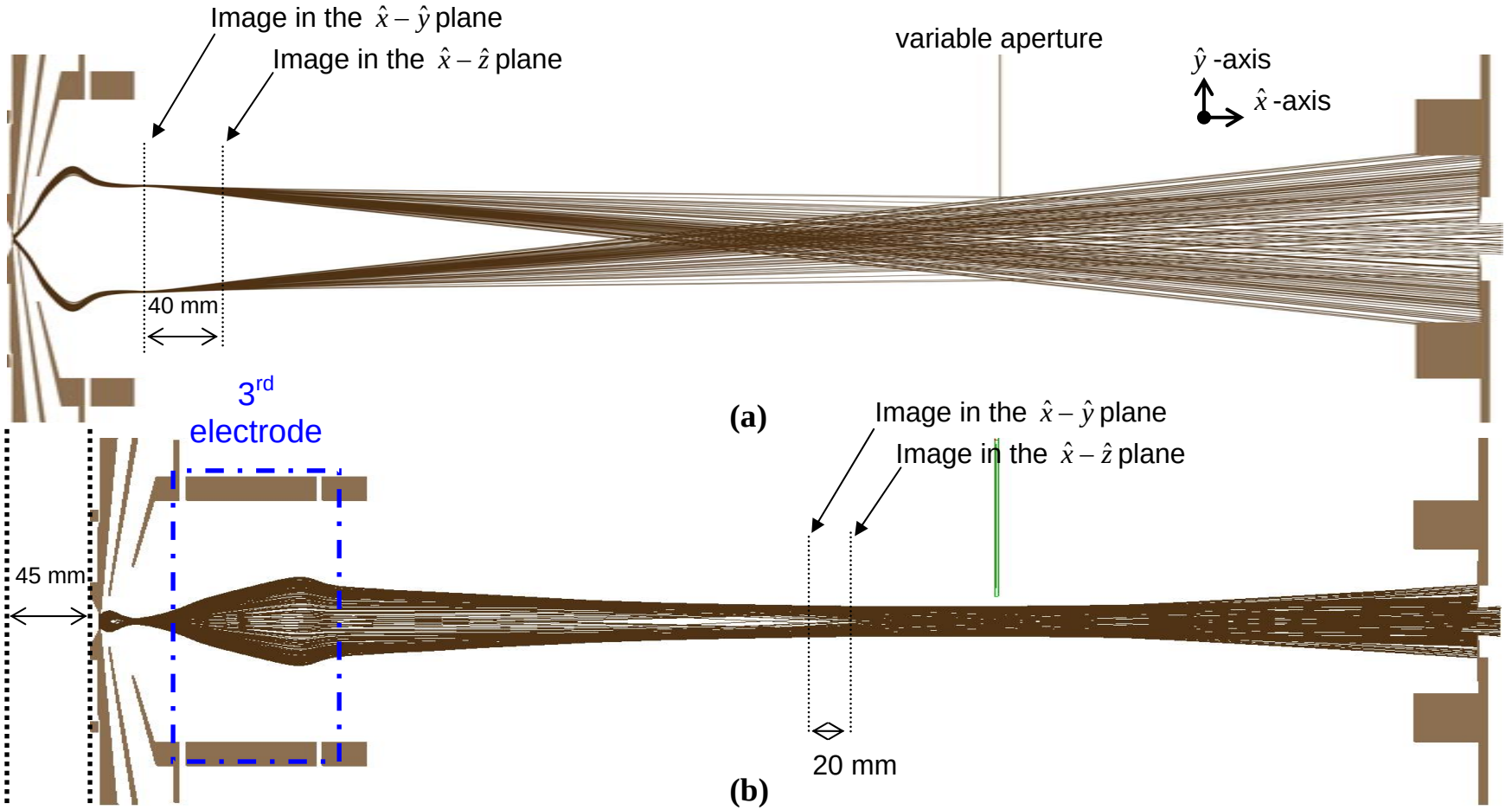

Fig. 5.4.2 The simulations of ion trajectories from the 5th area, when all potentials are optimised to obtain highest ion transmission through the variable aperture. (a) old emission system, (b) new emission system. The potentials for V_1 and V_2 are +2 and -0.13 kV respectively for the old, and -0.9 and +5 kV for the new with V_3 = +0.6 kV. V_c and V_F remain the same values as in Fig. 5.4.1.

105

The new system was built as shown in Fig. 5.4.3. It was found to be able to generate an Au_1^- current up to ~9 nA which had been limited to ~5 nA with the old system. The spot size at the sample was similar to that with the old system. The ratio of $\frac{I_{Au_1^-}}{I_{Cs^+}}$ was increased from $\sim 8\times10^{-5}$ ($\pm0.4\times10^{-5}$) to $\sim 1.2\times10^{-4}$ ($\pm0.4\times10^{-5}$) whilst that of $I_{Au_1^-} : I_{Au_2^-} : I_{Au_3^-}$ remained constant. Fig. 5.4.4 shows the orthographic projection of the source equipped with the new emission system (drawn in Alibre Design®).

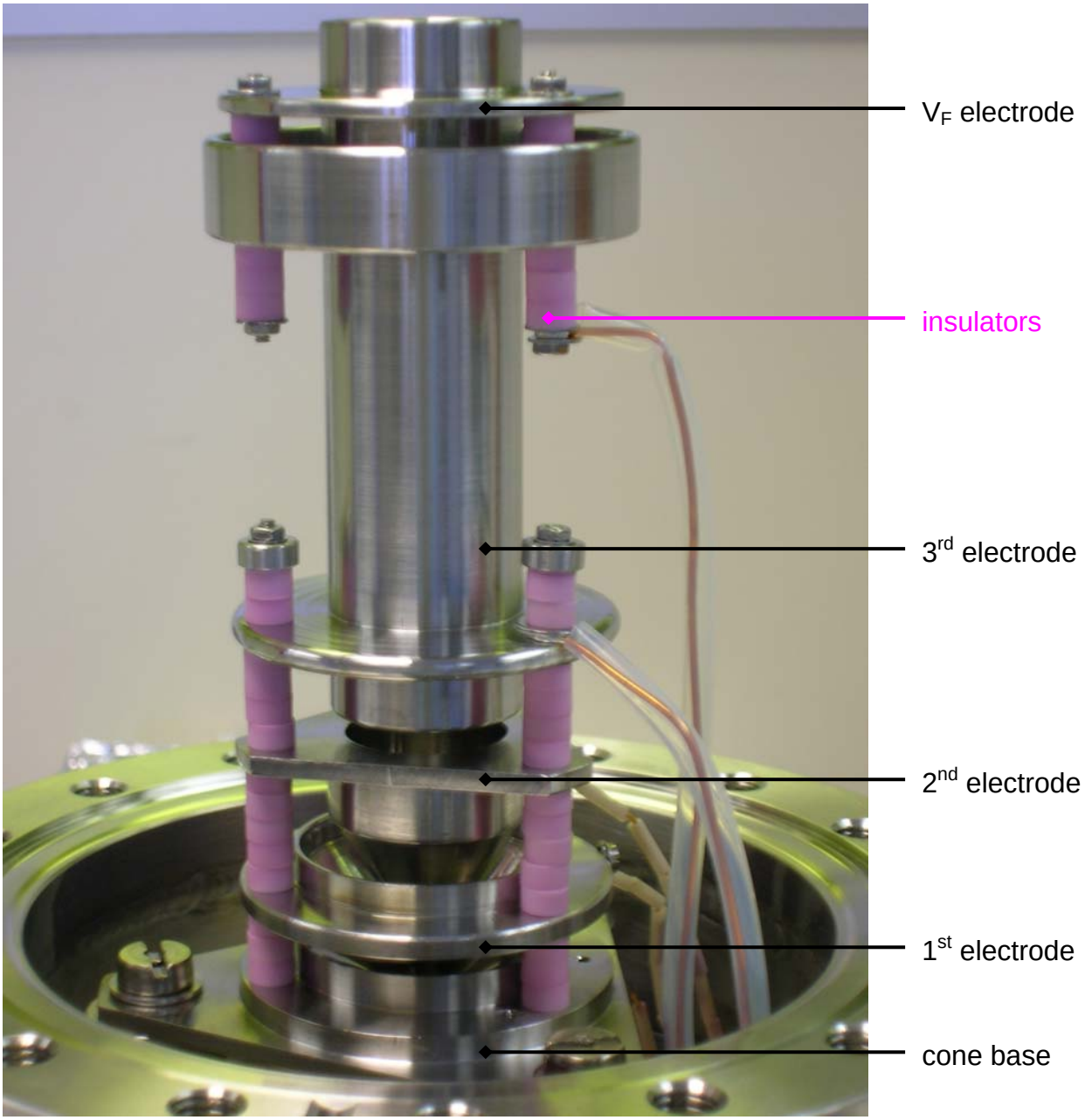

Fig. 5.4.3 The new emission system as built with the extra (3rd) electrode. The pink ceramics are used for electrical insulation.

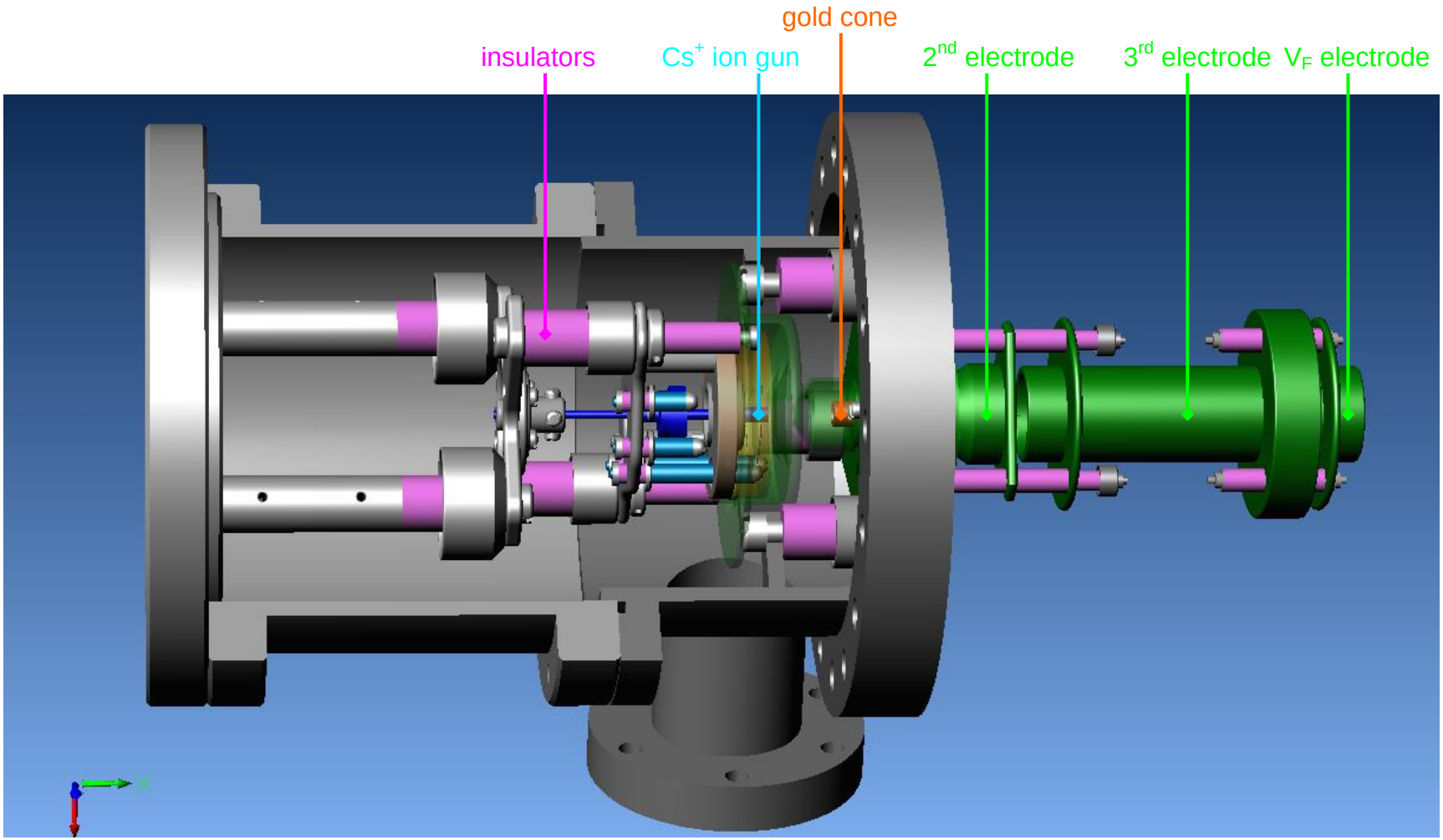

Fig. 5.4.4 Orthographic projection of the SCIS equipped with the new emission system. The pink area is insulators.

Chapter 6 Gold Ion Bombardment

One objective of this work is to investigate the usefulness of gold cluster ions for SIMS depth profiling applications, in terms of sputter rate and producing surfaces with low surface roughness. Silicon was chosen because it is a major material used in microelectronics, and therefore a frequent candidate for SIMS. The study was conducted with an impact energy in the ultra low energy range, namely ≤ 1 keV per constituent Au atom of any ion. The results of sputtering were compared with O_2^+ and Cs^+ ions, the most commonly employed species in this field. Deposition of gold on the sample was found in the cases with a low dose of gold. An interesting phenomenon was found in that some bombarded surfaces changed from crater to '*hill*', and the cause was examined by the (X-ray) energy dispersive spectrometer (EDS) technique. The roughness of bombarded surfaces was studied by atomic force microscopy (AFM).

6.1 Experimental

A float zone silicon sample (5-20 mΩ cm, antimony doped) was used through out the study.

The ion impact energy range was 0.33-3 keV, giving E_0 = 0.11-1 keV (E_0 defined in section 2.2.1). The impact angle, θ, was 0^o and 45^o, and dose in the range of 0.15-2×10^{17} Au atoms cm^{-2}. The pressure was about 5×10^{-8} to 2×10^{-7} mbar in the SCIS-FLIG chamber and 2-5×10^{-9} mbar in the sample analysis chamber.

The depth of bombarded craters was measured using mechanical stylus profilometry (Dektak 3030, Sloan Technology Division, Veeco Instruments, Inc.). Because the craters were elliptical (section 5.2.4), each was measured in two directions (three times to establish the error) corresponding to the $\hat{x}$ and $\hat{y}$ axes of the sample manipulator (section 3.1). The bombarded surface was imaged by scanning electron microscopy (SEM) (ZEISS SUPRA 55VP), which is equipped

with an X-ray energy dispersive spectrometer (EDS) for chemical imaging (Goodhew P J *et al*, 2001).

The sputtered volume of each crater was approximated by an elliptical cylinder with its axes equivalent to the full width half maxima (FWHM) of its Dektak depth profiles, and its length the depth of the crater. The sputter rate, *S*, was thus obtained by dividing the number of silicon atoms sputtered from a crater by the number of incident ions,

$$S = \frac{\pi ab \times d \times D(Si)}{M(Si) \times I \times t / e}, \qquad \text{(Eqn. 6.1.1)}$$

where, *a* and *b* are the radii of the corresponding ellipse, *d* the depth, *D(Si)* the density of silicon, *M(Si)* the atomic mass of silicon, *I* the ion beam current, *t* the bombardment time and *e* the charge on an electron. The error in the sputter rate calculation was established by

$$err(S) = \frac{(1 + \%err(a)) \times (1 + \%err(b)) \times (1 + \%err(d))}{(1 - \%err(I))} - 1, \qquad \text{(Eqn. 6.1.2)}$$

where, %*err*(*x*) representes the percentage error of any parameter *x*.

An atomic force microscope (Veeco Escope) was used in this work for surface roughness study. The data were taken by Dr Neil Wilson.

6.2 Gold deposition and bombarded crater evolution

A study of how dose affects sputtering or deposition for different ion species was initiated. However, due to the large errors (up to 36% at E_0 = 0.33 keV) in the depth measurement of shallow craters (≤ 10 nm) by Dektak, coupled with the low current density of the cluster ion beams imposing long time for bombardment, this study was not complete. Indeed, many bombarded craters with low dose were discarded because their depths were within the Dektak error range (1-2 nm). Nevertheless, the experiments that have been accomplished still provided some insights.

The results are shown in Table 6.2.1. For E_0 = 0.33 keV, a dose of 1×10^{17} cm^{-2} is enough for Au_1^- and Au_2^- to create craters. For Au_3^- a dose of

$\leq 0.539\times10^{17}$ cm^{-2} resulted in gold deposition. For E_0 = 0.5-1 keV, with the dose used of 0.8-2$\times10^{17}$ cm^{-2}, deposition was not observed. Most craters were found to have their edges raised by up to 1-2 nm immediately after having been removed from the ultra high vacuum (UHV), which may indicate deposition of gold in these low dose regions. It was found in the literature that, at E_0 = 30 keV, Au^+ deposited on silicon with dose < 2×10^{15} cm^{-2} (Döbeli M *et al.*, 1997; section 2.2).

Table 6.2.1 Depth measurement of the bombarded surfaces, with various E_0, ion species and the time for which the bombarded sample was under atmospheric pressure before being depth measured. Red coloured values were measured to be above the original surface level. **(a)** and **(b)** relates to Fig. 6.2.1, and **(c)** and **(d)** to Fig. 6.2.2.

E_0 / keV (±0.005)	ion	dose / 10^{17} atom cm^{-2}	1st depth / nm	time after having left UHV	2nd depth / nm	time after having left UHV
-0.33	Au_1^-	0.986±17%	-6.625±17%	1-5hrs	8~10	~31 hrs
-0.33	Au_2^-	1.036±14%	-6.5±9.7%	1-5hrs	**(d)** hill	~31 hrs
-0.33	Au_3^-	0.426	10~12	1-5hrs		
-0.33	Au_3^-	0.539	10	1-5hrs		
-0.33	Au_3^-	2.06±17%	-18 ~ -22 ±14%	1-5hrs		
-0.5	Au_1^-	0.999±13%	**(a)** -11±5.7%	1-5hrs	**(b)** 0 with edges ~5	~31 hrs
-0.5	Au_2^-	2.145±4%	-20 ~ -25 ±14%	1-5hrs	-18~-20 with edges 10~15	~16 days
-0.5	Au_3^-	1.058 ±7.5%	-14 ~ -19 ±6.8%	1-5hrs	-15~-17 with edges ~10	~1 day
-1	Au_1^-	0.954±6%	-18±9.5%	1-5hrs	-16 ~ -20	~42 days
-1	Au_2^-	0.823±14%	-19.67±2.6%	1-5hrs	**(c)** -19~-22.5	~31 hrs
-1	Au_3^-	1.461±11%	-45 ~ -55 ±4.6%	1-5hrs	-50	~1 day

A peculiar observation which has not been reported in the literature is the time dependent evolution of the bombarded silicon surface by gold ions. Some craters were found to change to '*hills*' after some time under atmospheric pressure. On those craters that were found to have raised edges immediately after having been removed from UHV, the edges were also found to become bigger in time. Fig. 6.2.1 (a) is the profilometer measurement from a crater

bombarded by 0.5 keV Au_1^- with dose 1×10^{17} cm^{-2} when the crater had been in air for one hour, and (b) for 31 hours. In about 30 hours the crater bottom had risen up ~10 nm and the edges 5 nm.

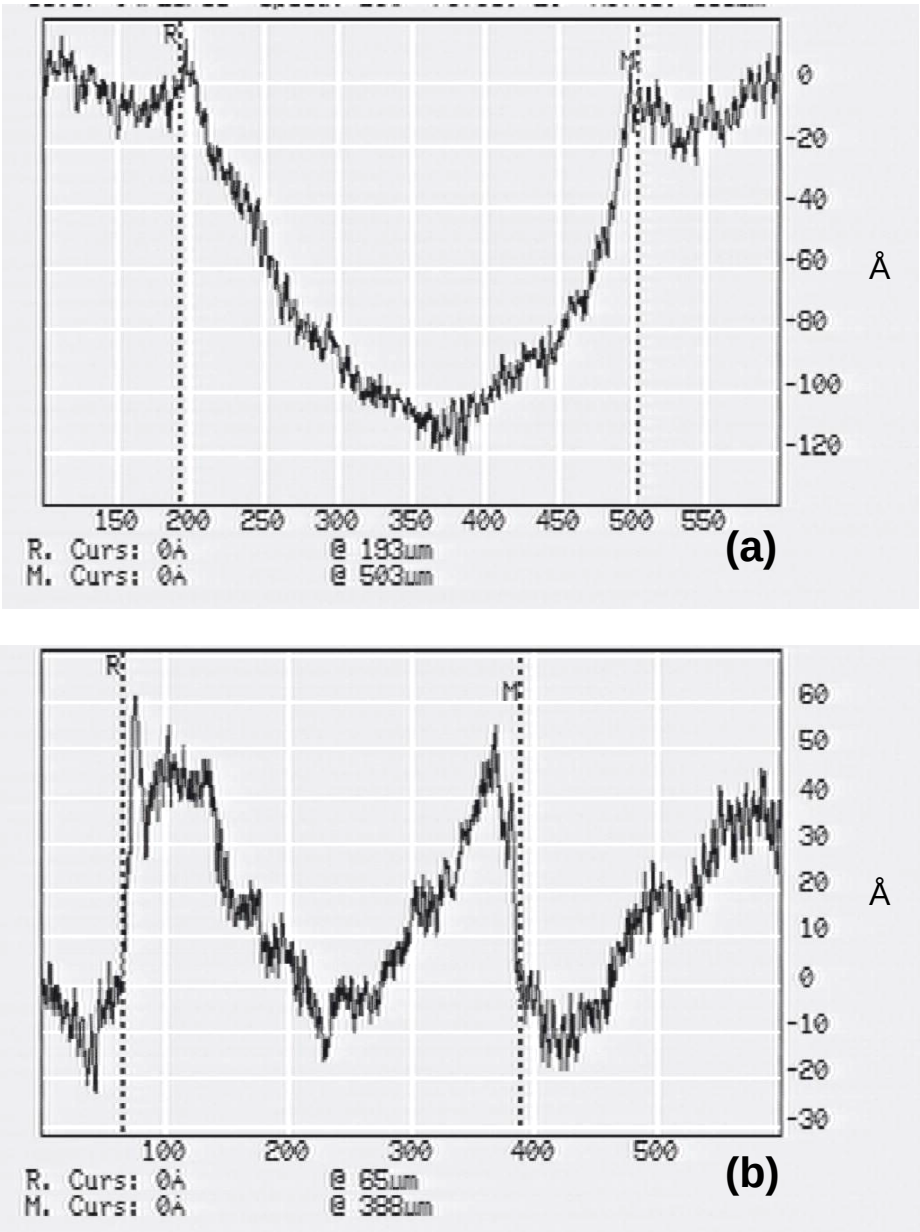

Fig. 6.2.1 The depth profiles of a crater formed by 0.5 keV Au_1^- impact (dose 1×10^{17} cm^{-2}), measured within one hour under atmospheric pressure (a) and after 31 hours (b).

This phenomenon is suspected to be due to the porous structure formed under the surface after the gold ion bombardment, and the generation of broken silicon bonds. Oxygen thus more readily penetrated into such regions forming

silicon dioxide, resulting in the rise of the bombarded surface. When silicon atoms are converted to silicon dioxide there is a volume increase of approximately a factor of 2.

Two craters were then chosen and the abundance of silicon, oxygen and gold was measured at the centre of each crater by EDS. One, impacted by $E_0 = 1$ keV Au_2^- (dose ~0.8×10^{17} cm^{-2}), remained a crater (Fig. 6.2.2(c)). Another, impacted by $E_0 = 0.33$ keV Au_2^- (dose ~1×10^{17} cm^{-2}), changed to a hill after 31 hours under atmospheric pressure (Fig. 6.2.2(d)). From the figures, it is seen clearly that the abundance of oxygen in (d) is more than the original surface.

Overall, with the limited obtained data, this phenomenon that crater shape evolves with time is both energy and dose related. The lower the energy and dose, the more probable it is that the crater changes shape. This also makes reproducible experiments difficult, as all the samples would need to be measured or analysed immediately after removal from the vacuum; exposure of the sample under atmospheric pressure leads to errors hard to estimate.

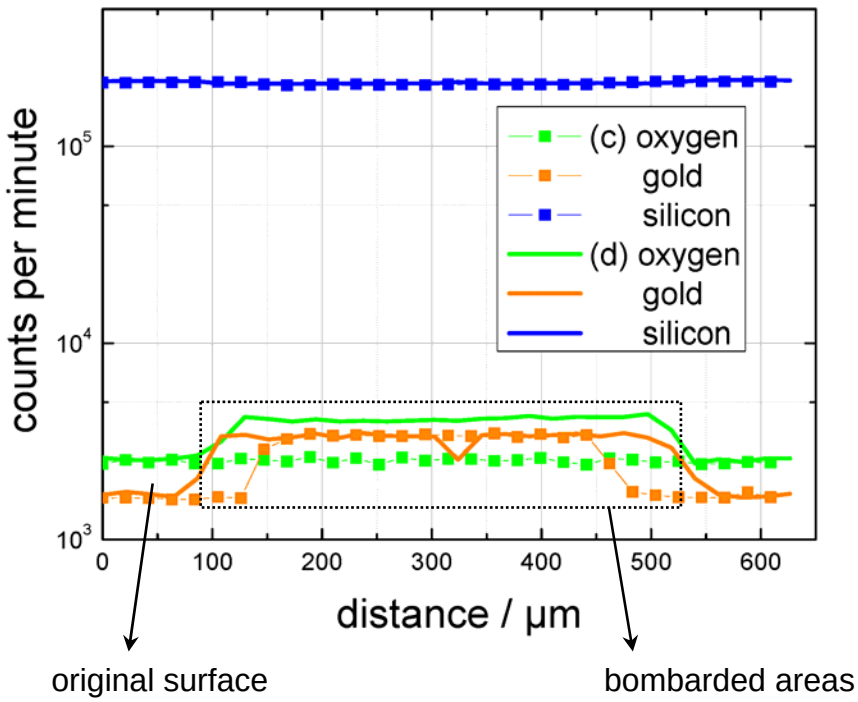

Fig. 6.2.2 EDS measurement of the abundance of oxygen, gold and silicon around the craters bombarded by Au_2^- ions with conditions of (c) $E_0 = 1$ keV, dose 0.8×10^{17} cm^{-2} and (d) $E_0 = 0.33$ keV, dose 1×10^{17} cm^{-2}.

6.3 Nonlinear sputtering by ultra-low energy Au_n^- ions

Apart from the oxygen cluster (dimer) ions, O_2^+, which have been widely used in the SIMS depth profiling, SF_5^+ ions has also been proved to sputter silicon in the ultra low energy range (Iltgen *et al.*, 1997). This was developed for the dual-beam system on a TOF SIMS instrument. In this work, gold monomer, dimer and trimer ions were observed to sputter the silicon sample in the ultra low energy range, with a dose > 0.8×10^{17} Au atoms cm^{-2}. The sputter rates of Au_n^- (n = 1-3) ions are shown in Table 6.3.1 below, together with the data of O_2^+, Cs^+ ions for comparison. The sputter rates are given as Si atoms sputtered per Au_n^- (n = 1-3) ion.

In general, sputtering silicon by gold cluster ions is more efficient than O_2^+ and Cs^+ ions. For example, at $E_0 = 0.33$ keV, an Au_3^- ion (total energy 1 keV) is equivalent to 9 O_2^+ ions (total energy 0.66 keV) and 4.5 Cs^+ ions, or at the same total energy 1 keV, an Au_3^- ion is equivalent to 7.4 O_2^+ ions and 2.2 Cs^+ ions. This means the primary beam current density and current (if the spot size is fixed) can be reduced to erode the sample to a certain depth.

Here I report the first observation of nonlinear sputtering in the ultra low energy range as discovered in this work. The nonlinear factors, K_n (section 2.2.1), are listed in Table 6.3.1. Fig. 6.3.1 shows the sputter rates given in Si atoms sputtered per constituent Au atom in any Au_n^- ion, with error bars. That K_2 at $E_0 = 0.33$ keV is lower than unity is explained by the measurement errors in the surface profilometer. A molecular dynamics simulation indicated that K_2 is about 7 with $E_0 = 1.5$ keV, $\theta = 45^o$ (Medvedeva M *et al*, 2003; section 2.2.3). In another work using an Au_n^+ LMIS, $K_2 = 1.08$ and $K_3 = 1.23$ with $E_0 = 10$ keV were reported (Döbeli M *et al*, 1997; section 2.2.3). Based upon the available data, K of $Au_n^{\pm} \rightarrow$Si increases with E_0 from 0.33 keV onwards until some point before 10 keV, at which it starts to decrease.

Table 6.3.1 The sputter rates of silicon by Au_n^- (n = 1-3), O_2^+ and Cs^+ ions, and the enhancement factors of Au_n^- ions, in the range $E_0 \leq 1$ keV (normal incidence) †R. Gibbons' software

ion species	Au_1^-	Au_2^-	Au_3^-	K_2 (±0.004)	K_3 (±0.004)	O_2^+ † (±0.004)	Cs^+ † (±0.004)
E_0							
1 keV	0.951 ±15.75%	2.39 18.4%	5.23 ±17.6%	1.26	1.83	0.38	0.63
0.5 keV	0.533 ±18.92%	1.15 ±18.25%	2.20 ±14.43%	1.07	1.37	0.185	0.414
0.33 keV	0.336 ±35.98%	0.627 ±25.67%	1.37 ±32.36%	0.934	1.36	0.15	0.307

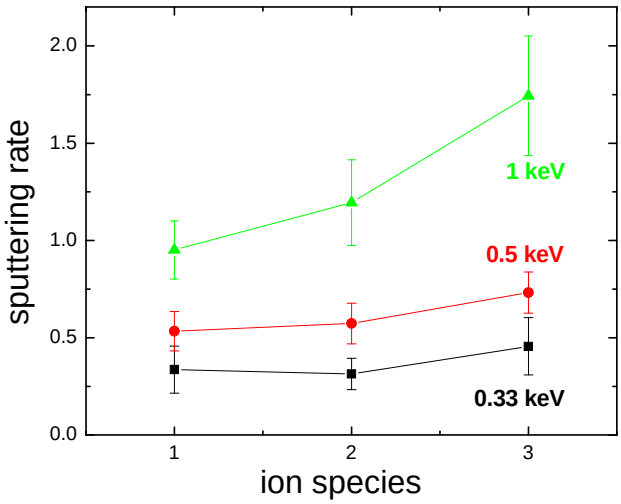

Fig. 6.3.1 Sputter rate of each Au atom in any Au_n^- (n = 1-3) ion, with E_0 = 0.33-1 keV.

6.4 Surface topography

The surface roughness at the bottom of sputtered craters is a key factor in determining SIMS depth resolution, as the rougher the surface the more superposition of signals from different layers, and thus the worse the resolution. A further problem is that developing roughness leads to unstable ion yields through changes in sputter rate and ionisation probability. Silicon samples were bombarded by Au_1^- and Au_3^- ions with a total impact energy of 1 keV, $\theta = 0^o$ and

45°, and one crater was raster scanned (375×540 μm^2). Surface roughness was measured by AFM by Dr Neil Wilson.

Table 6.4.1 gives the conditions and results of AFM. This experiment was conducted before the dose experiments (section 6.2), and thus the effect of dose was not considered in this experiment. The bombarded surface (a) was measured by Dektak to be a hill, (c) a crater, and (b) and (d) unknown because they fell into the Dektak error region. All of them were measured within 6 hours after removed from UHV. AFM pictures are shown in Fig. 6.4.1. Note the original surface (un-bombarded) has an inherent roughness of 0.15 nm.

Unfortunately the data gathered so far do not allow for comparative study between Au_1^- and Au_3^- ions. It is, however, expected that in this ultra low energy regime, for a given E_0, the roughness due to Au_3^- impact should be better than Au_1^- if the dose is high enough for sputtering to happen. Otherwise, the advantage of nonlinear sputtering by Au_3^- (and Au_2^-) may be compromised, hindering its prospect in SIMS depth profiling applications. Obviously, further work is required to establish the usefulness of gold cluster ion in this field.

Table. 6.4.1 AFM study of surface roughness after the radiations of Au_1^- and Au_3^- ions.

	ion	E_0 / keV	θ / degrees	dose / Au atom 10^{17} cm^{-2} (±2.4 %)	scan	roughness / nm (rms) (±4.4%)	sputtering / deposition
(a)	Au_3^-	0.33	0	0.518	No	4.5	deposition
(b)	Au_3^-	0.33	45	0.15	No	2.1	unknown
(c)	Au_1^-	1	0	1.7	No	0.9	sputtering
(d)	Au_1^-	1	0	0.28	Yes	0.15	unknown

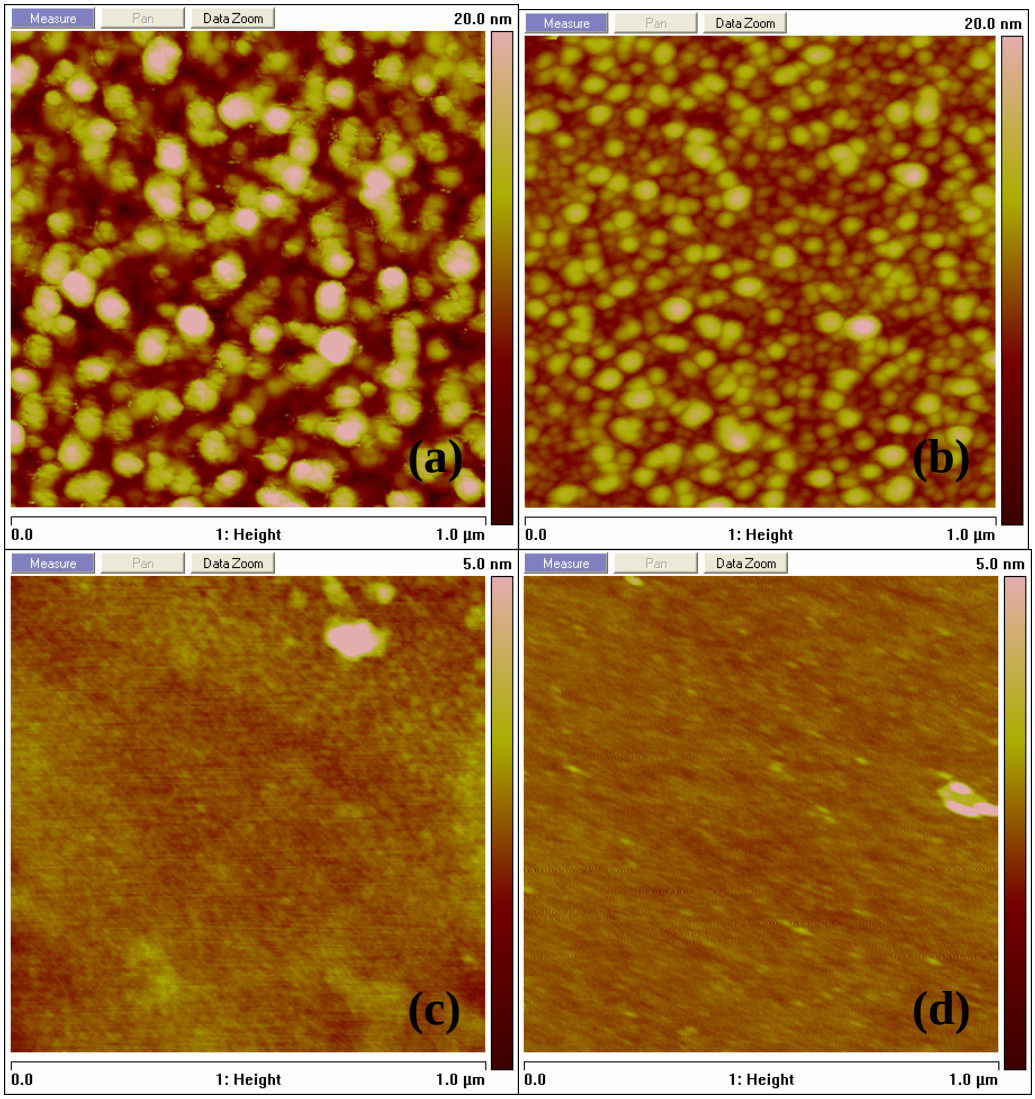

Fig. 6.4.1 AFM pictures of surfaces bombarded by Au_3^- ions (a) and (b), and by Au_1^- ions (c) and (d). The latitude shows the dimension, and the longitude shows the surface level (refer to Table. 6.4.1 for detailed conditions of bombardment).

Chapter 7 Conclusions and Further Work

7.1 Conclusions

To retrofit the sputter gold cluster ion source on the floating low energy ion gun in order to obtain ultra low energy cluster ion beams at the sample, the simulations of ion trajectories (both Au_1^- and Cs^+) were carried out. According to the simulations, an additional ion optical electrode, vacuum engineering, a new Wien filter and electrical scheme, etc. were designed and built.

The SCIS-FLIG was then tested and ultra low energy gold cluster ion beams have been obtained for the first time. Defects were found and improved, which include issues of electrode insulation, vacuum leakage and power supply unreliability. Most of the ions in the beam are found to come from close to the cone aperture (5th area as defined in section 4.2.1). Therefore, a new emission system was designed to enhance the transmission of ions from the region through the FLIG column. As the result, the source now can emit a maximum 1 keV Au_1^- current of 9 nA and current density of 38 μA cm^{-2}, which is superior to any other reported negative gold cluster ions source. The ratio of $I_{Au_1^-} : I_{Au_2^-} : I_{Au_3^-}$ is about 13:1.2:1, and the lifetime of the source is 192 nA hrs (1 keV Au_1^-). Ion beams with higher (3.7 keV) and lower energies (0.33 keV) can be achieved. Positive ions (Au_n^+) were also obtained.

The usefulness of the ultra low energy gold cluster ion beams for SIMS depth profiling has been investigated with a silicon sample. The sputter rates of the ions are higher than that of the most commonly used ions, i.e. O_2^+ and Cs^+. Nonlinear sputtering with $E_0 \leq 1$ keV has been discovered for the first time. Gold deposition due to Au_3^- bombardment ($E_0 = 0.33$ keV) was observed at dose $\leq 0.54\times10^{17}$ cm^{-2}, otherwise sputtering was found with dose $\geq 1\times10^{17}$ cm^{-2}. A peculiar observation is the time dependent evolution of the bombarded silicon surface under atmospheric pressure. The surface roughness has been studied using AFM. However, the latter two studies could not be completed, because of the low Au_n^- current density imposing long bombarding time, and the source

insulators being too quickly covered by sputtered materials, which results in frequent source maintenance.

7.2 Further improvements for the SCIS

In this section we suggest further improvements for the sputter cluster ion source, and preliminary designs and simulations are presented. The first part discusses the improvements to be made for the current source, which are minor changes. As the second part, new designs in terms of electrode geometries and emission systems are described.

7.2.1 For the current design

As has been discussed in Chapter 5, the main causes that result in the unreliability of the source are coated insulators and the caesium gun filaments. Each will be discussed in details and possible solutions be recommended.

7.2.1.1 Insulators

Because the source is based on sputtering, coating of the inside surfaces is unavoidable. The problem observed most often was insulators covered by a metal film, which leads to electrical unreliability. This problem is particularly serious at the insulators in between cone base-1st electrode, cone base-shield and ioniser filament-reservoir filament (through the plate on which the filament supports stand (Fig. 5.1.2 (b)).

The principle of the improvement is to prolong the routes that the sputtered materials access the insulators, either by inventing additional paths or putting the insulators further from the sources of sputtered materials. A suggestion is given in Fig. 7.2.1, in which insulators are placed further from lens apertures where ions emerge. Additionally, this arrangement makes the alignment of lens electrodes easier and better.

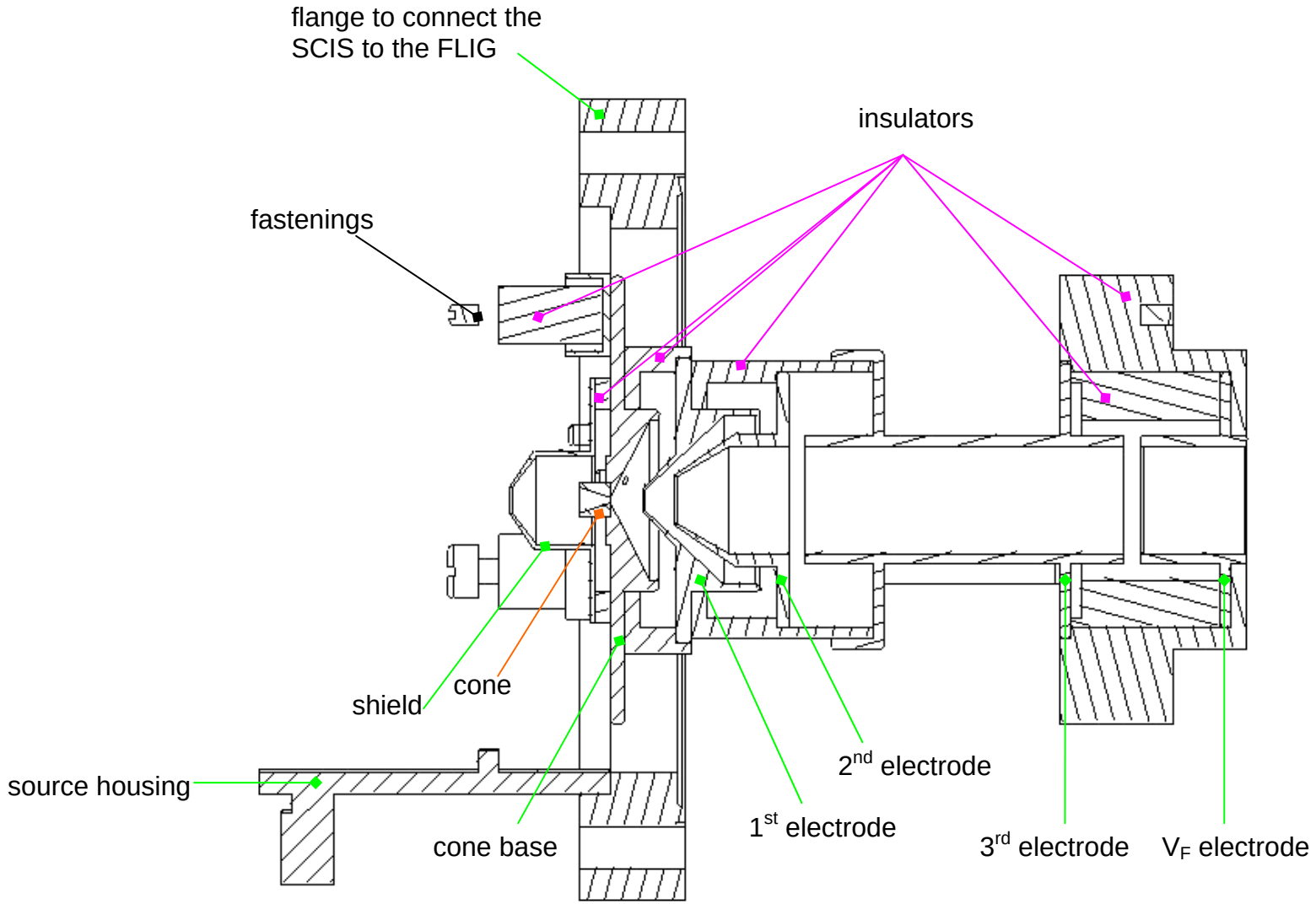

Fig. 7.2.1 Suggested design of insulators: compared to Fig. 3.3.1 and Fig. 5.4.3, insulators are placed further from lens apertures where ions emerge. Additionally, this arrangement makes the alignment of lens electrodes easier and better.

To improve the insulation between the two filaments, an easy way is to replace the filament supports (presently made of tantalum) by insulators, as shown in Fig. 7.2.2 (compared with Fig. 5.1.2). The insulating property of the insulators is further enhanced by putting threads on the surface. Another solution can be conceived based on the same principle as is shown in Fig. 7.2.1.

Other insulators of the source, although long-lived, can be re-designed for longer operation time and higher reliability of the source.

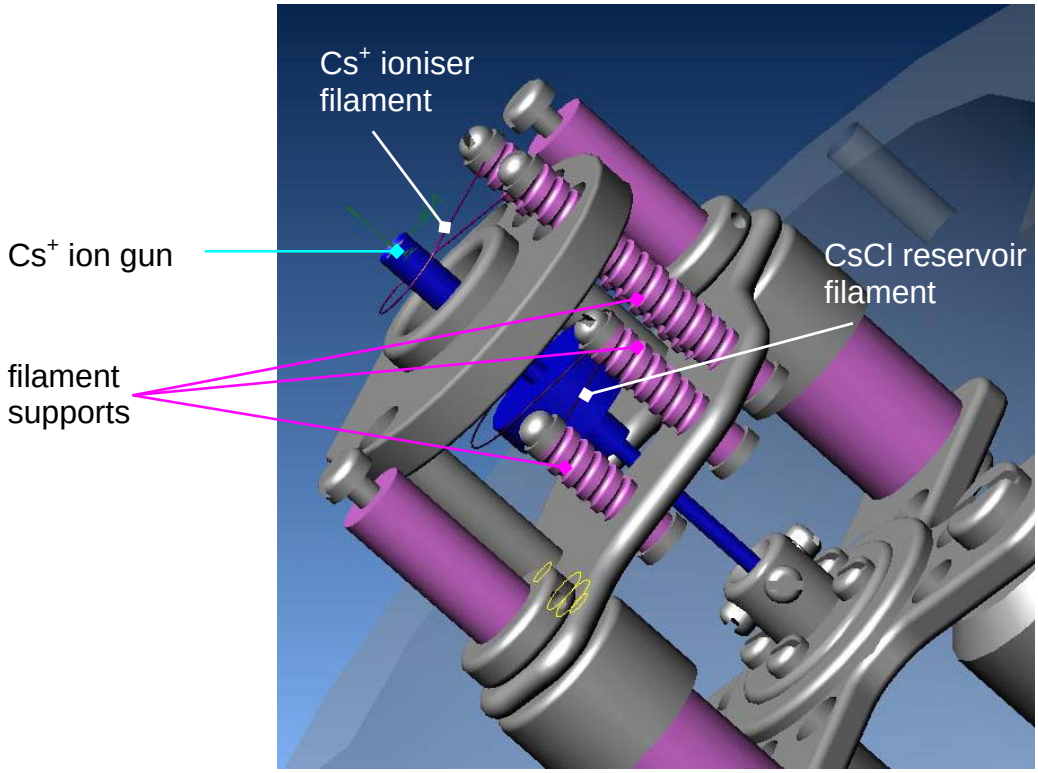

Fig. 7.2.2 The filament supports are replaced by ceramics such as alumina to obtain better insulation between the two filaments. The insulating property of the insulators is further enhanced by putting threads on the surface

7.2.1.2 Filaments

As addressed in section 5.1.2, the current design of the caesium gun heating system has the problem that the ioniser filament can short to its surrounding electrodes, and that the potential of the caesium gun extractor is subject to the ioniser filament electron emission. In addition, because the

filament potential changes with the cone potential (so as to maintain the same potential differences between Cs^+ gun and cone, and between Cs^+ gun and filaments) and the source chamber is always electrically grounded, the electron emission changes (so does Cs^+ current) with cone potential. This makes an instant change of cone potential with a constant Cs^+ current impossible.

A design of three supports combined with a planar shield electrode is a solution. Another is to change the heating system completely to a conduction type, where the filaments are always covered and fixed.

7.2.2 New source

The main disadvantage of the present source design is that neither the Cs^+ ions nor the Au_n^- (n = 1-3) ions contribute effectively to the gold current through the FLIG column and thus at the sample: the Cs^+ ions bombard more than half of the cone surface as indicated by the simulation and practical observation (section 5.2.6), but only the ions emitted from the cone aperture area can pass through the cone aperture. The other disadvantage is that, due to the shape of the gold target, Au_n^- ions are emitted from points off the optic axis. Ions emitted from this ring-shaped object suffer off-axis aberrations, such as astigmatism (section 5.4), which results in ion losses through the FLIG column. These two issues should be taken into account for a new source design in order to obtain a higher Au_n^- current density at the sample.

Two new designs are conceived and presented here. One is to reverse the cone so that the cone aperture faces the caesium gun, whilst the other is to change the cone to a rod to obtain a small circular source.

7.2.2.1 Reversed cone

In principle, this idea is to get gold ions attracted into the FLIG column, instead of being suppressed (due to high electric field) on the cone, re-sputtering the opposite cone surface (inadequate extraction field) and attacking the Cs^+ ioniser. At the same time Cs^+ ions need to be reflected to bombard the cone

surface with minimum loss, as well as an extraction system to get Au_n^- ions behaving such as emerging from a single object on the axis having least aberration.

A preliminary design of reversed cone emission system was simulated, and ion trajectories were shown in Fig. 7.2.3. The Cs^+ ion trajectories are displayed in Fig. 7.2.4. The definitions of Au_n^- and Cs^+ ions are identical to that in section 4.2.1.

As the surface where Au_n^- ions are emitted faces the extraction field, most ions can escape into the FLIG column, instead of being suppressed by the "shield" or attracted to the caesium gun as is in the present design. Nevertheless, since ions still emit from off-axis points (0.5-2.5 mm apart from the axis) and not from the same point on the optic axis, a large cross-over is formed at the variable aperture, and astigmatism was observed. Shown in Fig. 7.2.3 (a), the ions emitted from the 1st point (as defined in Chapter 4) form a cross-over of Ø 4 mm at the variable aperture. With identical parameters of electrical potentials, (c) shows that ions emitted from a point 1.5 mm apart from the 1st point form a cross-over at 167 mm upper-stream from the variable aperture, and the beam waist of this emission at the variable aperture is Ø 10 mm. The astigmatism due to off-axis emission can be observed by comparing Fig. 7.2.3 (a) and (b), which show the ion trajectories in two planes orthogonal to each other (i.e. $\hat{x}-\hat{y}$ and $\hat{x}-\hat{z}$ planes): the object is imaged at a distance of 236 mm from the variable aperture in the $\hat{x}-\hat{y}$ plane, but in the $\hat{x}-\hat{z}$ plane the image is formed 13 mm closer to the variable aperture. Overall, although ions are no more constrained by an aperture, altogether they form a beam subject to off-axis aberrations.

For the Cs^+ ion emission, Fig. 7.2.4 (a), (b) and (c) display that ions emitted from different areas are deflected to bombard different places of the cone. The figures also show that the Cs^+ ions can bombard electrodes other than the gold cone.

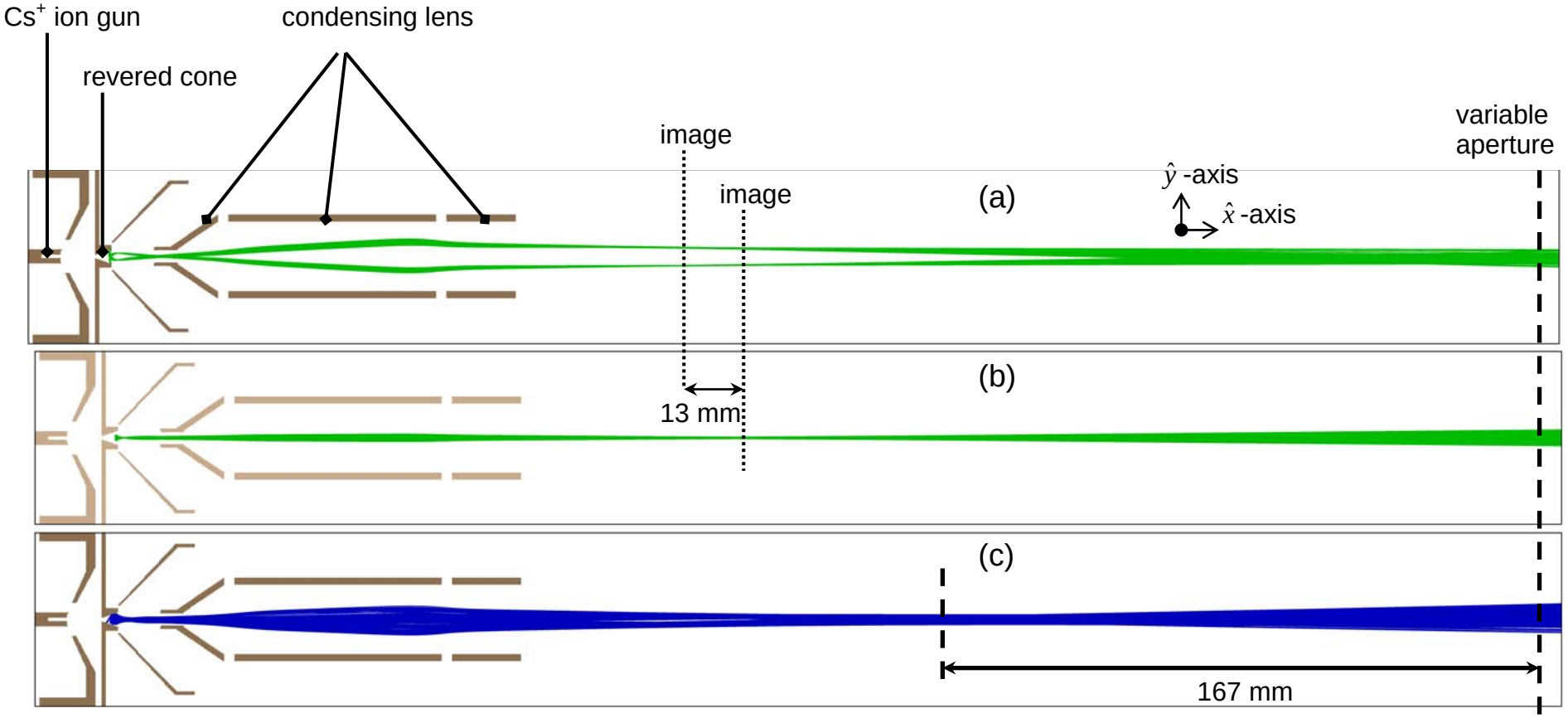

Fig. 7.2.3 The design of a reversed-cone emission system, and the simulation of Au_1^- ion trajectories. (a) and (b) show the trajectories of ion emitted from the *exit* point in $\hat{x}-\hat{y}$ and $\hat{x}-\hat{z}$ plane respectively: images are formed at different places in different planes. (c) shows the trajectories of ions emitted from the point 1.5 mm apart from the *exit* point: a cross-over is formed at upper-stream of the variable aperture.

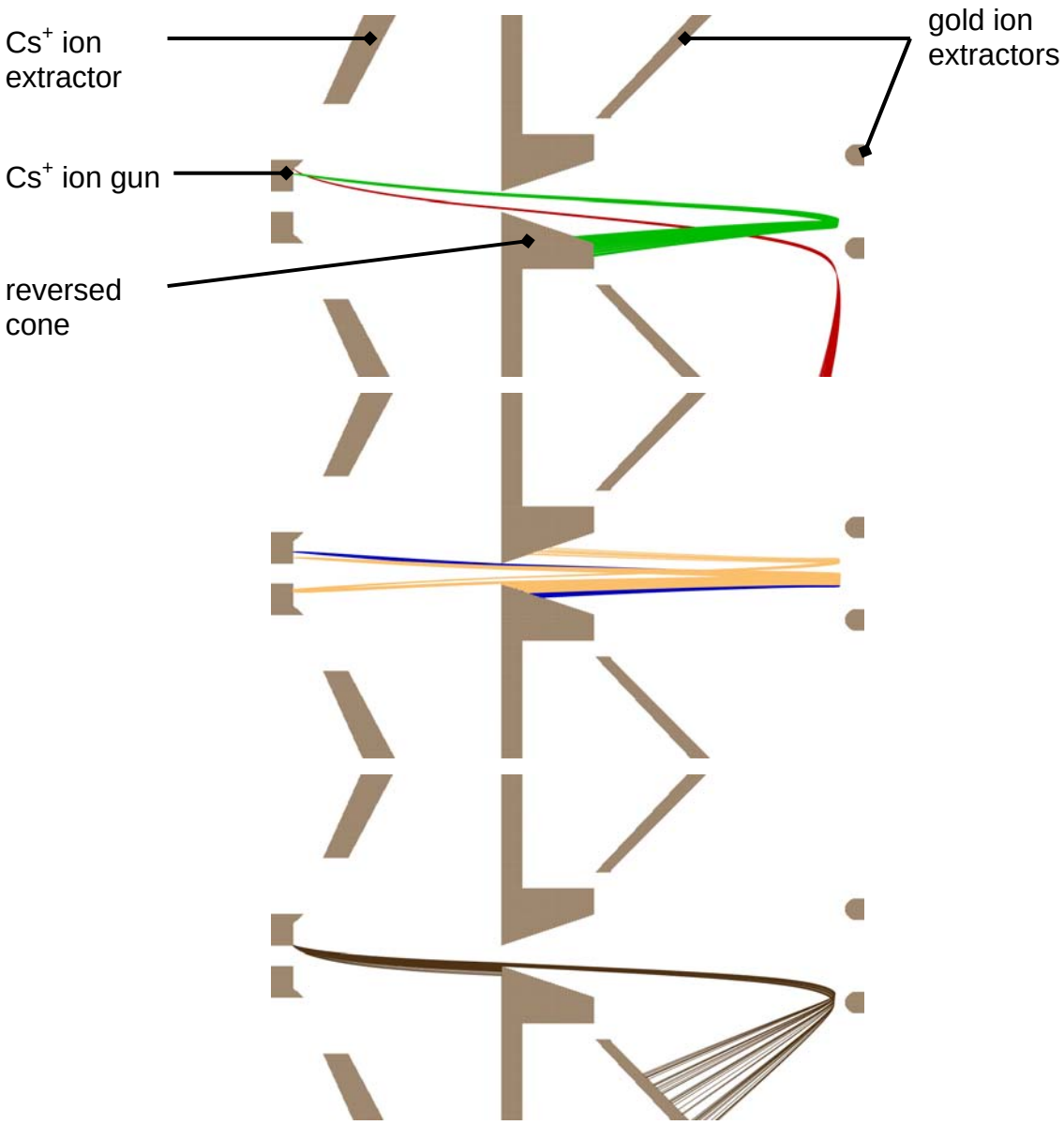

Fig. 7.2.4 The simulation of Cs^+ ion trajectories: ions emitted from different areas are deflected to bombard different places of the cone, they can also bombard electrodes other than the gold cone.

Conclusively, this reversed-cone design still suffers the problems of aberrations and large losses of both Cs^+ and Au_n^- ions, unless the Cs^+ ions can be controlled to bombard a certain region on the cone or a better extraction can be designed to get Au_n^- ions imaged at the same point.

7.2.2.2 Gold rod

There are several advantages of a gold rod design. (i) The object, ion-optics-wise, is a small disc on axis, instead of a ring, which reduces off-axis aberrations. (ii) The object can be made as small as the practical limit in focussing the caesium beam. (iii) Gold and caesium ions will not be wasted as is in the cone design. (iv) The gold rod can be designed to be movable, so that the sputtered tip will be replaced by shifting the rod; the source will not need to be dismantled as frequently.

A preliminary design of emission system for the rod source is presented in Fig. 7.2.5. This simulates 1 keV Au_1^- emission, and the Cs^+ ions bombard the rod tip with an energy of 6 keV. The lens 1 used for the duoplasmatron on EVA 2000 and Atomika 4500 is employed (Fig. 3.2.1). Eighty one caesium rays emitted from an area of Ø 500 μm with an initial angle of 90 ^{o} to the surface and an initial energy of 0.1 eV, are focussed to a spot of Ø 300 μm or less at the gold rod. The gold (Au_1^-) ions are emitted with an initial angle of 90 ^{o} and energy of 1 eV, they emit from an area of Ø 500 μm and can be focussed to the variable aperture where the beam waist is about Ø 40 μm (note: here the distance between the rod and the variable aperture is kept the same). After the variable aperture, the Au_1^- beam is focussed at the sample with a spot size of about Ø 20 μm.
However, if space charge effects are taken into consideration, the designed caesium emission system, with the provided potential parameters, can only emit 0.1 μA. If more current were to be emitted, some ions would stop at the extractor aperture. Again, SIMION cannot simulate space charge properly, and the simulation done here is only provided as a qualitative reference. Fig. 7.2.5(b1) and (b2) show the cases without and with space charge effects respectively. On the other hand, space charge effects should not affect the Au_1^- beam as severely, because the current is much smaller (10^{-4} of the Cs^+ current), provided secondary electrons can be removed. Assuming a maximum Au_1^- current of 50 nA is achieved and the space charge effects are taken into account, the beam will be focussed at the variable aperture and sample with a size of about Ø 200 μm and Ø 70 μm respectively.

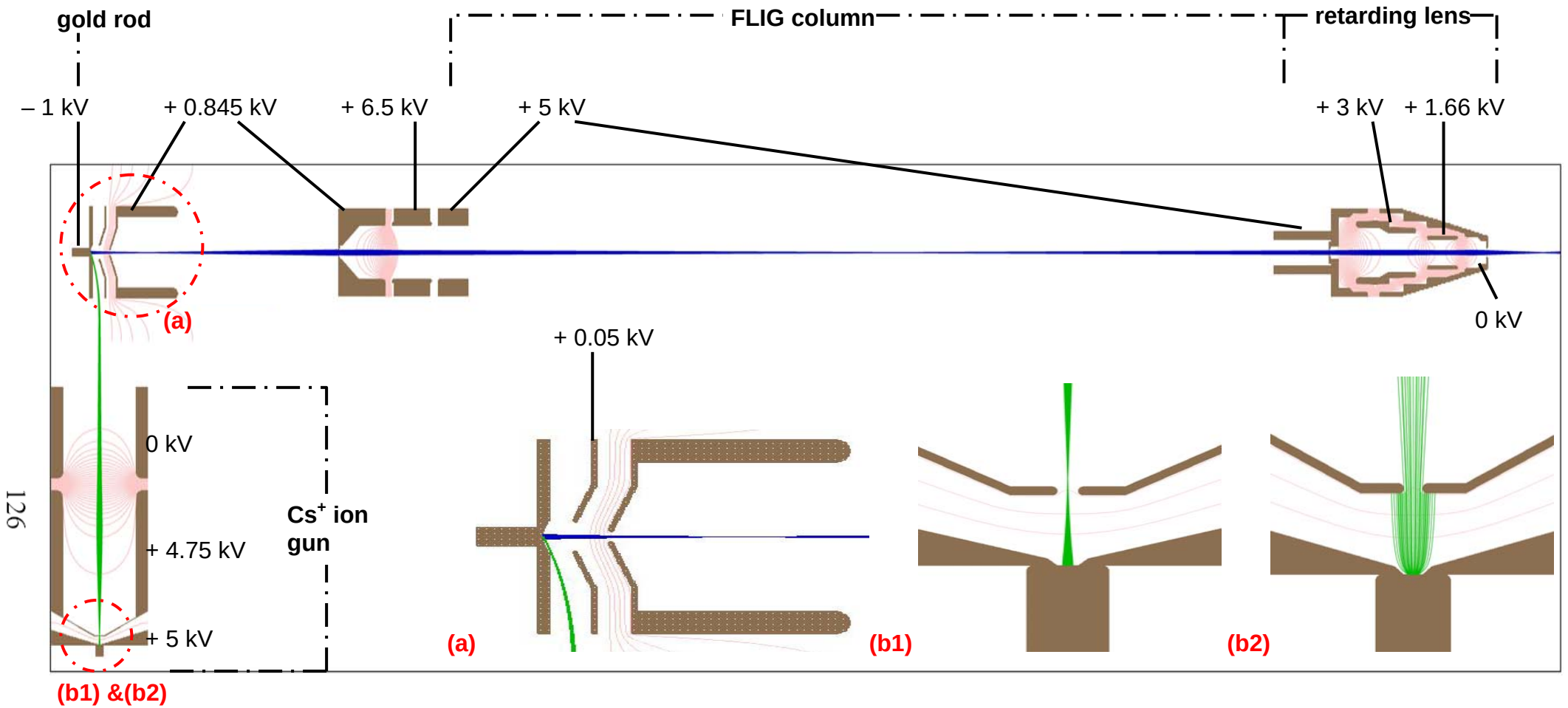

Fig. 7.2.5 The design of a gold-rod SCIS. The green rays denote the Cs^+ ions, and the blue the Au_n^- ions. Inset (a) shows the Au_n^- ion emission system, (b1) shows the emission of a Cs^+ current of 0.1 μA, and (b2) of 0.2 μA where space charge effects make some ions stop at the extractor aperture. (SIMION cannot simulate space charge properly; there is no way of relating the current to any "*real*" current.)

Overall, the main issue that needs to be considered for such a design is the space charge effects that may occur for the caesium ion beam, which influences the caesium current density falling on the gold rod. The caesium ions which do not fall on the rod tip will not only be a loss, but also lead to the problems of caesium coverage on insulators and undesirable sputtering.

Reference

Alton G D, *Rev. Sci. Instum.* **59(7)** (1988) 1039.

Andersen H H and Bay H L, *J. Appl. Phys.* **45** (1974) 953.

Andersen H H and Bay H L, *J. Appl. Phys.* **46** (1975) 2416.

Appelhans A D and Delmore J E, *Anal. Chem.* **61** (1989) 1087.

Barlow R D, Dowsett M G, Fox H S, Kubiak R A A and Newstead S M, *Nucl. Instr. and Meth. in Phys. Res.* **B72** (1992) 442.

Billen James H, *IEEE Transactions on Nuclear Science*, **NS-28** (1981) No. 2.

Belykh S F, Evtukhov R N, Lysenko Ju N and Rasulev U Kh, *Rev. Sci. Instrum.* **63(4)** (1992) 2458.

Belykh S F, Development of a negative cluster ion source for mass spectrometry of secondary ions and secondary neutrals. NATO SfP Project No. 97.1929 (1997)

Belykh S F, Bitensky I S, Mullajanov D and Rasulev U Kh, *Nucl. Instr. and Meth. in Phys. Res.* **B129** (1997) 451.

Belykh S F, Rasulev U Kh, Samartsev A V and Veryovkin I V, *Nucl. Instr. and Meth. in Phys. Res.* **B136** (1998) 773.

Belykh S F, Habets B, Rasulev U Kh, Samartsev A V, Stroev L V and Veryovkin I V, *Nucl. Instr. And Meth. in Phys. Res.* **B164-165** (2000a) 809.

Belykh S F, Rasulev U Kh, Samartsev A V, Stroev L V and Zinoviev A V, *Vacuum* **56** (2000b) 257.

Belykh S F , Kovarsky A P , Palitsin V V, Adriaens A, Adams F, *Int. J. Mass Spectrom.* **209** (2001) 141.

Belykh S F, Kovarsky A P, Palitsin V V, Adriaens A, Adams F, *Appl. Surf. Sci.* **203-204** (2003a) 122.

Belykh S F, Kovarsky A P, Palitsin V V, Adriaens A, Adams F, *Nucl. Instr. And Meth. in Phys. Res.* **B203** (2003b) 164.

Belykh S F, *private communication*, 2004.

Belykh S F, *private communication*, 2006.

Belykh S F, *private communication* 2007

Benninghoven A, *Chemical Physics Letters* **6** (1970) 626.

Benninghoven A, *Int. J. Mass Spectrom. Ion Phys.* **53** (1983) 85.

Bishop H E, Moon D P, Marriott P and Chalker P R, *Vacuum* **39** (1989) 929.

Blain M G, Della-Negra S, Joret H, Le Beyec Y, Schweikert E A, *Phy. Rev. Lett.* **63** (1989) 1625.

Cataing R and Slodzian G, *J. Phys.* **E14** (1981) 1119.

Chait B T and Standing K G, *Int. J. Mass Spectrom. Ion Phys.* **40** (1981) 185.

Chambost E de, Boyer B, Rasser B and Schuhmacher M, *Secondary Ion Mass Spectrometry XII* (2000) 533, Elsevier, Amsterdam.

Chang R J H, Belikh S F and Dowsett M G, unpublished design, 2005.

Cheng Juan and Winograd Nicholas, *Anal. Chem.* **77** (2005) 3651.

Clegg J B, *Surf. Inter. Anal.* **14** (1989) 307.

Chu D P and Dowsett M G, *Phys. Rev.* **B56** (1997) 15167.

Cooke G A, *Ph.D. thesis* (1992) University of Warwick.

Dahl D A, *SIMION 3D Version 7.0 User's Manual* (2000), BECHTEL BWXT IDAHO, LLC.

Davies N, Weibel D E, Blenkinsopp P, Lockyer N, Hill R, Vickerman J C, *Appl. Surf. Sci.* **203-204** (2003) 223.

Döbeli M., Nebiker P W, Mühle R, Suter M, . *Instr. And Meth. in Phys. Res.* **B132** (1997) 571.

Dowsett M G, unpublished, 1986.

Dowsett M G, McPhail D S, Parker E H C and Fox H, *Vacuum* **36** (1986) 913.

Dowsett M G and Clark E A, *Practical Surface Analysis Ch. 5*, **Vol. 2**, 2nd Ed., Wiley (1992).

Dowsett M G, Thompson S P and Corlett C A, *Secondary Ion Mass Spectrometry VIII* (1992) 187, Wiley.

Dowsett M G, Smith N S, Bridgeland R, Richards D, Lovejoy A C and Pedrick P, *Secondary Ion Mass Spectrometry X* (1997) 367, Wiley.

Dowsett M G, *Appl. Surf. Sci.* **203-204** (2003) 5.

Dowsett M G, *private communication,* 2007.

Dowson P H, in *Quadrupole Mass Spectrometry and Its Applications*, Elsevier, Amsterdam (1976).

El-Kareh A B and El-Kareh J C J, *Electron Beams, Lenses, and Optics* (1970), Academic Press.

Finkelstein A F, *Rev. Sci. Instrum.* **11** (1940) 94.

Gassiot J P, *Philos. Trans. Roy. Soc. London* **148** (1858) 1.

Gerlach R, *Secondary Ion Mass Spectrometry*, *SIMS III*, Springer Series in Chemical Physics **Vol. 19**, p. 22, Springer, Berlin (1982).

Gillen Greg, King R. Lance and Chmara Frank, *J. Vac. Sci. Technol.* **A17(3)** (1999) 845.

Gillen Greg, King Lance, Freibaum Brian, Lareau Richard, Bennett Joe and Chmara Frank, *J. Vac. Sci. Technol.* **A 19**(2) (2001) 568.

Gillen Greg, Batteas James, Michaels Chris A, Chi Peter, Small John, Windsor Eric, Fahey Albert, Verkouteren Jennifer, Kim K J, *Appl. Surf. Sci.* **252** (2006) 6521.

Gillen Greg, *44th IUVSTA Workshop: Sputtering and Ion Emission by Cluster Ion Beams*, Scotland UK, 2007.

Goldstein E, *Verh. Dtsch. Phys. Ges.* **4** (1902) 228.

Goodhew Peter J, Humphreys John and Beanland Richard, *Electron Microscopy and Analysis Ch. 6*, 3rd Ed. (2001), Taylor & Francis Inc.

Grove W R, *Phil. Mag.* **5** (1853) 203.

Herzog R F K and Vieböck F, *Phys. Rev.* **76** (1949) 855.

Hofer W O, Liebl H, Roos G and Straudemaier G, *Int. J. Mass Spectrom. Ion Phys.* **19** (1976) 327.

Iltgen K, Bendel C, Benninghoven A and Niehuis E, *J. Vac. Sci. Technol.* **A15(3)** (1997) 460.

Jede R, Ganschow O, Kaiser U, *Practical Surface Analysis Ch. 2*, **Vol. 2**, 2nd Ed., Wiley (1992).

Jiang Zhi-Xiong, Alkemade Paul F A, Algra Eelke and Radelaar S, *Surf. Interface Anal.* **25** (1997) 285.

Kilner J A, Beyer G P and Chater R J, *Nucl. Instr. and Meth. in Phys. Res.* **B84** (1994) 176.

Klemperer O, *Electron Optics*, 3rd Ed., Cambridge University Press (1971).

Kollmer F, *Appl. Surf. Sci.* **231–232** (2004) 153.

Krohn V, *J. Appl. Phys.* **33** (1962) 3523.

Lide David R (Edtor-in-Chief), *CRC Handbook of Chemistry and Physics* 2007-2008, TF-CRC (2007)

Liebl H, *Nucl. Instrum. Meth.* **187** (1981) 143.

Liu J R, Wang X M, Shao L, Chen H and Chu W K, *Nucl. Instr. and Meth. in Phys. Res.* **B197** (2002) 101.

Littlewood S D and Kilner J A, *J. Appl. Phys.* **63** (1988) 2173.

Littmark U and Hofer W O, *Nucl. Instr. and Meth.* **168** (1980) 329.

Longhurst R S, *Geometrical and Physical Optics, Ch. 2*, 2nd Ed. (1967) Longman.

Mahoney C M., Roberson S V and Gillen Greg, *Anal. Chem.* **76** (2004) 3199.

Maier M, *Vacuum* **36** (1986) 409.

Massey H S W and Burhop E H S, *Electronic and Ionic Impact Phenomena Ch IX* (1952), Oxford University Press.

Maul J L and Wittmaack K, *Surf. Sci.* **47** (1975) 358.

Medvedeva M, Wojchiechowski I, Garrison B J, *Appl. Surf. Sci.* **203-204** (2003) 148.

Middleton R and Adams C T, *Nucl. Instrum. and Meth.* **118** (1974) 329.

Middleton R, *Nucl. Instrum. and Meth.* **144** (1977) 373.

Miwa Shiro, Nomachi Ichiro, Kitajima Hideo, *Appl. Surf. Sci.* **252** (2006) 7318.

Mohoney J F, Perel J and Forrester A T, *Appl. Phys. Lett.* **38** (1981) 320.

Morris R J H, *private communication* 2007.

Nagamachi Shinji, Yamakage Yasuhiro, Maruno Hiromasa, Ueda Masahiro, Sugimoto Seiji, Asari Masatoshi and Ishikawa Junzo, *Appl. Phys. Lett.* **62** (1993) 2143.

Newton G and Unsworth P J , *J. Appl. Phys.* **47** (1976) 70.

Nielsen K O, *Nucl. Instrum.* **1** (1957) 289.

Nier A, *Rev. Sci. Instrum.* **18** (1947) 398.

Paul W and Steinwedel H, *Zeitschrift Für Naturforschung* **8a** (1953) 448.

Paul W, Reinhard H P and Zahn U von, *Z. Phys.* **152** (1958) 143.

Reuter W and Wittmaack K, *Applications of Surface Science* **5** (1980) 221.

Prewett P D, Jefferies D K and McMillan D J, *Vacuum* **34** (1984) 107.

Ronsheim P A, *Appl. Surf. Sci.* **252** (2006) 7201.

Rybalko V F, Kolot V Ya and Fogel Ya M, *Soviet Phys.-Solid State* **11** (1959) 1142.

Samartsev A V, Duvenbeck A and Wucher A, *Phys. Rev.* **B72** (2005) 115417.

Samartsev A V and Wucher A, *Appl. Surf. Sci.* **252** (2006) 6474.

Sigmund P, *Phys. Rev.* **184** (1969) 383.

Sigmund P, *Appl. Phys. Lett.* **25** (1974) 169.

Sigmund P, *Sputtering processes: Collision Cascades and Spikes, Inelastic on-Surface Collisions*, Ed. by Tolk N H, Tully J C, Heiland W and White C W, Academic Press Inc., New York (1977) 121.

Sigmund P, *Sputtering by particle bombardment. I. Physical sputtering of single element solids. Ch. 2, Topics in Applied Physics*, Ed. by R. Behrisch, **47** (1981) Springer.

Sigmund P and Claussen C, *J. Appl. Phys.* **52(2)** (1981) 990.

Slodzian G, *Applied Charge Particle Optics B, Advances in Electronics and Electron Physics*, Ed. Septier A, **Vol. 13**, p. 1, Academic Press, New York (1980).

Slodzian G, Girard F, Boust F and Hillion F, *Proceedings of Secondary Ion Mass Spectrometry Conference VIII*, Ed. by Benninghoven A, Janssen K T F, Tumpner J, and Werner H W, Wiley (1992).

Smith N S, *Ph.D. thesis* (1996) University of Warwick.

Stevie F A, Kahora P M, Simons D S and Chi P, *J. Vac. Sci. Technolol.* **A6** (1988) 76.

Sykes D E, Chew A, *Surf. Interf. Anal.* **21** (1994) 231.

Szymczak W, Wittmaack K, *Nucl. Instrum. Meth*. **B88** (1994) 149.

T *ä* rvi T T, J. Pakarinen A, Kuronen A and Nordlund K, *EPL* **82** (2008) 26002.

Thompson D A and Johar S S, *Appl. Phys. Lett.* **34(5)** (1979) 342.

Thompson D A, *Radiat. Eff*. **56** (1981) 105.

Thomson J J, *Philosophical Magazine* **20** (1910) 752.

Urbassek H M and Michl J, *Nucl. Instr. and Meth. in Phys. Res.* **B22** (1987) 480.

Vályi L, *Atom and Ion Sources* (1977), John Wiley & Sons.

Vancauwenberghe O, Hellman O C, Herbots H, Tan W J and Olson J, *Mater. Sci. Eng.* **B12** (1992) 97.

van der Heide P A W, Lim M S, Perry S S and Bennett J, *Nucl. Instr. and Meth. in Phys. Res.* **B201** (2003) 413.

Veryovkin I V, Belykh S F, Adriaens A, Adams F, *Instr. And Meth. in Phys. Res.* **B219-220** (2004) 215.

Vandervorst W, *Appl. Surf. Sci.* doi: 10.1016/j.apsusc.2008.05.090.

Wagner M S, *Surf. Interface Anal*. **36** (2005) 42.

Wagner M S, *Surf. Interface Anal.* **36** (2005) 53.

Wagner M S, *Surf. Interface Anal*. **36** (2005) 62.

Wien W, *Annal. Phys.* **8** (1902) 260.

Williams P, *Surf. Sci.* **90** (1979) 588.

Wittmaack K, *Appl. Phys. Lett.* **29** (1976) 552.

Wittmaack K, *Surf. Sci.* **90** (1979) 557.

Wittmaack K, *Nucl. Instr. Methods.* **168** (1980) 343.

Wittmaack K, Wach W, *Nucl. Instr. and Meth.* 191 (1981)327.

Wittmaack K, *Vacuum* **32** (1982) 65.

Wittmaack K and Poker D B, *Nucl. Instr. and Meth. in Phys. Res.* **B47** (1990) 224.

Wittmaack K, *Practical Surface Analysis Ch. 3*, **Vol. 2**, 2nd Ed., Wiley (1992).

Wittmaack K, *Nucl. Instr. and Meth. in Phys. Res.* **B85** (1994) 374.

Wong S C C, Hill R, Blenkinsopp P, Lockyer N P, Weibel D E and Vickerman J C, *Appl. Surf. Sci.* **203-204** (2003) 219.

Yamada Isao, Matsuo Jiro, Toyoda Noriaki, Kirkparick Allen, *Materials Science and Engineering* **R34** (2001) 231.

Zalm P C and Vriezema C J, *Nucl. Instr. and Meth. in Phys. Res.* **B64** (1992) 626.

Zimmermann Steffen, Urbassek Herbert M, *Int. J. Mass Spectrom.* **272** (2008) 91.